AALBORG UNIVERSITY
INSTITUTE OF ELECTRONIC SYSTEMS
DEPARTMENT OF CONTROL ENGINEERING

Frederik Bajersvej 7 ▪ DK-9220 AALBORG Øst   Telefon 96 35 80 80

TITLE: Attitude Determination for AAU CubeSat
THEME: Autonomous and reliable systems
PERIOD: 4th of September 2001 to 6th of June 2002
GROUP: IAS-1030

AUTHORS:
  Kristian Krogh

  Elmo Schreder

SUPERVISOR:
  Thomas Bak

Synopsis

NUMBER OF COPIES: 7
NUMBER OF PAGES: 133 pages
HANDED IN: 6th of june 2002

Contents

chapter 1

Introduction

This report describes the development of the attitude determination system for a satellite project at Aalborg University. The satellite, called AAU CubeSat, is a pico satellite designed and build by engineering students of the university. It is to be launched into space in the spring of year 2003 after a development time of approximately 1.5 year. The purpose of this project is to give students a unique chance to experience a real engineering project with real engineering problems.

The satellite is designed to take satellite photos of Denmark from an Low Earth Orbit at a height of 700 km. These photos will be transmitted down to a ground station at Aalborg University and be published over the Internet. The satellite relies on attitude determination and control in order to acquire photos of chosen geographic targets. This report is handed in as a master thesis, and documents the development of the attitude determination system. At the time this report was finished, work was still being done on the satellite subsystems. This is also the case of the attitude determination and control subsystem.

1.1 The CubeSat concept

The first satellite developed entirely by students at Aalborg University is a CubeSat. A CubeSat is a standardized pico-satellite format developed for small orbital experiments and designed to house small experiments. It was developed by Stanford University and was chosen for the first AAU satellite.

The design requirements set up for the CubeSat consist of a limited size and weight. The satellite shape consists of a cubic shaped platform with the length of 10 cm. The maximum weight allowance of the entire construction is limited to 1kg.

The CubeSats are launched with a rocket into space as secondary or tertiary payloads. This is done using a standardized deployment system developed by California Polytechnic State University. This deployment system, which is known as a P-Pod, is attached as extra load on a launch vehicle and contains three CubeSat satellites. These are after the launch deployed into space from the P-Pod by the force of a spring in the deployment system.

A clear benefit of the CubeSat concept is the inexpensive launch possibility for small satellite projects, which otherwise would be too cost-prohibitive to launch into space. In this way CubeSats have shown to be the ideal solution for small satellite projects developed by universities as they make a simple, cost effective and fast development possible. At many universities around the world CubeSat project are taking place. A first launch of 18 CubeSats is scheduled for the year 2002.

1.2 Outline of report

The development of the Attitude Determination and Control System (ADCS) has been split up into two parts. The Attitude Control (ACS) part containing the main task of maintaining or changing the satellites attitude, based on information about the satellites attitude. The design and development of the attitude control is described in (Frederiksen et al., 2002).

The second part of the ADCS consists of the Attitude Determination (ADS), which main purpose it is to determine the current attitude of the satellite by use of on-board sensors, mathematical models used as reference to measurements. This report will deal with the subject of attitude determination of the AAU CubeSat. The focus will be on sensors and attitude determination methods. We will not go into details of software implementation, partly because not all software has been developed yet, but also because it would be quite a task to describe.

Chapter 2 gives an insight to the mission objectives of the AAU CubeSat. Further the life cycle and system of the satellite is described. Here a focus will be on the Attitude Determination and Control System (ADCS) and its required performance.

Chapter 3 concerns the analysis of the ADS. Apart from describing the choice of sensors it defines the for the attitude determination strategy and architecture.

Chapter 4 will line up the different requirements set up regarding the development of the hardware and software for the ADS. Following the requirements corresponding test specifications are defined to validate if the requirements have been fulfilled.

The design of the hardware for the ADS is described in chapter 5. Here the design of the circuitry for the sensors is described as well as the interfacing of these components to the micro controller in the attitude determination and control system.

Chapter 6 describes the integration of the ADCS in the satellite. This includes the development of sun sensor sockets as well as the placement of the sensors on the satellite structure.

The orbit of the satellite and its properties is described in chapter 7. Here also some on-board algorithms used to determine the satellites orbital position are described and evaluated.

The chapter describing the orbit of the satellite is followed by chapter 8 explaining the algorithm used to determine the position of the Sun. Further a model is developed of the Earth albedo and its impact on the ADS performance.

The next chapter 9 describes and evaluates the magnetic field model used in the ADS for the attitude determination with the measurements of the magnetometer.

Chapter 10 will introduce deterministic algorithms for determining an attitude based on reference and measurement vectors. These are evaluated and a suitable algorithm is chosen and evaluated.

The chapter about the deterministic attitude determination algorithm is followed by chapter 11, describing an attitude estimation using an extended Kalman filter. This method is accordingly tested and its performance evaluated.

In chapter 12 the conclusion of the project is given.

chapter 2

Mission analysis

In this chapter a general view of the mission of the AAU CubeSat will be given. It will present the mission objectives, life-cycle of the satellite and operational modes of the attitude determination and control system. A short description will be given of subsystems and their interfaces.

2.1 Mission objectives

The development of the AAU CubeSat is a project carried out by students at Aalborg University. A number of project groups have responsibility for designing and developing the different subsystems for the satellite. Work was coordinated between groups in a series of meetings and summaries. As a result of some of these meetings, the mission objectives for the satellite were determined.

Besides the objective for students to gain engineering skills in their line of education and in the field of developing satellites, the following objectives were defined for the AAU CubeSat:

- The primary mission of the AAU CubeSat will be to take pictures of the earth from a low earth orbit (LEO) at approximately 700 km height. For this purpose a CMOS camera is going to be used. This will take color pictures in the visible light spectrum. The pictures will be transmitted to a ground station and made public via the Internet. People using the Internet will have the possibility to request the satellite to take a photo of a geographic location. The scope of photo coverage will be restricted to Denmark.

- The purpose of this mission is to increase public interest in space science, technology and natural science in general. The satellite can show that it is possible to monitor or take pictures of the Earth from LEO with a small pico-satellite like the CubeSat.

- With this being the first in a line of possibly more CubeSat projects at AAU, it is part of the mission to bring some experience to AAU in the field of developing CubeSats. Students working on future CubeSats at AAU may learn from the results of this project. For this to be possible it is important to document all project work and receive health data from the subsystems on-board the satellite, after it has been launched.

- In order to secure a high level of reliability in expensive satellites, it is normal to use components which have been well tested for use in space. However, this being a low cost satellite, some experimentation is done in the choice of components. This is the case with the payload camera, solar panels and a lot of other components in the subsystems of the satellite.

- It has also been proposed that the satellite should perform a task with a more scientific purpose. This regards the observation of stars. Monitoring the stars efficiently would require on-board analysis of data from the camera, which would proof to be difficult to implement on a CubeSat. However, it has been decided that it would be a good idea to take some pictures of stars, in order to decide if the camera and lens together with the other subsystems in the AAU CubeSat could perform this mission. This could provide a good basis for later CubeSats designed specifically to monitor the stars.

3

2.2 Satellite life cycle

The life cycle of the satellite can be described as a number of life phases. It consists of pre-launch, launch, deployment, mission in orbit, end of functionality and reentry into the Earths atmosphere. The life phases are explained in the following sections.

2.2.1 Pre-launch

The first life cycle begins when development and test of the satellite has been completed and it is transported from Aalborg to Kasakhstan. Before launch tests shall be performed for the satellite to secure that it is functional, and that it fulfills requirements set forth in *The P-POD Payload Planner's Guide* (Connolly, 2000). At the final stage of the pre-launch phase the satellite will be transported to the launch site, where it will be inserted into the P-POD, which has been mounted on the satellite platform of the launch vehicle. The P-POD is a simple mechanism designed for deploying the satellite. During the time the satellite is inside the P-POD, a mechanical switch shall secure that all subsystems are without electrical power. Not until deployment will power be switched on.

2.2.2 Launch

The AAU CubeSat will be launched into orbit with a various number of up to 17 other CubeSat satellites from Baikonur Kosmodrome in Kasakhstan in may 2003. The launch vehicle will be a Dnepr-rocket, which is a former ICBM reconfigured for the purpose of sending small satellites into Low Earth Orbit.

As the CubeSats represent the secondary payload of the launch mission, the date of the launch might be postponed to wait for the primary load. For this reason a precise launch date or the orbit parameters are not yet known. Following the pre-launch phase the launch phase should only take few hours including the last preparations and the launch itself and the flight time.

2.2.3 Deployment

After the insertion of the payload into orbit, the deployment of the satellites will follow. The primary load, consisting of one or two micro satellites, will be deployed. After a delay of minutes or hours the deployment of the CubeSats will follow. The P-Pods will open one by one to push the three containing CubeSats out into space. After the deployment of the AAU CubeSat the satellite will initialize itself after a
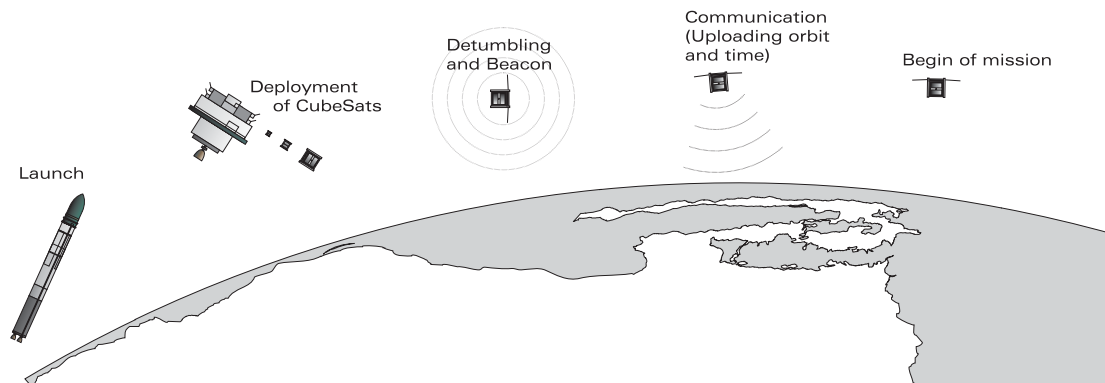
Figure 2.1: The deployment and initialization of the satellite before the startup of the actual mission.

delay of some minutes. This delay is required in (Connolly, 2000) with the purpose of getting into a certain distance from the P-Pod and the other CubeSats before deploying the communication antennas.

The on-board computer will start with a boot-up sequence for the subsystems. The communication subsystem includes a beacon function which will be activated in the boot-up and send a standard beacon signal.

4

When the attitude determination and control subsystem in the satellite has been initialized, the satellite will start a detumbling maneuver. The detumbling is performed in order to slow down any rotations of the satellite, which may be caused by the deployment. When detumbling is performed the satellite will point the solar panels towards the Sun to collect as much power as possible.

As soon as the first communication with the satellite is established, the basic beacon will be turned off and the satellite will receive the properties of its orbit, to obtain knowledge about its position. The deployment and startup of the satellite is also described in figure 2.1.

2.2.4 Mission in orbit

During the mission in orbit the satellite will receive a flight-plan. The flight plan will contain a time schedule which informs the satellite on how to behave at different times. In the flight plan it will be specified which geographic site to photograph and at what time. The satellite will then autonomously change its attitude and at the specified time acquire a photo of the site to be photographed. During the next passes over the ground station data will be transmitted to Earth and the satellite will receive the flight-plan for the next photo-task. The satellite shall be designed to take at least one photo per day. When the satellite is not acquiring any photos it shall try to optimize the energy input to the solar panels. During the mission phase housekeeping data shall be transmitted to the ground station. Housekeeping is data sampled from the on-board subsystems describing status and including informative data.

During its mission the satellite will be exposed to many environmental effects. These range from the vacuum in space over thermal effects and major temperature changes to electro-magnetic radiation. The environmental effects connected to a Low Earth Orbit are also described in appendix A.

2.2.5 End of functionality and Reentry

The satellite shall be designed to have an active lifetime of at least one year. After ended functionality of the satellite, it will stay in orbit as space debris. Finally it will burn up during the reentry approximately 20 years after the launch, ending its existence in a minor visual effect on the night sky.

2.3 System description

The complete system to be considered includes the satellite and a ground station for communicating with the satellite. The satellite is divided into subsystems, to be developed by project groups at Aalborg University. The subsystems are the following:

Satellite structure: The AAU CubeSat must fulfill the requirements set up by OSSS (One Stop Satellite Solution) and Stanford University, which originally developed the Cube-Satellite concept (Connolly, 2000). The size of the satellite has to be 10 x 10 x 10cm, while its weight has to be below 1kg. To achieve this, light materials are used to develop and build the structure of the satellite. Its design will be based on a frame of aluminum with sides made of carbon fibers. High requirements have been set regarding the structure of the satellite and its integrity, as it has to withstand high temperature variations between +80 and -40 °, vibrations and shocks, radiation, and the vacuum in space. The group responsible for the satellite structure will also be responsible for weight and space budgets, which other subsystems are confined to. The satellite structure is developed by (Overgaard and Hedegaard, 2002).

Power supply: The power supply unit (PSU) relies on four 3.7 V Li-Ion batteries and five pairs of triple junction solar panels, which are placed on the surface of 5 of the 6 sides of the satellite. The Power Supply Unit (PSU) provides other subsystems with a nominal voltage of 5 volt and monitors the performance of the different subsystems regarding their power consumption. Apart from being used to gather electric power are the solar panels also used as backup sun sensors for the ADS. The PSU was developed by (Lazar et al., 2002).

On-Board Computer: The on-board subsystems are controlled from a central On-Board Computer (OBC) of the type C161PI from SIEMENS. It has a 16-bit CPU and 16 Megabytes Total Linear Address Space. The OBC will use two types of memory. A ROM module for stack operations and buffers and a RAM module for system software, housekeeping and payload data. The communication between the subsystems and the on-board computer will run over an I^2C bus, which will connect between the Power Supply Unit, the Attitude Determination and Control, The Camera and the Communication Unit. The OBC has been the responsibility of (Clausen et al., 2002).

Furthermore software has been developed for the OBC. This is the Command and Data Handling (CDHS).

Payload camera: The payload is the on-board camera for taking satellite photos. It uses a digital CMOS camera chip based on a Kodak 1.3 megapixel kac1310, which has been provided by the Danish company DEVITECH. It will take photos of the Earth with a field of view of 100 x 80 km and a resolution of 1280 x 1024 pixels with a color depth of 24bit. The lens in front of the CMOS camera chip is handmade with a diameter of 20mm at a length of 50mm. The payload camera has been the responsibility of (Clausen et al., 2002).

Communication unit: For receiving telemetry from the ground station as well as for transmitting the on-board status and the photos acquired during flight, an on-board communication unit is used. In this case the on-board communication unit and antenna is purchased from OSSS and will communicate with ground by using radio amateur frequencies. The antenna attached to the satellite will be deployed after the launch from the P-Pod into space. To be able to communicate with the CubeSat from ground, a tracking antenna will be used, which will follow the satellites motion over the sky.

Attitude determination and control system : To be able to take photos of the Earth, an attitude determination and control system (ADCS) is required. It will be used for pointing the camera, which is fixed in the satellite structure. Furthermore it shall be needed after deployment for detumbling the satellite. Between photo-tasks the ADCS is needed for pointing three of the satellite sides with solar panels towards the Sun to maximize the power input. This also secures that the camera is not pointed directly towards the Sun.

The ADCS is divided into two projects. One project develops the control related part of the subsystem (ACS). This includes actuators and control algorithms. The ACS is described in (Frederiksen et al., 2002). The other part of the ADCS is the one described in this report, which is the attitude determination related part (ADS). This includes developing sensors and algorithms for attitude determination.

Ground station: The ground station, which is located in Aalborg, will communicate with the satellite and download satellite photos and housekeeping data. Accordingly new flight plans and configurations of the satellite are uploaded from the ground station to the satellite.

The download of an entire satellite photo will take several orbits, as the entire download at the current communication speed of 9600 bit/sec will take up to 20 minutes, and a single orbit pass over Denmark under ideal circumstances only lasts 8 minutes.

The data transmitted down to the ground station will be processed and the acquired photos will be published on the Internet. Further it will be possible for visitors of the AAU CubeSat web-page to place an order for a photo of a location in Denmark. This photo request will automatically be uploaded in a succeeding flight plan.

2.3.1 Interfaces between Subsystems

Subsystems are connected as shown in figure 2.2. The camera is connected to the OBC by a separate interface, while the communication between the OBC, PSU, communication unit and ADCS runs over the I^2C bus.

The Power Supply Unit PSU connects to the kill switch, batteries and solar panels while the ADCS is hooked up to the sensors and actuators.
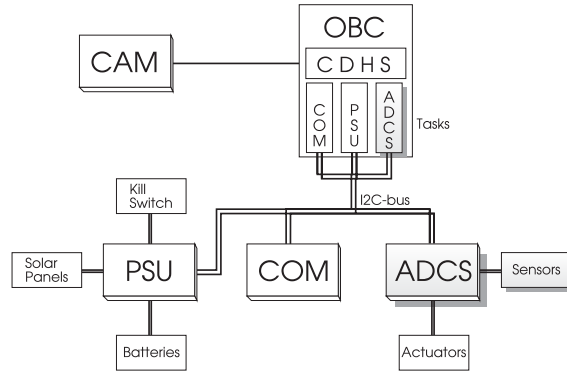
Figure 2.2: Diagram illustrating the satellite subsystems and their internal connections.

The CDHS is installed on the OBC with a task to interface each of the subsystems PSU, COM and ADCS. Each of the tasks collects housekeeping[1] from the subsystems and sends commands from DHCS to the subsystems. Housekeeping data coming from subsystems include status and error reports to be logged, interpreted and acted upon in the subsystem task on the OBC.

The subsystem task for the ADCS to be implemented on the OBC will contain the algorithms for attitude determination (ADS). The attitude control (ACS) algorithms are implemented in a micro-controller in the ADCS subsystem. The ADCS subsystem is connected to actuators and sensors. Using this structure means that the sensor data will be included in housekeeping data from the ADCS subsystem and send to the ADCS task on the OBC. On the OBC the attitude will be determined based on housekeeping data. The difference between a reference attitude and the actual attitude will be returned to the ADCS subsystem where it is used for attitude control.

The main part of the attitude determination software will be implemented in the ADCS task on the OBC. Only a few algorithms are needed for sampling the attitude sensors on the micro-controller of the ADCS subsystem. Work related to the ADCS subsystem has been developing and interfacing the sensors and writing software to test the sensors.

2.4 Required pointing accuracy

A very simple consideration is used for determining the requirement to the pointing accuracy of the satellite. The required pointing accuracy when acquiring a satellite photo is based on the size and resolution of the photo, which is going to be taken of Denmark. The photo taken of Denmark at a height of 700 km above the Earth surface is going to cover approximately 100×100 km. The max deviation of the intended center of the photo to the actual center of the photo was decided to be approximately 100 km. According to these parameters a pointing accuracy was calculated as shown in equation 2.1

$$PointingAccuracy \leq \arctan\left(\frac{100km}{700km}\right) = 8.13°$$ (2.1)

This pointing accuracy of $8°$ is accordingly the main requirement of the ADCS.

2.5 The Operation Modes of ADCS

The satellite is dependent on the ADCS to change its own attitude when performing a photo task and when optimizing power. For this to be obtained the following operation modes have been defined for the satellite:

---

[1]Housekeeping is data sampled in a subsystem with the purpose of being transmitted to ground for study

Initialization, Fail Safe, Detumbling, Power Safe and Camera mode. A state diagram showing these modes is shown in figure 2.3. The ADCS starts in the state *Off*.
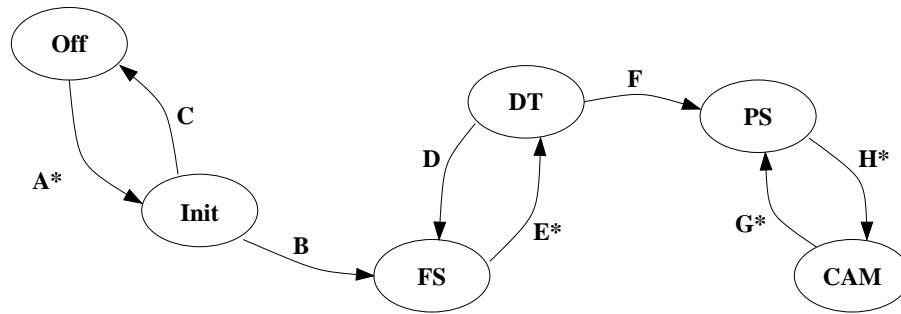

Figure 2.3: A state diagram describing the six different operation modes of the satellite including their connections.

In figure 2.3 the functions marked with $*$ are triggered external by the OBC or PSU. The state diagram shows the natural flow between states in the ADCS. Apart from this the following three notes are given regarding the ADCS:

1. On Fail any state may go to OFF-state (Soft Reset).

2. The Command and Data Handling System (CDHS) may at any time force the ADCS into any state: FS, DT, PS or CAM.

3. The CDHS and PSU may force the ADCS into OFF-state with a Hardware-reboot or power off.

Initialization (Init): After deployment or at reboot the power supply unit turns the power on for the ADCS subsystem **A**. During initialization sensors and actuators in the ADCS are initialized. Errors from initialization of ADCS hardware are reported as housekeeping.

Fail Safe (FS): When the initialization **Init** is completed **B** the ADCS automatically enters fail safe operation mode **FS**. In this mode the ADCS will be on standby until a command from the CHDS allows it to continue **E** to detumbling mode.

Detumbling (DT): In this mode the ADCS will detumble the satellite. If the detumbling is completed successfully or no detumbling is needed, the system will continue **F** to the power save mode. If a timeout occurs in detumbling mode the ADCS will return **D** to fail safe mode.

Power Safe (PS): In Power Save Mode **PS** the ADCS will change the attitude of the satellite so three solar panels are pointed towards the Sun. This is to obtain a maximum power input from the solar panels. When the satellite is in the shadow of the Earth (eclipse), it is important that power consumption is kept low in all subsystems. At a scheduled time in the flight plan, the satellite needs to change attitude to acquire a photo, the CDHS commands the ADCS to change to camera mode **H**.

Camera Mode (CAM): In camera mode the ADCS will change the attitude of the satellite in order to acquire a photo. The ADCS will receive reference attitude from the CDHS. In the flight plan time is specified for when the ADCS should go into Camera mode, and when the CDHS shall acquire a photo using the payload camera. After the photo is taken **G**, the system will return to Power Safe mode **PS**.

It was decided to use the flight plan to specify when to change to camera mode and when to leave camera mode. Accordingly the flight plan dictates at what time to acquire the photo. This time is calculated beforehand at the ground station by the use of an orbit model. In figure 2.4 the task of acquiring a photo is illustrated. The satellite enters from the right of the figure in power save mode. The CDHS commands
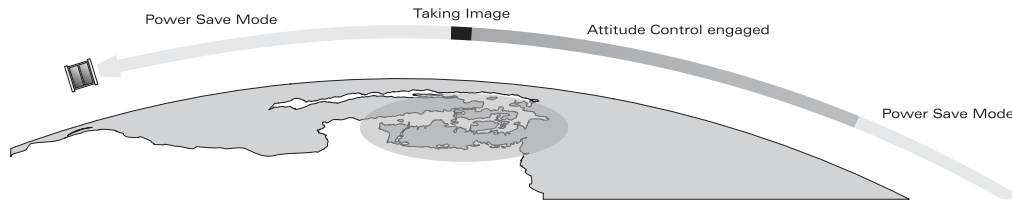
Figure 2.4: The satellite goes from Power Safe Mode into Camera mode until the photo is obtained over the target area and the system returns to Power Safe mode.

the ADCS to change into Camera mode. At the time specified the flight plan, the CDHS uses the payload camera to acquire the photo. After this the CDHS commands the ADCS to change into power save mode.

No attitude control is needed to ensure communication with the ground station. This means that detumbling, power save mode and camera mode are the modes in which attitude control is needed. The attitude determination is needed in power save mode and camera mode [2]. The accuracy requirement for the camera mode, section 2.4 will also be used for the power save mode. In the remaining of this report, the focus will be on developing an attitude determination system, to fulfill the requirements in power save and camera mode.

2.6 Summary

The defined mission objectives of the satellite were specified. Some objectives are educational, because the satellite is developed by students. Other objectives are: Remote sensing, raising public interest, testing components in space and gaining experience with pico-satellites.

The satellite has five life cycle phases consisting of pre-launch, launch, deployment, mission in orbit and end of functionality. The satellite subsystems were shortly described in section 2.3. The system consists of power supply (PSU), a central On-board computer (OBC) with a Command and Data Handling System (CDHS), a payload camera (CAM), a communication unit (COM) and an attitude determination and control system (ADCS). A ground station is also being developed with communication hardware, control center and interface to the Internet. The ADCS subsystem will be implemented in the ADCS subsystem and in a thread on the OBC. The main part of the ADS is implemented on the OBC and the ACS is implemented on a micro-controller in the ADCS subsystem.

The pointing accuracy for the ADCS was determined to be 8°. Operation modes for the ADCS describes the functionality of the ADCS in relation to other subsystems. An initialization mode is needed for initializing ADCS hardware. In fail safe mode not attitude control is used. A detumbling mode is needed to slow down rotations of the satellite after deployment. A power save mode is used to optimize Sun input on the solar panels and a camera mode is needed when acquiring satellite photos. The attitude determination is needed in power save and camera mode to secure a pointing accuracy of 8°.

---

[2]Though detumbling needs magnetometer data, this mode has required no attention from attitude determination and is handled by (Frederiksen et al., 2002)

chapter 3

Analysis

The analysis in this chapter results in defining requirements for hardware and attitude determination algorithms. The attitude control strategy and actuators chosen for the satellite are described in section 3.2. In section 3.3 the analysis of the attitude determination takes its starting point in analyzing, which sensors to use. The choice of the attitude determination method, in section 3.4, involves choosing an attitude determination strategy. This involves determining the attitude using a deterministic method or an extended Kalman filter, which is a recursive estimation method. The analysis of the attitude determination method is concluded with defining the overall design of the attitude determination in section 3.5.

3.1 Coordinate Frames

For the purpose of determining the attitude in three dimensional space, several coordinate frames are defined. As the names of these frames will occur several times in the description of the attitude determination, they will be described in this section.

3.1.1 Reference Coordinate Systems

To define an orbit around Earth, two specific Earth related coordinate systems are given beforehand. They both have their origin in the geometrical center of Earth and are named the Earth Centered Inertial (ECI) coordinate frame and the Earth Centered Earth Fixed (ECEF) coordinate frame. These can be seen in figure 3.1.
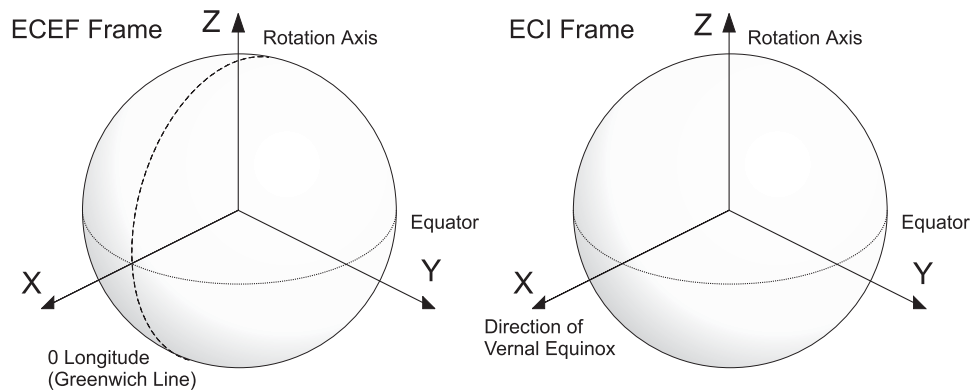

Figure 3.1: The ECI and ECEF coordinate frame

The ECI Coordinate Frame The term ECI stands for Earth Centered Inertial and represents a coordinate system with origin in the center of Earth, which is fixed relative to the Earth rotation. Its X-axis is

parallel with the Vernal Equinox (The axis around which the Earth rotational axis is tilted relative to its orbital plane) and its Z-axis, which is parallel with the Earth rotational axis.

The ECEF Coordinate Frame The second coordinate frame is the Earth Centered Earth Fixed (ECEF) coordinate frame. In this frame the X-axis is passing through the zero longitude, also known as Greenwich meredian, and has a Z-axis parallel with the rotational axis. In this way the ECEF frame is fixed to the earth itself and rotates around with it.

3.1.2   Spacecraft Coordinate Systems

To determine the attitude of the satellite, some spacecraft fixed coordinate systems are introduced. The attitude and position of the satellite is accordingly given as a rotation between the satellite fixed coordinate frames and the reference frames.

The SCB Frame The first frame, called Spacecraft Body Frame (SCB), is placed in the center of mass of the satellite and fixed to the satellites geometric axes. In case of the AAU CubeSat, the X-axis of this coordinate frame is defined as being parallel with the camera axis. Accordingly the Y-axis and Z-axis are placed perpendicular on the satellite sides, which are parallel with the Z-axis. A description of the SCB frame can also be seen in chapter 6.

The SCP Frame The Space Craft Principal Axes frame is similar to the SCB frame fixed to the satellite and centered in the satellites center of mass. However, it is not fixed to the geometric properties of the satellite but to the inertial properties. It represents the principal axes, in which the principal moments of inertia are given as a diagonal matrix. The SCP frame will be defined in chapter 6.

The SCO Frame The last spacecraft related coordinate frame is the Space Craft Orbit frame, which is the link between the spacecraft fixed frames and the reference frames. It is parallel with the ECI frame axes but centered in the satellites center of mass. This frame is used to transfer the vectors calculated with reference to the earth centered coordinate systems out to the satellites position to compare them with the measurements of the attitude determination in the SCB frame.

3.2   Attitude control strategy

The control strategy used for the remote sensing task is determined in cooperation with the group responsible for designing and implementing the attitude control. For a detailed description of the choice of control strategy and actuators see (Frederiksen et al., 2002).

Magnetorquers, momentum and reaction wheels were considered as possible actuators. It has been chosen to use magnetorquers mainly due to their limited size. The magnetorquers are mounted on the outside of the satellite structure and will unlike momentum or reaction wheels not take up space inside the satellite. Compared to momentum wheels the magnetorquers have no moving parts and this is an advantage when considering lifetime and complexity of the satellite. It has been decided to use three magnetorquers for satellite control. Three-axis attitude control using three magnetorquers has all ready proven to be feasible in the Danish satellite Ørsted.

As illustrated in figure 3.2 the satellite will be inertial pointing. This means, that the attitude control reference is a pointing direction vector given in the ECI frame. In daylight power save mode the reference vector points towards the Sun. In camera mode the reference vector is defined as a vector, going from the point on the orbit, from where the photo is to be obtained, to the photographic cite to be photographed.
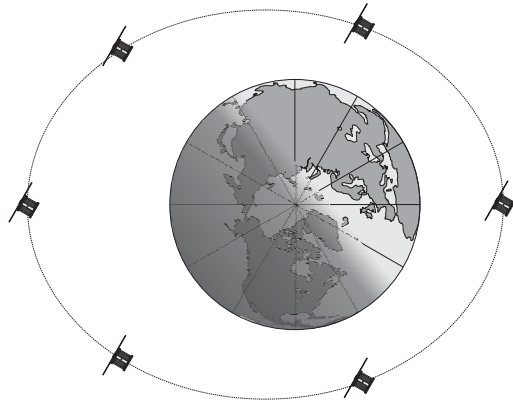
Figure 3.2: The inertial pointing satellite is given a reference vector in the ECI frame for the attitude control

3.3 Attitude determination sensors

Three-axis attitude control is needed in camera mode or power save mode in sunlight. In order to have three-axis attitude control it is necessary to determine a full three-axis attitude given in the ECI frame. The choice of sensors for the satellite is described in this section.

In order to determine the three-axis attitude the position of the satellite in the ECI frame must be known. Furthermore at least two non-collinear vector measurements in the SCB frame together with corresponding vectors in the ECI frame are needed. The position can be determined using a mathematical model for the satellite orbit together with Kepler elements describing the orbit, which are provided as two-line element sets by NORAD (CelesTrak, 2002). Vector measurements in the SCB frame are acquired using attitude sensors. The corresponding vectors in the ECI frame are determined from mathematical models.

Sensors for attitude determination in a satellite can be categorized as reference sensors or inertial sensors (Bak, 1999). A reference sensor measures in SCB frame the direction to a reference point known in the ECI frame, while an inertial sensor measures rotational or translational motion. Different types of reference sensors and inertial sensors are described and evaluated with respect to use in the AAU CubeSat in section 3.3.1 and section 3.3.2, respectively.

3.3.1 Reference sensors used in satellites

The reference sensors considered for the AAU CubeSat are: Star sensors, horizon sensors, sun sensors, three axis magnetometers and GPS.

Star sensors: Star sensors are cameras used for recognizing star patterns in the sensors field of view. Camera technologies as Charged-Coupled Devices (CCD), Active Pixel Sensors (APS) and CMOS could be considered for the task. The location of two or more stars on the sensor is enough to determine the attitude of the satellite. This means that a star sensor alone can determine a three axis attitude, when pointing towards the sky. An on-board star database is necessary for recognizing star patterns and determining vectors in the ECI frame.

Horizon sensors: Horizon sensors detect the threshold between infrared light of the Earth's atmosphere and the cold space. A horizon sensor uses an infrared diode and a lens. There are two kinds of horizon sensors; scanners and horizon crossing indicators (Larson and Wertz, 1992). A horizon crossing sensor is fixed in the satellite structure and will only provide valuable attitude information when the sensors line of sight crosses the threshold between the Earth's atmosphere and space. Due to size, weight and complexity only static horizon crossing indicators are considered suitable for the CubeSat. This type of sensor has to be used together with other attitude sensors, if it is to be used in the satellite.

12

Sun sensors: Sun sensors are used for providing a vector measurement to the Sun. Sun sensors are available in various designs, small sizes and low mass of just a few grams. One simple type of sun sensor is the cosine detector (Wertz, 1978) which uses the fact, that the output current from a silicon solar cell has a sinusoidal variation with the angle of incoming sunlight. One cosine sensor is a single axis sun sensor, and one cosine sensor on each side of the cube shaped satellite makes it possible to determine a Sun vector. Different designs exist for making double or three axis sun sensors. These designs normally use a mask for shading off incoming light and multiple silicon sensors in different shapes and sizes (Wertz, 1978). The measured Sun vector is compared to an on-board model of the direction to the Sun in the ECI frame. Incoming Earth Albedo on a sun sensor will affect the accuracy of the sensor.

Three-axis magnetometer: In Low Earth Orbit, where the magnetic field of the Earth is well defined and strong a 3-axis magnetometer will provide valuable attitude information. Magnetometers are available in mainly three different versions: As fluxgate, magneto-resistive and magneto-inductive sensors. They can be purchased as sensors of small weight, size and low power consumption. However, electronics in the satellite and external disturbances are often a source of disturbance when using a magnetometer. The measured magnetic field vector is compared to an on-board reference model of the magnetic field for the determination of the satellites attitude.

GPS: This sensor is used for providing the position of the satellite. This technology will not be considered for the CubeSat as the position is determined using an orbit model together with Kepler elements provided by NORAD.

3.3.2 Inertial sensors used in satellites

Inertial sensors used in satellites include accelerometers and rate gyros.

Accelerometers: Accelerometers measure translatory accelerations. Accelerometers are typically used with an on-board propulsion system and hence not of interest here.

Rate gyros: Rate gyros are used for determining the rotary motions of the satellite as angular velocities. These angular velocities can be used for estimating the attitude or to provide a velocity feedback to the attitude control. However, due to drift in the rate gyros it is necessary also to use attitude sensors to compensate for this effect and to determine a precise attitude. In this way rate gyros can supplement other sensors in order to improve the attitude determination by including the satellites rotations. Rate gyros are available in very small sizes, of low weight and power consumption and have already been used on some CubeSats (CubeSat Cute, 2002).

3.3.3 Choice of sensors for the AAU CubeSat

First of all the sensors chosen for attitude determination must combined be able to provide a three-axis attitude determination. The accuracy of the total attitude determination and control system, must for camera mode be $8°$ σ. According to (Bak, 1999) typical accuracies for reference sensors are as specified in table 3.1 and can be used as guidelines.

Horizon sensor	Sun sensor	Star sensor	Magnetometer
0.05 deg - 1 deg	0.005 deg - 4 deg	1 arc sec - 1 arc min	0.5 deg - 5 deg

Table 3.1: Typical accuracies for reference sensors

Due to the size and weight of the CubeSat and in order to keep down costs, the focus is not on expensive commercial attitude sensors. This means that developing sensors is part of the project. Of the sensors described in section 3.3.1 and section 3.3.2 the star sensors, horizon sensors, sun sensors, magnetometers

and rate gyros are the sensors considered most suitable for the AAU CubeSat. In the following section each sensor type is discussed and a sensor configuration is chosen.

Star Sensors: Even as star sensors are the most accurate reference sensors according to table 3.1, it has been decided, not to use this sensor type. Though it might be possible to design a star tracker from using a camera chip, it is considered, that this type of sensor will be too great a task to implement within the limited project period. Also the on-board processing needed to determine the attitude from star constellations could be a problem. Power consumption of a camera chip and electronics needed to interface it, will be relatively large compared with the other sensors. Using a camera chip, which has not already been tested in space, would also require extensive testing to make sure the component can be used in the harsh environment of the low Earth orbit.

Horizon Sensors: A clear disadvantage of the horizon sensors is, that they only provide data for attitude determination when detecting the threshold between the atmosphere and space. This means, that horizon crossing indicators, which are fixed in the satellite structure, are most useful, when the satellite is rotating. However, the satellite will not be rotating because it could smear the photo during its task of taking images of the Earth. Horizon scanners, which are rotating horizon sensors, are not suitable for the satellite, because they include moving parts, take up more space and are more complex. Though horizon crossing sensors have no moving parts, they still require a complex construction including a housing, lenses and detectors.

An advantage of the horizon sensors compared to sun sensors is, that they can be used in eclipse, as they use infrared detectors. However, this does not compensate for the disadvantages and it has been decided not to use this sensor type.

Sun Sensors: Due to their low weight, small size, low power consumption and a wide range of possible designs, sun sensors are a suitable choice for a simple sensor type. The possible designs of sun sensors range from three axis sun sensors, which are determining the suns direction as a three dimensional vector, over the design of two axis sun sensors to simple light intensity sensors, such as photo-diodes. As some of these sensor designs are temperature dependent, they require temperature measurements to compensate for these effects. A disadvantage of many sun sensor designs is, that they not only measure the incoming sun light but also the light from Earth albedo. This will introduce an error in the measured Sun vector. Another disadvantage with sun sensors is, that they do not provide a Sun vector, when the satellite is in eclipse. However, the mission objectives only sets requrements for the attitude determination in sun light.

Sun sensors were chosen as suitable sensors to be implemented in the attitude determination system of the CubeSat. During tests of the attitude determination the Sun can be simulated using a strong light source.

Magnetometers: As the magnetic field of the Earth is well defined and strong in the low Earth orbit of the CubeSat, magnetometers could be used as sensors to determine the satellites attitude. A magnetometer is well suited for implementation in the attitude determination system of the satellite, due to its small size, low weight and low power consumption. When using a magnetometer on-board the CubeSat, it has to be taken care of disturbances in the measurements, especially when the sensor is implemented inside the satellite structure, surrounded by other subsystems and the electro-magnetic fields they produce. This will require a calibration of the magnetometer when the satellite finally is assembled, to reduce the effect of the constant electro-magnetic disturbances. Furthermore it will limit the use of the magnetometer to intervals, when the electro-magnetic coils of the satellite are deactivated. It has been decided to implement a magnetometer on-board the satellite to combine its output with the measurements of the chosen sun sensors and hereby to be able to provide a three-axis attitude determination. For tests of the magnetometer and the attitude determination, the Earth's magnetic field at ground level can be used.

Rate Gyros: Rate Gyros are available in small sizes and low weight. They have a low power consumption and would provide useful information about angular velocities of the satellite. This could proof to be very useful when combining the data with reference sensors and especially while stabilizing the

satellite or during detumbling. Based on this fact rate gyros have been used as sensors on other pico-satellites and CubeSats. However, it was chosen not to implement any rate gyros. This is to keep the design of the attitude determination system as simple as possible. Implementation of rate gyros would increase the time needed for development and test of hardware. Rate gyros would take up space inside the satellite structure and increase the time needed for integration. Instead of using rate gyros, angular velocities can be found by differentiation of the attitude.

3.3.4 Choice of sun sensor design

For the design of the sun sensors several options are possible. It is required that the sun sensors are of low weight and small sizes. Furthermore a simple design is required for higher reliability and because of the limited development time. When the satellite is in sunlight it is required, that, no matter which side faces the Sun, it should be possible to determine the direction to the sun.

The sun sensor designs considered are seen in figure 3.3 and are categorized as three axis-, two axis- and single axis-sensors.
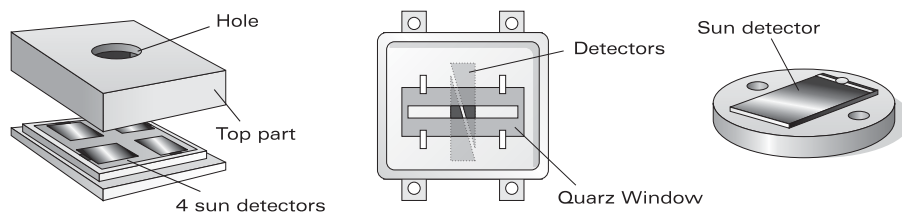

Figure 3.3: Three axis, two axis and single axis sun sensors are shown in this order from the left to the right

Three Axis Sun Sensors: With three axis sun sensors it is possible to determine the direction of the sun using only one sensor. In this design four rectangular photo-voltaic cells are used in a closed casing with an opening in the top part. In this sensor the output of each photo-voltaic cell will have to be measured and compared with each other to determine the angle of the incoming sunlight.

Instead of using four detectors an alternative would be to use a CMOS camera ship for the same purpose. A similar design is already being developed by Tokyo Institute of Technology for a satellite project (CubeSat Cute, 2002).

Two Axis Sun Sensors: This example of a two axis sun sensor uses two overlapped triangular pieces of silicon detectors, placed inside a aluminum housing. A quartz window with a slit is placed above the detectors and allows only a line of sunlight to hit the detectors. In this way it is possible to measure the direction of the sunlight in two axes by determining the difference of the output of the two detectors.

If this type of sun sensor would be used on the satellite, it would be necessary to use at least two of these on the side facing the sun, to determine the position of the sun in three dimensions.

A benefit of the two- and three axis sun sensors is, that they are independent of the temperature they are exposed to, as they use the difference between their single sensor parts, which all are exposed to the same temperature, to determine a direction of the sun.

Single Axis Sun Sensors: A Single Axis Sun Sensor determines the angle between incoming sunlight and an axis perpendicular to the surface of the sun sensor. This type is also called a cosine sun sensor as its output is reduced with cosine to the angle of incoming light. It will require a minimum of three cosine sun sensors positioned perpendicular to each other to determine a direction to the Sun. As the shape of the satellite is cubic and all sides are in an $90°$ angle to each other, this sensor design could easily be adapted to the CubeSat.

The spectral responsitivity of sun sensors are temperature dependent and since they will be exposed to a wide temperature range when placed on the surface of the satellite, it will be necessary to measure the temperatures at the sun sensors and compensate for temperatures in the sun sensor data.

The mechanical design and manufacturing of the sensors is simplest in case of the single axis sun sensors, as these only require a socket to mount a photo-voltaic cell and thermistor for temperature measurements. Manufacturing include the construction of a precise housing, exact alignment of sensor elements and in some case even cutting of silicon into precise triangular shapes.

As the satellite is shaped as a cube, the single axis sensor design is supported by the possibility of applying one cosine sun sensor on each side of the satellite. Each cosine sun sensor has a field of view of $180\,^{\circ}$, and using six sensors gives a full $360°$ field of view. Two- and three-axis sun sensors have a field of view which is limited by the height of their housings and size of their sensor elements. This means one of the three axis sun sensor or two of the two axis sun sensors would be needed on each of the side of the satellite. The total number of sun sensors needed on the satellite, when considering the different designs, is specified in table 3.2.

In the designs considered, one photo-voltaic cell is used in the single axis sun sensor, two photo-voltaic cells are used in the two axis sun sensor and four photo-voltaic cells are used in the three axis sun sensor. This means, that the same number of amplifier circuits would be needed to interface the sensors. This would result in a total of 24 amplifier circuits for interfacing three- or two axis sun sensors, while only six are needed for the single axis sun sensors. By using differential amplifiers for the two axis sun sensors the total amount of amplifiers could be reduced to 12. For the single axis sun sensors additional six temperature sensors would be required for temperature compensation of the sun sensor data. In table 3.2 the total number of amplifier circuits needed is specified for the three sensor designs.

	Single axis	Two axis	Three axis
Nr. of Sensors needed on CubeSat	6	12	6
Total of photo-voltaic cells	6	24	24
Temperature measurements	6	0	0
Amplifier circuits	12	12	24

Table 3.2: Key numbers for the three considered sensor designs

An advantage of the cosine sun sensors is, that the solar panels used for the power supply can be used as secondary sun sensors. In this way some redundancy is added to sun sensors on the five sides with solar panels. Solar panels are not considered to be accurate when used as sun sensors as Earth albedo affects the measurements. Earth albedo is Sun light reflected from the Earth and is near (30 ±5)% of the solar flux (Larson and Wertz, 1992). The Earth albedo will have the same effect on the single axis sun sensors, as they have on the solar panels. In the case of the two axis and three axis sun sensor designs, it will most often be possible to use sun sensors facing the sun which are not affected by Earth albedo.

It has been decided to use cosine sun sensors (single axis). This is first of all because of the simplicity in this design. This sensor type will have a lower accuracy due to Earth albedo, and it will be necessary to introduce an albedo compensation to reduce this error. However, the solar panels can be used as secondary sun sensors by using the same algorithms used for the primary sun sensors.

3.3.5   Choice of design for 3-axis magnetometer

The 3-axis magnetometer should be of low weight and small size. For the magnetometer design magnetoresistive integrated circuits from Honeywell are used. These are small, robust and have a low power consumption. They can be integrated on the print board, which is being developed for the attitude determination and control system. Interface electronics for the sensors will have to be implemented and tested for the sensors. This is a design choice, which is preferred over buying a magnetometer product with complete interface electronics. Existing magnetometer products would without doubt take up more space in the satellite than the chosen solution.

The sensor components from Honeywell are of types HMC1001 and HMC1002 (HMC1001-2, 1999). These are also used in the HMR2300r 3-axis strapdown magnetometer from Honeywell. In the datasheet for HMR2300r this product is suggested for for use in satellites (HMR2300r, 1999). This means that the HMC1001 and HMC1002 should be able to survive the harsh environment in low Earth orbit and during launch.

The HMC1001 and HMC1002 have integrated Set/Reset straps, which are used for resetting or setting the polarization of the magnetoresistive bridge circuit used for measuring the magnetic field. The Set/Reset straps can be pulsed with high negative or positive currents. The polarity of the magnetoresistive bridge is determined from the Set or Reset pulses. A *Set-Reset switching technique*, which uses the Set/Reset straps, will be implemented in order to achieve the following benefits described in (HMC1001-2, 1999):

- Operation of the magnetoresistive sensors in high sensitivity mode.

- Elimination of temperature offsets in sensors.

- Elimination of offsets in amplifier circuitry.

With the *Set-Reset switching technique* a Set pulse is first generated and magnetometer data is sampled. This is followed by a Reset pulse and a new sampling of data. The data sampled after the Reset and Set pulses is combined to create the magnetic field vector. The magnetometer electronics and the *Set-Reset switching technique* is described in higher detail in chapter 5.

In the case that a component stops working in the circuitry for generating Set/Reset pulses, the data from the magnetometer can still be used, but with a reduced accuracy. The sampled data from a Reset or Set pulse can be used directly for generating a magnetic field vector, but offsets due to temperatures or electronics may be introduced.

3.4   Attitude determination methods

With the chosen sensors for attitude determination, a vector to the Sun and a vector describing the magnetic field of the Earth in the SCB frame can be determined. An attitude determination method, which can determine the attitude from two vector measurements, is needed for the satellite. Determining the attitude of the satellite is equivalent to finding the rotational matrix describing the orientation of the SCB frame in the ECI frame. In (Bak, 1999) existing attitude determination methods are categorized as deterministic solutions and recursive estimation algorithms.

Deterministic solutions: These methods need at least two vector measurements obtained at a single point in time to determine a three-axis attitude. If a vector measurement is missing the deterministic solutions can not provide an attitude. Some common deterministic solutions are: TRIAD, SVD, Q-method, FOAM, QUEST and ESOQ (Markley and Mortari, 1999) (Markley, 2002).

Recursive estimation algorithms: The recursive estimation algorithms use both present and past measurements for determining the attitude. The Kalman filter or the extended Kalman filter are recursive estimation algorithms utilizing a state-space model of the system (Grewal and Andrews, 2001).

Many deterministic attitude determination methods exist, which differ in accuracy and computational burden. The only recursive estimation algorithm considered here is the Extended Kalman filter.

3.4.1   Choice of Attitude determination method

The choice of attitude determination method is based on, what is required of the attitude determination. Secondly it is a clear advantage if the attitude determination is simple to implement and test.

The attitude determination using a deterministic solution will be simpler and more straight forward to implement and test. It uses sensor readings at one given point in time and does not include dynamics

of the system. When implemented in the satellite with sun sensors and magnetometer, the deterministic attitude determination can be tested by applying known sensor inputs to the system and by observing, if the attitude is determined correctly. The Kalman filter can not be tested in this simple way, because it takes the dynamics of the system into account. The deterministic methods have some shortcomings compared to the extended Kalman filter, which are mentioned below. If these shortcomings are acceptable a deterministic attitude determination method may be suitable.

The deterministic methods require at least two vector measurements to determine the attitude. This is a problem when the satellite is in eclipse and if the measured magnetic field vector and the Sun vector are collinear.

When the satellite is in eclipse, the Sun vector measurement can not be used. However, a three axis attitude determination is needed only when the satellite is in daylight. In the power save mode (daylight) and in camera mode both vector measurements are available from the sensors.

If the magnetic field and the sun vector are collinear an attitude can not be determined using a deterministic solution. As described in appendix E the angle between the magnetic field vector 700 km above Denmark and the equatorial plane varies approximately from $30.5\,^\circ$ in the south of Denmark to 37° in the north. The angle between the equatorial plane and the incoming sun light will range from $+23.4\,^\circ$ to -23.4° during one year. This means that the sun vector and magnetic field vector will not become collinear over Denmark. However, the albedo correction needed to compensate for Earth albedo may cause the magnetic field vector and sun vector to become collinear. This is due to the effect, that the direction of the sun vector measured with the sun sensors, is changed by the Earth albedo.

If the sun vector and magnetic field vector are found to be collinear, the last known attitude may be assumed until the vectors are no longer collinear. A collinearity is assumed not to last longer than 1 or 2 minutes, due to the speed of the satellite. It may be possible, when planning the flight plan from the ground station, that a photo is not acquired when there is possibility for collinearity.

Even though collinearity may cause a deterministic attitude determination to occasionally fail, it has been decided that this type of attitude determination is suitable and will be used for the attitude determination. Different deterministic solutions have been used for attitude determination in satellites. The choice of which deterministic solution to use is determined in chapter 10.

The choice of a deterministic attitude determination is based on the decision, that no attitude control is to take place in eclipse. This decision was made early in the project in order to minimize power consumption in eclipse. However, the solar panels purchased for the power supply are triple junction and also convert light in the infrared spectrum into electrical power. This means that infrared radiation from the Earth also will supply the solar panels with energy even in eclipse (Lazar et al., 2002). In addition to this, the attitude control would benefit from being able to actuate also in eclipse. For this reason it was decided to supplement the deterministic attitude determination with an extended Kalman filter.

With the chosen sensor configuration it would be possible to estimate the attitude in eclipse when using an extended Kalman filter. Attitude determination using an extended Kalman filter and magnetometer data has been described in (Bak, 1999) and in (Humphreys, 2002), where data from solar panels is used in addition to magnetometer data, to make the extended Kalman filter converge faster. One difficulty with implementing an extended Kalman filter will be determining a precise inertia matrix. However, if the extended Kalman filter fails, the deterministic solution can be used instead.

To sum up the choice of attitude determination: It was chosen to implement a deterministic method, due to simplicity and because the attitude determination is not required in eclipse. Later it was chosen to supplement the deterministic solution with an extended Kalman filter, because the solar panels purchased for the satellite, will make attitude control in eclipse possible.

3.4.2 Accuracies of reference models

Accuracies of the sensors will have different effects on the deterministic and recursive method. In addition to the vector measurements made with sensors in the SCB frame, reference models for determining additional vectors in the ECI frame are needed. Reference models are needed of the magnetic field and for

determining a direction to the Sun. In addition an orbit model is needed to provide a position in orbit for the magnetic field model.

The sun sensors are expected to have a low accuracy due to Earth albedo. The deterministic method will always rely on both sensors, which means that a good albedo correction is needed, to compensate for large errors in the sun sensors. The albedo correction must reduce the sun vector error to secure an error of the attitude determination lower than $8\,\sigma$.

The Kalman filter may rely on magnetometer data to determine the attitude, this diminishes the importance sun sensor data and albedo correction. Instead the magnetic field model for determining a magnetic field vector in the ECI frame becomes important.

In (Wertz, 1978) angular errors (RMS) for magnetic field models (IGRF) of orders 1 to 7 in an altitude of 300 km, are specified to $0.1°$ to $10°$. Accuracy improves with rising altitude. It is decided that the RMS error of the magnetic field model to be implemented in the on-board computer should be lower than $1°$. The RMS error of the sun model should be well below $1°$ and will be negligible compared to Albedo errors. Low accuracy of the orbit model will affect the accuracy of the magnetic field model. The accuracy of the orbit model will decrease over time. Based on initial simulations with existing orbit models, it seems that an orbit model with a maximum position error less than 100 km after one week should be expected.

3.5 Attitude determination architecture

It was decided to develop a deterministic and a recursive attitude determination to be implemented. This gives the opportunity to test both attitude determination methods when the satellite is in orbit. Three different operation of the attitude determination have been defined. The *primary operation* uses a combination of the extended Kalman filter and the deterministic solution. The *secondary operation* uses entirely the deterministic solution and the *tertiary operation* uses only the Kalman filter. Algorithms used in the attitude determination are described in the following:

Process magnetometer data: Raw magnetometer data sampled is processed to a measured magnetic field. This includes necessary Set/Reset switching, calibration, taking account for errors in magnetometer and creating a unit vector.

Process temperature data: The temperature sensors have a nonlinear relation between sensor output and temperature. Processing temperature data includes necessary filtering, determining temperature from sensor readings and taking account for errors in temperature sensors.

Process sun data: Both sun sensors and solar panels can be used for supplying sun data. Processing sun data includes selecting primary or secondary sensors, necessary filtering and calibration.

Temperature correction: This algorithm corrects sun data based on measured temperatures.

Sun model: This model determines the direction vector to the Sun in the ECI frame based on julian date.

Albedo correction: The sun sensors are sensitive to Earth albedo. This algorithm adds a contribution from Earth albedo to the Sun vector from the sun model.

Orbit model: The orbit model determines the position of the satellite based on julian date.

Magnetic field model: The magnetic field vector in the ECI frame is determined based on the satellite position.

Deterministic attitude determination: Vector measurements in the SCB frame and corresponding vectors in the ECI frame are used in the deterministic attitude determination. Angular velocities of the satellite will be found by differentiation of the attitude.

Extended Kalman filter: The extended Kalman filter estimates angular velocities and attitude given sensor measurements, models of the dynamic system and statistical descriptions of uncertainties associated with these.

Selector: This algorithm is used in the *primary operation* for selecting either the deterministic or recursive solution.

For the orbit model and the sun model the time given as Julian date is required. The DHCS synchronizes its clock after a reboot, when communicating with the ground station. This clock is given i Unix time, and is converted to Julian date when used in the ADS.

3.5.1 Primary operation

The *primary operation* is illustrated in figure 3.4. This will be the default operation setting, which the satellite starts in after deployment or system reboot.
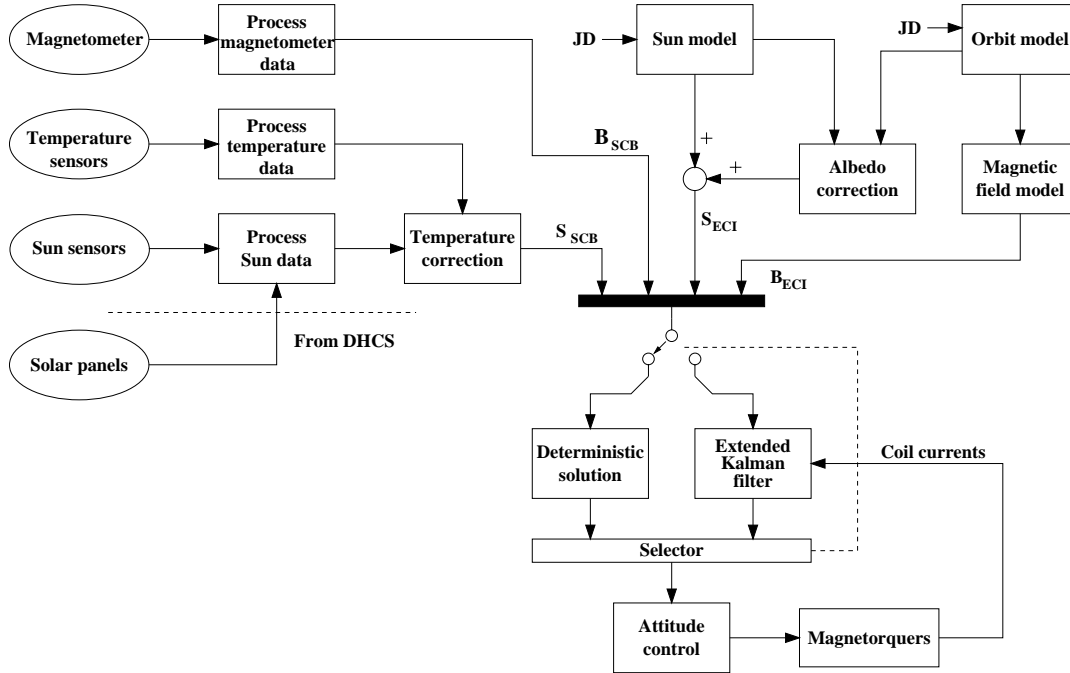
Figure 3.4: The oval circles represent sensors and rectangles are algorithms for attitude determination. The attitude and angular velocity are provided to the attitude control

Criteria for selecting determination method

The selection in block *Selector* of using either the deterministic attitude determination or the extended Kalman filter is defined as:

- An initial attitude to be used for the extended Kalman filter, is found by first finding the deterministic solution. The deterministic attitude determination only has to use one sampled set of sensor data, to determine the attitude, after which the *primary operation* uses the extended Kalman filter.

- If the extended Kalman filter for 30 minutes does not converge as expected, the deterministic solution will be used to re-initialize the extended Kalman filter. If this takes place in eclipse, the deterministic solution will be found as soon as the satellite leaves eclipse.

- The magnetic field vector and sun vector can be found to be collinear when a deterministic solution is required. If this happens the deterministic solution is used until a solution is found. If five min-

utes pass without finding the deterministic solution, the extended Kalman filter uses a default initial attitude instead of the deterministic solution.

3.5.2 Secondary operation

The secondary operation is intended for using only the deterministic attitude determination. This is useful if the extended Kalman filter against expectation should fail.
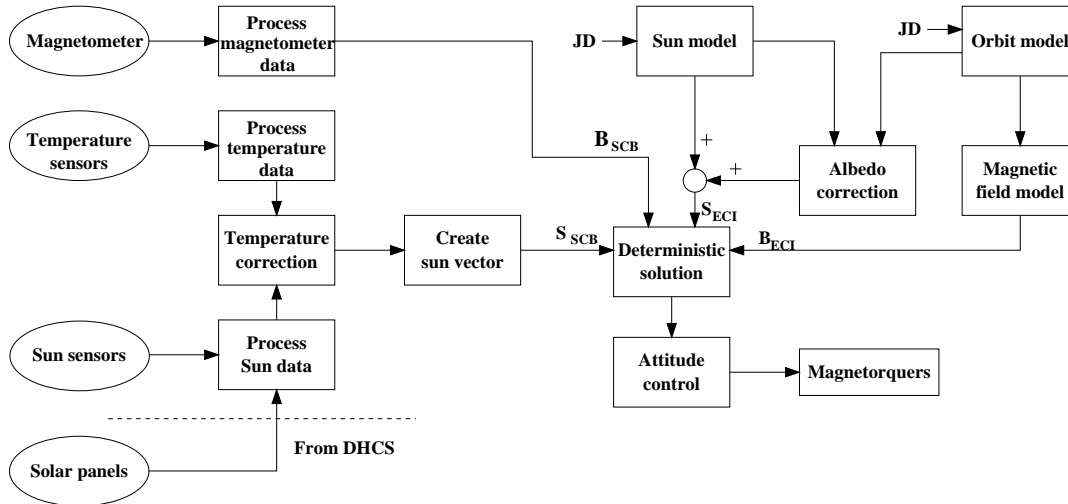

Figure 3.5: Secondary operation uses only a deterministic solution. Oval circles represent sensors and rectangles represent algorithms. Attitude and angular velocity are provided to the attitude control

3.5.3 Tertiary operation

The tertiary operation uses only the extended Kalman filter. Default values are used for initializing the filter, instead of using the deterministic solution as in the primary operation. The operation may be used for testing the extended Kalman filter alone. This operation may also be useful if both primary and secondary sun sensors are lost, making it impossible to determine the attitude with the deterministic method.

3.6 Configuration of ADS

It must be possible to re-configure the system from its default settings. The following settings shall be possible to update from ground:

Two-Line Elements: Kepler elements used for updating the orbit model. These shall be obtained when available from NORAD in order to asure accuracy of the orbit model.

Black-list sensors: Used for excluding faulty sun sensors, solar panels, magnetometer axes and measurements of currents through coils. Faults are detected either when studying housekeeping.

Magnetometer setting: For selecting to use or not to use *Set-reset switching technique* in magnetometer.

Calibration factors for sun sensors: Calibration factors to compensate for differing photo sensitivities in the six sun sensors.
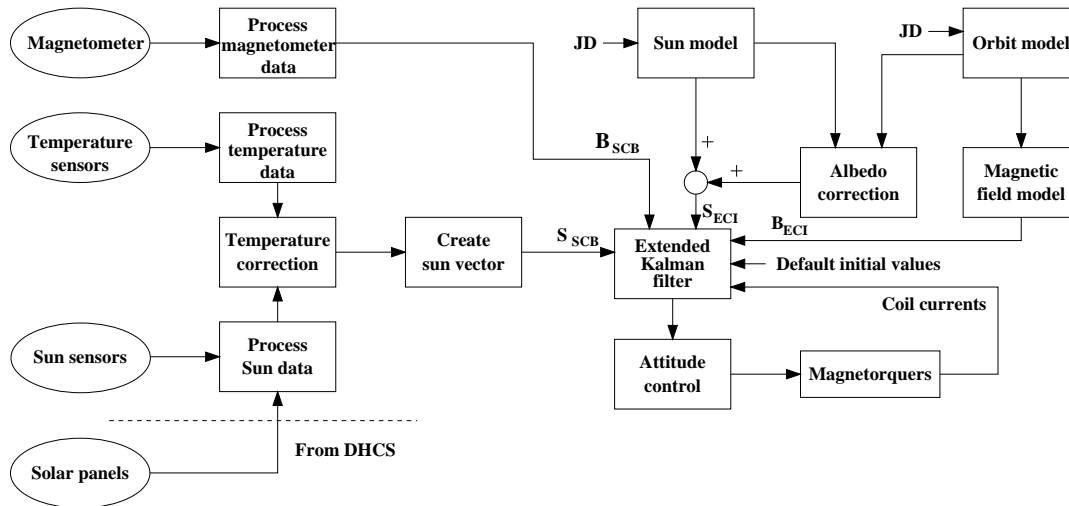
Figure 3.6: Tertiary operation uses only the extended Kalman filter. Oval circles represent sensors and rectangles represent algorithms. Attitude and angular velocity are provided to the attitude control

Calibration factors for solar panels: Calibration factors to compensate for differing photo sensitivities of solar panels with respect to sun sensors and solar panels.

Calibration factors for magnetometer: Calibration factors to compensate for constant magnetic fields due to satellite structure.

Albedo correction ON/OFF: Switch albedo correction on or off.

Sunlight threshold: Threshold for determining if the satellite is in eclipse, when comparing to the sum of sun sensor data.

Operation mode: Choice of which operation mode to use. The default is *primary operation*.

The two-line elements must be updated in the ADCS when possible to ensure an accurate orbit model. The rest of the configurable settings are for repairing the ADS. The ADS can survive a number of errors in the different sensors. If a sensor fails it is necessary to use a redundant sensor or re-configure the system to determine the attitude without the sensor. It has been decided to keep the level of autonomy in the ADS down in order to keep the design simple. Errors in sensors should be detected and reported in the housekeeping data, which is send to ground. Re-configuration of the ADS is then to be made from ground. If a sensor stops working properly it may result in failure of the attitude determination followed by the attitude control. If this happens before or during the satellite takes a photo, the photo may be off target. One or two succeeding photo jobs may fail due to the error, before reconfiguration is made from ground.

3.7 Summary

In this chapter a sensor configuration consisting of a three-axis magnetometer and six cosine sun sensors was chosen. It was decided that a suitable sensor type for the magnetometer is the HMC1001/2 product from Honeywell. The sun sensor designs shall be kept simple in order to reduce development time. The chosen design require temperature measurements which will have to be implemented with the sun sensors.

It was first chosen to use a deterministic attitude determination method. Later in the project it was decided to also implement an extended Kalman filter. An attitude determination architecture was described in section 3.5. When considering errors in the ADCS it was decided to keep the level of autonomy low.

Errors should be detected when studying/processing housekeeping data in ground. A small number of settings will be made available, in order to reconfigure the ADS.

chapter 4

Requirements and test specifications

In this chapter the requirements of the attitude determination are specified for both hardware and software. First the hardware and software parts are identified in section 4.1. In section 4.2 the requirements are defined. The test specifications are given in section 4.3.

4.1 Breakdown into Hardware and Software

The attitude determination to be implemented into the satellite consists of hardware and software parts. These are described in the following sections.

4.1.1 Hardware

The attitude determination consists of the following hardware parts:

- Sun sensors

- Temperature sensors

- 3-axis magnetometer

- Micro controller for interfacing sensors and actuators

- Micro controller (OBC)

Sensors consist of the sensor component and interface circuitry. The OBC is used for the attitude determination algorithms while another micro-controller is used for sampling sensors and generating control signals to the actuators. The solar panels used for the power supply are used as secondary sun sensors. No requirements or tests are specified for the solar panels with respect to the attitude determination system.

In chapter 3 suitable sensor types have been determined for the magnetometer, temperature sensors and sun sensors. Requirements are specified for sample time, noise and error for the sensors. The system is slow reacting and a total sampling time of the sensors of 300 ms is both adequate and realistic to implement. The sensing parts of temperature sensors and magnetometer are in fact resistors changing with a slowly varying temperature and magnetic field, respectively. For this reason noise on these sensor readings can be expected and required to be lower than the resolution of the A/D-converter sampling the signals.

The choice and development of OBC micro controller was done by (Clausen et al., 2002). Accordingly no requirements are defined for the OBC here.

A simple set of requirements are defined for the micro-controller to interface sensors and actuators. For the purpose of test and development the micro controller used should be available in EPROM or EEPROM version. For the final version the of the electronics a surface mounted PROM version should be available. The microcontroller will be used for sampling sensors, executing control algorithms and interfacing actuators.

4.1.2 Algorithms for attitude determination

The attitude determination algorithms consist of algorithms for processing sensor data, models for determining a Sun vector and a magnetic field vector in the ECI frame and finding the attitude and angular velocities to the corresponding measured vectors in the SCB frame. The following are the algorithms for attitude determination.

- Process sensor data

- On-board Sun model

- On-board Orbit model

- On-board Magnetic field model

- Albedo correction

- Deterministic attitude determination

- Extended Kalman Filter for attitude determination

For simulation of the attitude determination, true reference models are needed for sun model, orbit model and magnetic field model. These true reference models will be used to simulate the true environment against the on-board models. The true reference models are included in the requirements and test specifications for sun, orbit and magnetic field models.

4.2 Requirements

In the following section, requirements and test specifications are listed for the ADS hardware and algorithms. Requirements for hardware are marked with an *H*, while requirements for algorithms implemented i software are marked with *S*. Test specifications will accordingly be marked with *TH* and *TS* for hardware and software, respectively. The test specification *TH1.1* specifies how to test requirement *H1.1* and so forth.

4.2.1 ADS Hardware

General Requirements

H1.1 **Mass Budget:** The total weight of the ADCS including circuit print, sensors and coils shall not exceed 90g.

H1.2 **Power Budget:** The power consumption of the ADCS subsystem (OBC not included) shall be below 450mW, when it is in power save (Sunlight), camera or initialization mode, and below 75mW when in fail safe or power save mode (Eclipse). This corresponds to 5V and 90mA in active mode and 15mA in fail safe or power save mode.

H1.3 The ADS shall fit into the available design space as specified in chapter 6.

H1.4 The hardware components used must be able to survive in LEO environment, considering the temperatures, radiation and vacuum and still be fully operational. Details in this requirement have not been specified at writing time.

H1.5 The hardware components must not cause outgassing at all or as little as possible when exposed to vacuum, in order to avoid that particles deposit on the camera lens, solar panels and sun sensors.

Sensor Requirements

H2.1 The max measurement error of each primary sun sensor, including measurement errors and misalignment from mounting, shall be lower than $4\,^\circ\sigma$.

H2.2 The max measurement error of the magnetometer, including measurement errors and misalignment from mounting, shall be lower than $1\,^\circ\sigma$.

H2.3 The max measurement error of the temperature sensors shall be sufficiently low to ensure requirement H2.1. The temperature interval to measure is determined according to the same requirement.

H2.4 A photo sensitivity for the sun sensors shall be determined for the sun sensors, when exposed to extraterrestrial sunlight.

H2.5 A temperature coefficient shall be determined for the sun sensors, to be used in temperature compensation.

H2.6 Calibration procedures should be performed for the magnetometer, when integrated in engineering and flight model, in order to reduce effects of misaligment and magnetic distortions, this should be done to fulfill requirement H2.2.

Micro-controller Requirements

H3.1 The micro-controller interfacing the sensors shall sample the sensor data from the three sensor types.

H3.2 The micro-controller shall on request send the data from the sensors on the I^{2}C bus to the OBC.

H3.3 The micro-controller shall interface actuators and execute control algorithms.

H3.4 For test purposes EPROM versions of the micro-controller shall be possible to implement on prototype and engineering model version of ADCS circuit print board.

4.2.2   ADS Algorithms on the OBC

The requirements for the attitude determination have been set up based on the mission analysis for the satellite, described in chapter 2. Here the pointing accuracy of the ADCS was set to be $8\,^\circ\sigma$. Accuracies of on-board reference models were discussed in section 3.4.2.

Real-time thread Requirements

S1.1 The ADCS-thread running on the OBC shall be executed periodically in intervals of 1 second.

S1.2 The ADCS-thread shall via I^{2}C bus request, receive and save housekeeping data including sensor readings and current measurements from the coils.

S1.3 The ADCS-thread shall receive requests from DHCS for housekeeping data and reply with the data.

S1.4 The ADCS-thread shall receive and save solar panel readings from the DHCS.

S1.5 The ADCS-thread shall receive and respond to requests from the DHCS for changing mode.

Configuration of ADS

S2.1 It shall be possible to save new TLEs for use in the orbit model.

S2.2 It shall be possible to specify if a sensor is not to be used for the attitude determination (black-list).

S2.3 It shall be possible to specify if the magnetometer shall use *Set-Reset switching technique* or not.

S2.4 It shall be possible to upload six new calibration factors for the six primary sun sensors.

S2.5 It shall be possible to upload five new calibration factors for the solar panels.

S2.6 It shall be possible to upload a total of six new calibration factors for the three magnetometer axes (Scaling and Offsets).

S2.7 It shall be possible to switch off the albedo correction algorithm.

S2.8 It shall be possible to update the sunlight threshold value for determining, if the satellite is in eclipse.

Measurement Processing Requirements

S3.1 Data sampled from the temperature sensors shall be converted to temperature values.

S3.2 Data sampled from the sun sensors shall be calibrated to compensate for differing photo sensitivities of the sensors. This should be done to secure requirement H2.1.

S3.3 Data sampled from the solar panels shall be calibrated to compensate for differing photo sensitivities with respect to the primary sun sensors.

S3.4 Compensation of sun sensor or solar panel data shall be performed.

S3.5 Magnetometer data shall be calibrated to compensate for constant magnetic fields in structure and to secure requirement H2.2.

S3.6 The ADS shall transform the measurement data into vector measurements, describing the direction of the sun and the Earth's magnetic field, to be used in the attitude determination, without violating requirement H2.3.

On-board reference Models Requirements

S4.1 The satellite shall have knowledge of the position in the ECI frame by using an on-board orbit model, which includes updated TLE sets. The error of the orbit model using a one week old TLE shall not exceed 100 km off position.

S4.2 An on-board magnetic field model shall determine the direction of the magnetic field in the satellite position with a RMS error less than $1°\sigma$.

S4.3 An on-board Sun model shall determine the direction to the Sun in the ECI frame with a max error less than $1°\sigma$.

S4.4 An albedo correction, shall compensate for the fact, that the measured sun vector includes the light of Earth albedo. This correction shall work well enough to ensure that the attitude can be determined within $8°\sigma$ for in the deterministic attitude determination.

The Attitude Determination Requirements

S5.1 Using the deterministic attitude determination the attitude and angular velocities of the satellite shall be determined with respect to the ECI frame. Maximum error of the attitude determination shall be within $8°$ σ.

S5.2 The deterministic solution shall be able to handle collinearity or cases of temporally unavailable data by using the last determined attitude as current data.

S5.3 Using the extended Kalman filter attitude and angular velocities of the satellite with respect to the ECI frame, shall be determined with maximum errors lower than $8°$ σ. This also includes the ability of the ADS to change between the deterministic attitude determination and the extended Kalman filter, as specified in section 3.5 for primary operation.

S5.4 The attitude determination in combination with the attitude control, shall ensure a pointing accuracy of $8°\sigma$.

4.3 Test specifications

The test specifications have the purpose of specifying which conditions the tests shall fulfill, in order to test if a requirement has been fulfilled. However, the specifications do not go into details regarding common laboratory and test procedures. The test specifications also works as a guide on how to test if requirements are fulfilled. When referring to ADCS hardware in the following, this includes sensors, actuators and the micro-controller for interfacing these. Though algorithms for attitude determination will be implemented into the OBC, the test specifications for the OBC are not included here. Test of the OBC has been the responsibility of (Clausen et al., 2002).

The test specifications will be marked with an *TH* or *TS* for hardware- and software-test respectively.

4.3.1 Test of hardware

Test - General requirements

TH1.1 The ADCS hardware (OBC not included) should be weighed to secure that requirement H1.1 is fulfilled.

TH1.2 The power consumption of the ADCS hardware should be measured when data is sampled from sensors and control signals are generated for the coils, corresponding to camera mode. The power consumption should also be tested when no sampling of sensors and no actuation takes place corresponding to fail safe mode. The power consumption should not exceed requirement H1.2

TH1.3 It should be tested that the ADCS hardware does not violate requirement H1.3. This is done when implementing engineering and flight model version of ADCS subsystem into the satellite structure with other subsystems.

TH1.4 The engineering model with all subsystems integrated, should be tested with respect to temperatures, vacuum, shock, radiation and single-event upsets. Details for these tests have not been specified at this point, because they depend on which test equipment will be available, the number of personnel and available time. However, ADCS hardware should be designed with consideration on requirement H1.4.

TH1.5 No tests will be made to validate if requirement H1.5 concerning outgassing is fulfilled. Outgassing is avoided in the choice of components.

Test - Sensor requirements

TH2.1 Accuracy of sun sensors are tested by finding sample points on the cosine characteristic for the sensors and comparing to a perfect cosine curve. The sensors are exposed to incoming light while sampling the output from the sensors. The orientation of the tested sensor is changed so the angle between incoming light and a normal to the sensor ranges over $\pm 90\,°$. Albedo is not simulated in any of these tests and the sun sensors are tested with one single light source.

Prototype print: The sun sensors are rotated on a rotating plate, which has an inbuilt protractor. For each $5°$ a data sequence is sampled from the sensors using the micro-controller. Data from the micro-controller is logged using a PC. Only a couple of sun sensors will have to be tested, and that without being mounted in sockets. Sun sensor error, when testing the prototype, does not include misalignment, in order to fulfill requirement H2 1. The test will not include temperature compensation, so tests should be performed when temperatures does not vary more than $\pm 1\,°$Celsius.

Engineering and flight model: All primary sun sensors are mounted on the satellite structure. The structure shall be rotated $360°$ with respect to a constant light source, in which four of the sun sensors will be exposed to incoming light of angles ranging $\pm 90\,°$. It is necessary to have know the rotation of the satellite for each sample of sun sensor data, for this the calibrated magnetometer data shall be used as reference. Sensor data is sampled with the micro-controller and saved as housekeeping data on the OBC. When having performed a rotation exposing four different sensors to light, the structure is rotated $90°$and a rotation is performed exposing also the remaining two sun sensors. Data can at the same time be samled from the solar panels, thus giving an idea of their performance as secondary sun sensors.

TH2.2 The accuracy specified in requirement H2.2 for the magnetometer, is tested by going through a calibration procedure for the magnetometer, using the *Set-Reset switching technique* specified in (HMC1001-2, 1999). The magnetometer is rotated in the x-y plane and in the x-z or y-z plane while logging data. After rotation has been performed the logged magnetometer data is processed in Matlab. Scaling factors for x, y and z axis are found together with offsets caused by constant magnetic fields from the satellite structure and other subsystems, as described in (Caruso, 1998). Calibrated data for rotations in the two planes should result in complete circles. Errors of the magnetometer will be sampled data deviating from these circles.

Prototype: Test of the magnetometer prototype is to validate functionality and accuracy. Data sampled with the micro-controller interfacing the sensors does not have to be transferred to the OBC when testing the prototype print. Data from the micro-controller is logged using a PC.

Engineering and flight model: First it is necessary to secure that the three axes of two sensor components HMC1001 and HMC1002 are mounted perpendicular to one and another. If this is not the case corrections should be made to secure this. Second, a calibration procedure shall be performed to find calibration constants for removing magnetic distortion caused by constant magnets in the satellite. It is important that rotations of the magnetometer is performed with a constant axis of rotation. Also it is important that the measured magnetic field does not change strength or direction during the test. The test shall be performed with all subsystems integrated in the satellite. The initial orientation of the satellite, with respect to the surrounding magnetic field, shall be known with the purpose of determining any rotation between the magnetometer and the SCB frame. The calibration procedure shall be performed in the x-y, x-z and y-z plane for the magnetometer.

TH2.3 Accuracy of the temperature sensors, as specified in requirement H2.3 should be tested over their temperature range. Sampled temperature data is compared with measurements from a thermometer.

Prototype: Data sampled with the micro-controller interfacing the sensors does not have to be transferred to the OBC when testing the prototype print. Data from the micro-controller is logged using a PC.

Engineering and flight model: Temperature sensors are mounted in sockets together with primary sun sensors on the satellite structure. Tests should be performed where temperature data is sampled and stored as housekeeping, while exposing the satellite to temperatures in their full temperature

range. Temperatures shall be compared to temperatures measured with a thermometer (accuracy $\pm 1^\circ$ C). Each time a temperature is measured with the thermometer a sun sensor should be exposed to a light blink. This is in order to find the corresponding temperature sample in housekeeping, when examining data after the test. Thermometer should be noted in temperature intervals of 5 $^\circ$ C

TH2.4 **Prototype:** The photo sensitivity of the sun sensors when exposed to extraterrestrial sunlight shall be determined, by exposing the sensors to light with a similar light spectrum. Data is sampled from sensors. This test is only needed for a few photo voltaic cells of the type to be used in the sun sensors, and should be performed before design and production of engineering and flight model print. The test shall determine the output range from the sun sensors.

Engineering model: The photo sensitivity of each sun sensor mounted on the satellite structure shall be determined, with the purpose of determining calibration factors for the sun sensors. This is accomplished by observing peak values for sun sensors sampled in the test specified by TH2.1.

TH2.5 The temperature coefficient of the sun sensors is found by exposing a few sun sensors to a constant light, while changing the temperature in the range -40 $^\circ$C to +80°C. Meanwhile the output from sun sensors is sampled and logged on a PC. This test is only needed for a few photo voltaic cells of the type to be used in the sun sensors.

Test - Micro-controller Requirements

TH3.1 Requirement H3.1 is fulfilled if the tests TH2.1 to TH2.3 are performed to satisfaction.

TH3.2 Requirement H3.2 is fulfilled if the tests TH2.1 to TH2.3 are performed to satisfaction. For the prototype ADCS hardware, it has been decided to only test that communication is possible over the I^{2}C bus. It is not necessary to test by sending sampled sensor data.

TH3.3 Requirement H3.3 is to be handled by (Frederiksen et al., 2002).

TH3.4 Requirement H3.4 is not to be tested.

4.3.2 Test of algorithms

The purpose of the tests of the on-board algorithms is to verify their performances. This is obtained by comparing the output of the algorithms with either real data or input values used in a simulation.

The error of the models algorithms is finally calculated as an error angle between the real or most optimal outputs and the outputs given by the algorithms and models.

Test - Real-time thread Requirements

TS1.1 The periodic execution of the ADCS-thread, according to S1.1, is tested by going through the time stamps in housekeeping from the test of sensors.

TS1.2 Requirement S1.2 is fulfilled if test TS1.1 is performed successfully. No data samples should appear to be missing, and sensor data should evolve as expected.

TS1.3 If DHCS can sample housekeeping from the ADCS thread, this one is tested. Sampling should be performed over a long period of time (Hours, days - TBD)

TS1.4 In the configuration possibilities all primary sun sensors shall be deactivated. Then an attitude shall be determined using solar panel data. This is easiest tested with a deterministic attitude determination.

TS1.5 The ADCS shall respond in housekeeping data, which mode it is in.

Test - Configuration of ADS

TS2.1 The different tests connected to the configuration of the ADS and concerning the functionality of the different options mentioned in the requirements of S2 will be tested as a part of the communication with the CDHS. All these requirements will be tested one by one during the integration of the ADS on the OBC.

Test - Measurement Processing Requirements

TS3.1-5 The conversions from sampled measurement data to temperature values given in requirements S3 are tested, by applying known inputs to the ADS to simulate sensor data, and by reading the output given. This output is accordingly verified by its relation to the given input.

Test - On-board reference Models Requirements

TS4.1 **Orbit Model:** The orbit model used for the truth model and for the on-board orbit model, will be tested by using TLE parameters and position data from the Ørsted satellite. Existing TLE sets for Ørsted are used for the orbit models. The calculated satellite positions over this time interval is compared to position data measured by GPS on-board the Ørsted satellite over the same time interval. Hereby the two orbit models are validated including the error, which occurs when using the same TLE parameters for one week without any update. Here the requirement regarding the accuracy given in requirement S4.1 has to be fulfilled.

TS4.2 **Magnetic Field Model:** The on-board magnetic field model and a model for simulating the true the magnetic field shall be tested with data from the Ørsted satellite. This is achieved by using position data of Ørsted obtained by the satellites GPS as input to the magnetic field models. The direction and intensity of the magnetic field measured by the Ørsted Satellite in the same orbital path is compared to the outputs of the magnetic field models. The requirement S4.2 has to be fulfilled for the magnetic field model used on-board the satellite.

TS4.3 **Sun Model:** The on-board sun model and the sun model used for determining the true direction to the Sun in simulations, shall be tested by comparing to the output results for existing sun models. The test shall be performed for the whole year 2003 and fulfill requirement S4.3.

TS4.4 **Albedo Correction:** The RMS errors caused by Earth Albedo on the sun sensors have to be simulated. Then an albedo correction shall be introduced and the resulting RMS error is determined by simulation. These simulations have to be performed with the inertial pointing satellite illustrating power save mode and camera mode. For power save mode one corner of the satellite will point towards the Sun, and for camera mode, the satellite will point the camera towards the Earth and away from the Sun. The day of simulation will be the 21st of June year 2003, which is shortly after the satellite has been launched.

Test - Attitude Determination Requirements

TS5.1 **Deterministic Attitude Determination:** To test the performance of the deterministic attitude determination the following test scenarios shall be used. The attitude determination shall fulfill requirement S5.1.

a First, verify that the deterministic attitude determination works, by determining the rotation between two vector pairs, which have been rotated with a known rotation. Secondly, the same test is performed with an error added to one of the vectors, corresponding to the expected albedo error.

b A simulation of the satellite in orbit, shall be performed where the deterministic attitude determination is used and no albedo errors on sun sensors are included. The simulation shall be performed for the 21st of June year 2003, which is shortly after the satellite has been launched.

Due to the tilt of Earth rotational axis, the risk of collinearities between sun vector and magnetic field vector, is greatest in the vicinity of Denmark at this time of the year.

c The test TS5.1.1b is performed again, but this time with albedo errors on sun sensors and Albedo correction to lower the effects of albedo.

TS5.2 **Collinearities of magnetic field and sun vectors:** Requirement S5.2 is tested in the scenarios TS5.1b and TS5.1c.

TS5.3 **Extended Kalman filter:** Attitude determination using the extended Kalman filter is tested with the following scenarios. The scenarios correspond to primary and tertiary operation, described in section 3.5. Purposes of the tests are not only to test the extended Kalman filter but also to make fine tuning. This is done as part of the simulations described below.

Satellite dynamics, disturbance torques, orbit position, magnetic field and direction to Sun shall be simulated and used as inputs to the attitude determination. Errors of sun sensors and magnetometer shall also be simulated. The simulations are performed for the 21st of June, year 2003.

a A simulation is performed corresponding to tertiary operation, where only the extended Kalman filter is used. For the initial attitude state an error of 180° is used. Through the entire simulation both primary sun sensors and magnetometer is used.

b A simulation similar to TS5.3a shall be performed, with the one difference that no sun sensors are used. This is in order to observe how the filter converges without sun sensor data.

c A simulation shall be made of primary operation, where the extended Kalman filter uses initial states determined with the deterministic attitude determination.

d Deterministic attitude determination and attitude determination using the extended Kalman filter shall be combined with attitude control, and simulations using primary, secondary and tertiary operation for the attitude determination, shall be performed for the entire attitude determination and control system. Requirement S5.4 shall be fulfilled for the complete attitude determination and control system.

4.4 Summary

Requirements have been set up for the development and test of the ADS for the AAU CubeSat. These include the requirements for the hardware and especially its precision. Further the requirements for the software algorithms have been set up outlining the necessary steps to be taken. An overall requirement for the complete ADCS system consists of a pointing accuracy of 8°.

Following the list of requirements the test specifications have been defined. Following these it will be possible to verify if the requirements set up are fulfilled or not. To simplify and optimize this way of validating the parts developed or designed the test specifications have been defined using the same numbers as the requirements connected to them.

chapter 5

Attitude determination hardware

This chapter describes the implementation of three different sensors used for attitude determination. A 3-axis magnetometer for measuring the Earth's magnetic field, six cosine sun sensors for measuring the direction to the Sun and six temperature-sensors for measuring the temperatures of the sun sensors. Section 5.1 gives a general view of the hardware. In the sections 5.2 to 5.4 each sensor type is described. For each sensor the environment to be measured, the sensor component and the circuitry for interfacing it to the PIC micro-controller are described. In section 5.5 the PIC micro-controller is described together with pseudo code for sampling the sensors.

5.1 General view of hardware

A block-diagram of the hardware used for attitude determination and control can be seen in figure 5.1. The hardware for attitude determination is divided into detector, interface electronics, the PIC micro-controller and the OBC.
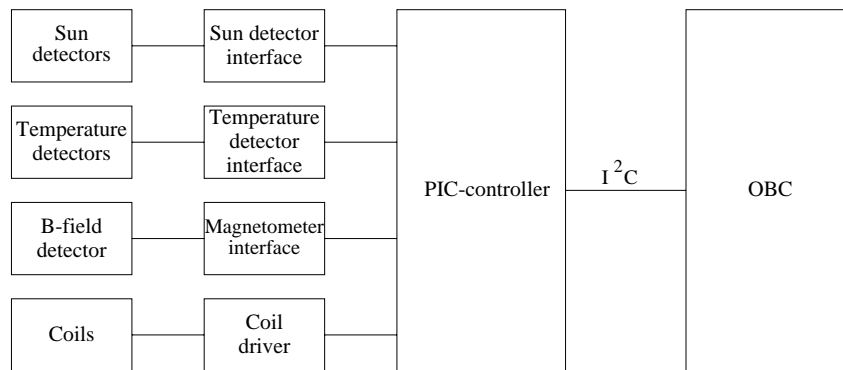

Figure 5.1: The attitude determination is executed on the OBC and uses sensor data sampled with the PIC micro-controller. The attitude is returned to the PIC micro-controller for generating control signals to the coils

Figure 5.1 provides a general view of the electronics used for the ADCS and includes the coils and coil drivers for the attitude control. This text will only focus on the electronics for attitude determination.

5.2 Sun sensors

Six cosine sun sensors attached on each side of the satellite are used for detecting the direction to the Sun. For this purpose silicon photodiodes are used as sun detectors, to generate a current proportional to

incident light. According to (Centrovision, 2002), the equivalent circuit diagram of a photodiode can be seen in figure 5.2.
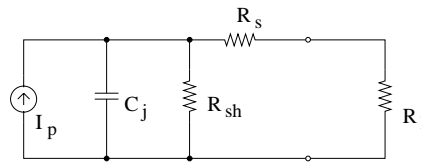

Figure 5.2: Equivalent circuit for silicon photodiode with a load R_l

I_p represents the photo-current proportional to the incident light. R_s is the series resistance of the photodiode and R_{sh} is the resistance of the diode junction. C_j is the junction capacitance of the photodiode.

Operating the photodiodes in photo voltaic mode with large load resistance will result in a nonlinear output response, which is also very temperature dependent. Reverse-biasing the photodiodes will allow high speed and linear response of the photodiodes, but also increased leakage current resulting in increased shot noise. It is chosen to operate the photodiodes zero-biased, where constant load resistance of the interfacing circuit is significantly smaller than the shunt resistance in the photodiode. This will result in an output response linear to the incident light and the noise generated by the photodiodes is mainly Johnson noise due to almost complete elimination of leakage current through R_{sh} (Centrovision, 2002)(Silicon, 2002).

5.2.1 Solar radiation

The sun sensors measure solar flux outside the Earth's atmosphere. A plot of extraterrestrial solar radiation and solar radiation at sea level[1] is shown in figure 5.3. Data used for in figure is from (RREDC, 2002).
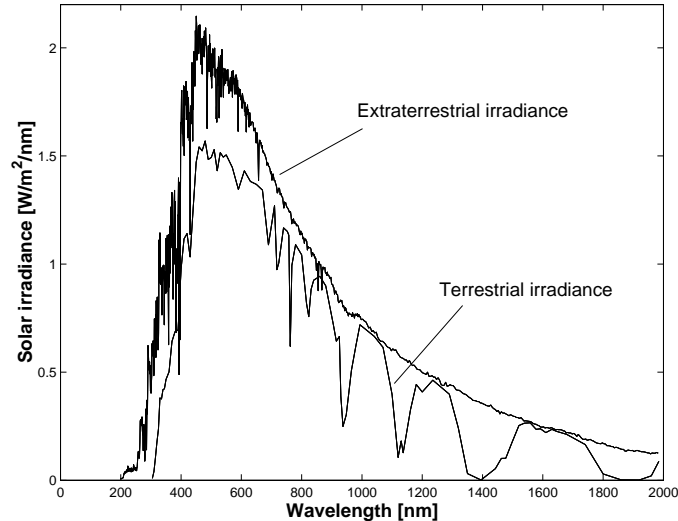

Figure 5.3: 1985 Extraterrestrial and terrestrial solar spectral irradiance curves are created in Matlab

The solar constant is mean solar energy flux at one astronomical unit [2]. In reality it is not a constant but varies by about 3.4% during each year because of the Earth's elliptical orbit about the Sun. In addition the radiation emitted from the Sun varies throughout an 11-years cycle. The solar energy flux outside

---

[1]The specified atmosphere for the terrestrial irradiance is the "1962 U.S. Standard Atmosphere" and an absolute air mass of 1.5
[2]One astronomical unit (AU) = average Earth to Sun distance

the Earth's atmosphere is equal to the area below the extraterrestrial solar spectral irradiation curve in figure 5.3. The default solar constant at 1 AU is 1371 W/m^2 and the maximum solar energy flux is 1428 W/m^2 during winter solstice (ECSS, 2002).

5.2.2 Sun detectors

For detecting solar radiation silicon planar photodiodes from Silonex are used (Silonex, 2001). These photodiodes have a sensitivity spectral range from 400 nm to 1100 nm and the maximum sensitivity wavelength is 930 nm. The typical short circuit current is specified to 170 μA at an energy input of 25 mW/cm^2 from a black body 2854° K light source. However, extraterrestrial solar irradiance better resembles radiation from a black body with a temperature of 5800° K (Ryer, 1998). In appendix B the maximum short circuit current at a total solar energy flux of 1367 W/m^2 is estimated to be 1.05 mA. Through tests, where the photodiodes were exposed to terrestrial daylight, the maximum output from the photodiodes are found to be 1.3 mA (see appendix J). Tests using light from lamps resembling sun light, indicated a maximum signal of approximately 0.52 mA. From these results the maximum short circuit current from the photodiodes is expected to be 1.3 mA.

The temperature dependency for the silicon planar diodes is measured to be 0.23%/$^\circ$C of the generated short circuit current (see appendix I). As there will be a large temperature difference between a sun sensor just entering sunlight from shadow and a sun sensor, which has been heated in sunlight for a long time, it is necessary to measure the temperatures of the sun sensors.

5.2.3 Sun detector interface

The zero-bias circuit used to interface the silicon photodiodes is shown in figure 5.4. The short circuit current from the photodiode is converted to a DC voltage between 0V and 5V.

$$R_l = 100\Omega$$
$$R_f = 28K\Omega$$
$$A = \frac{5V}{100\Omega \cdot 1.7mA}$$
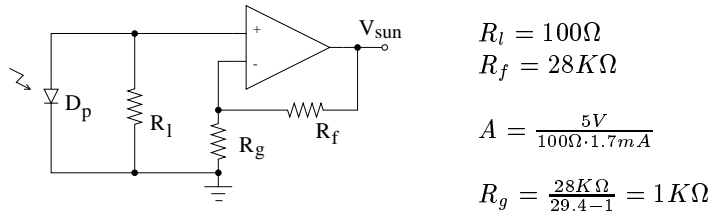$$R_g = \frac{28K\Omega}{29.4-1} = 1K\Omega$$

Figure 5.4: Zero-bias circuit for interfacing the photodiodes

Due to uncertainties in determining the maximum signal from the photodiodes, the amplification in the interface is dimensioned to a short circuit current in the range: 0 to 1.7 mA. This means, the interface is dimensioned for a maximum short circuit current approximately 23% higher than the tested maximum short circuit current. The output voltages from the 6 sun sensor interfaces are multiplexed and sampled with a 12 bit analog to digital converter.

If the maximum signal from the photodiodes is lower than expected in the size of 0.52 μA only 32% of the A/D converters range is used (32% of $2^{12} = 1305$). This will result in an angular resolution lower than one degree and much lower than the expected error of the sun sensors due to albedo:

$$\Delta S = \arctan\left(\frac{1}{1305}\right) = 0.044^\circ \tag{5.1}$$

5.2.4 Evaluation of sun sensor

The uncertainty with respect to the maximum output signal from the sun sensors when exposed to extraterrestrial sunlight, is compensated for by lowering amplification of the signal and accepting a lower resolution of sampled sun sensor data.

The error in one sun sensor, due to a temperature error of 5 °C, is found to:

$$I_{error} = TC_i \cdot \Delta T \cdot I_{sc,max}$$
$$= 0.0023 \cdot 3 \cdot 1.7mA$$
$$= 11.7\mu A$$

The angular error α_{error} is determined using equation 5.2 where the maximum possible error in one sun sensor is considered perpendicular to the signal of another sun sensor.

$$\alpha_{error} = \arctan\left(\frac{0.0117mA}{1.7mA}\right) = \pm 0.395° \qquad (5.2)$$

The cosine characteristic of the photodiodes is tested in appendix K, according to test specification TH2.1. The maximum error comparing to a perfect cosine curve was found to be 3.5 ° and the RMS error to be 1.84°. Considering the error due to cosine characteristic and temperature dependency, it is possible to fulfill requirement H2.1 of 4° using a temperature compensation with precision better than $\pm 3°$ C. This means that the error from misalignment, when mounting sun sensors on the engineering and flight model, should be less than 0.1°. If misalignment errors are higher than 0.1 °, it should still be tested if requirement H2.1 can be fulfilled. The angular error determined in equation 5.2, is an approximation of maximum error.

The noise from the sun sensors is specified in bit of the A/D-converter and is found for a maximum signal from sun sensors in appendix I. The noise has a peak value of 100 bit and is approximated to result in an error of 1.5°. The noise is white and will be reduced by sampling 16 values on the sun sensors and then finding the mean value. This is done on the PIC micro-controller. Note, that this has not been implemented and tested for the prototype, but is expected to reduce noise by a factor 16.

5.3 Temperature sensors

Sensors are implemented for measuring the temperatures of the sun sensors in order to compensate for the temperature dependencies of the silicon photodiodes. The temperatures will have great influence on the signals from the sun sensors, when a sun sensor comes from the shadow and into the sunlight.

5.3.1 Temperature interval

The expected temperatures for the sun sensors will range from -70 °C to +90°C. The temperature interval to be measured is limited to -50°C to 85°C as precision is limited at low temperatures because of the non-linear characteristic of the thermistor (see section 5.3.2). Because the Sun will heat the sun sensors towards the Sun, it is accuracy in the positive temperatures which are of importance for the temperature corrections of sun sensor readings.
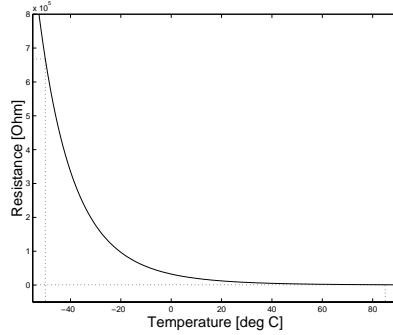
5.3.2 Thermistors

Six NTC thermistors are used for sensing the temperatures. NTC thermistors have a large negative temperature coefficient of resistance. The type of device chosen is a small epoxy coated BetaCurve interchangeable thermistors type 10k3A1A in series I from BetaTherm (BetaTherm, 2002). Interchageability means that each device is guaranteed to match the published resistance-temperature characteristics within the specified deviation ($\pm 0.1°$ C tolerance) over the temperature range $0°$ C to $70°$ C. The interchangeability removes the need for determining a temperature characteristic for the individual thermistors and hereby simplifies integration in the satellite structure.

The thermistor resistance-temperature characteristic is non-linear. A temperature value can be calculated from resistance using the Steinhart-Hart thermistor algorithm in equation 5.3 and the A, B and C values

specified for the thermistor. Equation 5.3 is verified with resistance values R for each temperature degree in the range from -50° C to 150° C specified from BetaTherm (BetaTherm, 2002).

$$T = \frac{1}{A + B\ln(R) + C(\ln(R))^3} - 273.15 \quad [^{\circ}C] \tag{5.3}$$

$A = 1.129241 \cdot 10^{-3}$
$B = 2.341077 \cdot 10^{-4}$
$C = 8.775468 \cdot 10^{-8}$

Table 5.1: Temperature-resistance characteristic and A, B and C values for the thermistor.

5.3.3 Thermistor interface

The thermistor and a constant resistor are used to make a temperature dependent voltage divider, in which voltage rises with temperature. To avoid self-heating of the thermistor a low voltage at 1.2V is applied to the voltage divider.
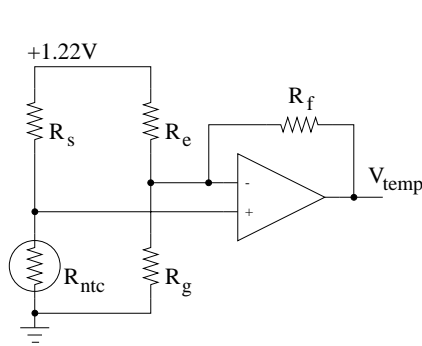
$V_{temp} = 0.02V$ to $4.98V$
$R_s = 25K\Omega \qquad R_f = 30K\Omega$
$R_{ntc} @ -50^{\circ}C = 1255\Omega$
$R_{ntc} @ +80^{\circ}C = 60.8K\Omega$

gain $= 7.5V$
offset $= 0.34V$

$R_e = \frac{1.2V \cdot 30K\Omega}{0.34V} = 150K\Omega$

$R_g = \frac{30K\Omega}{7.5 - 1 - 30K\Omega/150K\Omega} = 9K\Omega$

Figure 5.5: Interface for measuring temperatures at the sun sensors.

Output-voltages from the 6 amplifier circuits for the temperature measurements are multiplexed and then converted to a 12 bit digital value.

5.3.4 Evaluation of temperature-sensor

The output from the temperature sensors is non-linear and is converted to a temperature using the Steinhart-Hart equation 5.3.

The accuracy of the temperature sensors for the prototype is tested, according to TH2.3, as described in appendix M, and errors are found to be lower than $\pm 3^{\circ}$ C in the interval [-30 ... 85]°C, when calibrating with an offset of -1° C. This means that if misalignment errors are kept low when mounting sun sensors, as specified in section 5.2.4, requirement H2.3 is fulfilled.

Noise in the temperature measurements is in the level of one bit in the A/D-converter. Outliers have occurred in the measurements. The effect of outliers will be reduced by sampling each temperature sensor 16 times and finding the mean value. This is done on the PIC micro-controller. Note, that this has not been implemented and tested for the prototype, but is expected to reduce the size of outliers by a factor 16.

5.4 3-Axis magnetometer

A 3-axis magnetometer will be used to measure the direction of the Earth's magnetic field with respect to the satellite. Distortions of the magnetic field may occur from the satellite structure and other satellite components, and this must be taken into account.

5.4.1 Earth's magnetic field

The magnetic field intensity in an altitude of 700 km in a sun synchronous orbit is expected to be within 0.5 Gauss. This is verified with simulations of the Earth's magnetic field using an International Geomagnetic Reference Field (IGRF) model. The results of these simulations are shown in appendix N. The satellite structure or the subsystems may produce magnetic fields and affect the magnetic field measurements. This is known as magnetic distortion.

Magnetic distortions can be categorized as hard iron and soft iron effects. Hard iron distortion is caused by permanent magnets, magnetized iron or steel placed near the magnetometer, and will introduce a constant offset in the measured magnetic field. This offset can be determined using a calibration procedure when the satellite is assembled. Soft iron distortion arises from the interaction of the Earth's magnetic field and any magnetically soft material surrounding the magnetometer. The amount of distortion from the soft iron depends on the orientation of the magnetometer. It is also possible to perform a calibration for soft iron distortion, or it may be possible to reduce it by shielding its sources.

5.4.2 Magneto-Resistive (MR) sensors

For sensing the magnetic field in three axes Honeywells HMC1001 and HMC1002 components are used (HMC1001-2, 1999). HMC1001 contains one sensor used for measuring the Z-axis and HMC1002 contains two perpendicular sensors for measuring the X and Y -axis. The sensing material of the MR sensors in each axis is made of a resistive material[3] patterned to form a Wheatstone resistor bridge, as the one illustrated in figure 5.6. When a magnetic field is applied along the sensitive axis of the sensor, the resistance in the bridge will change, and so will the output voltage.
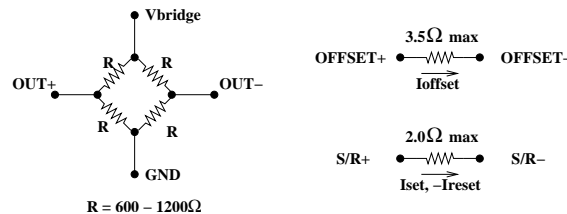

Figure 5.6: In each axis a Wheatstone bridge is used to measure the magnetic field.

The Honeywell MR-sensors have patented on-chip set/reset and offset straps. The offset strap can be used to eliminate the effects of hard iron distortion. The set/reset straps are used to reduce effects of temperature drift, non-linearity errors and loss of signal output due to the presence of high magnetic fields. If a magnetic field larger than 3 Gauss is applied to a sensitive axis in the HMC1001 and HMC1002 sensors, the polarity of the permalloy film may be upset or flipped, and result in a change of the sensor characteristics. Sensor characteristics may be restored by applying a strong magnetic field along the sensitive axis, using the

---

[3]The sensing material of the MR-sensors is made of permalloy film deposited on a silicon wafer.

set/reset straps. When applying a +5V bridge voltage V_{bridge} and using 3A S/R pulses the sensors have a typical sensitivity of 16 mV/Gauss.
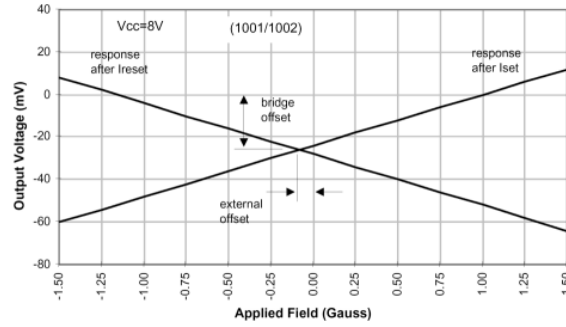

Figure 5.7: Output voltage after set and reset pulse when applying magnetic field

When a SET current pulse is driven from the SR+ pin in the set/reset strap the output response is the curve with positive slope in figure 5.7 (HMC1001-2, 1999). When a RESET current pulse is driven from the SR-pin, the output response is the curve with negative slope. The two output responses are mirrored about the origin, except for a bridge offset and an external offset. The bridge offset is due to resistor mismatch in the wheatstone bridges from manufacturing. The external offset may be due to nearby ferrous objects or magnetic fields interfering with the field to be measured.

The magnetic field is measured by first driving a SET pulse through a sensor and then read the sensor output V_{SET} when it has settled. Then a RESET pulse is driven through a sensor and the sensor output V_{RESET} is read. This technique is called "set/reset switching" and the applied magnetic field can be found using equation 5.4.

$$V_{applied} = \frac{V_{SET} - V_{RESET}}{2} \tag{5.4}$$

Bridge offsets, temperature offsets and offsets from the interface electronics are neglected when using the "set/reset switching" technique. External offset from hard iron distortion should be removed by performing a calibration when the satellite is assembled. Offset from soft iron distortion should be minimized by placing the magnetometer away from magnetically soft materials and shielding off sources of soft iron distortion.

5.4.3   Magnetometer interface

The signal from each MR-sensor bridge is amplified using instrumentation amplifiers. The total magnetic field is the result of the Earth's magnetic field, magnetic fields from soft iron and hard iron distortion. The actuators are not used while measuring the magnetic field. To avoid saturation of the sensors all magnetic field contributions have to be taken into account. The signal from the magnetic field of the Earth is ±0.5 Gauss. To account for the contribution from hard and soft iron distortion the field to measure is expanded to ±1 Gauss.

The constant bridge offset specified by Honeywell is for a sensor between -60 mV to 30 mV but it is typically -15 mV. This offset is reduced using the resistors R_{trim} in figure 5.8. The sensor signal to be amplified is ±1 Gauss equal to ±16 mV. It should be amplified to an output signal ranging from zero to 5V with a reference voltage of 2.5V corresponding to zero Gauss. The MR-sensors with interface are shown in figure 5.8. Operation and interface electronics for using the "set/reset switching-technique" with Honeywell MR-sensors is described in (HMC1001-2, 1999).

A set/reset circuit is used to create set and reset pulses of 4 A. The set/reset circuit is controlled using the PIC micro-controller. Each amplified output is converted with a 12 bit analog to digital converter on three different input ports in the PIC micro-controller.
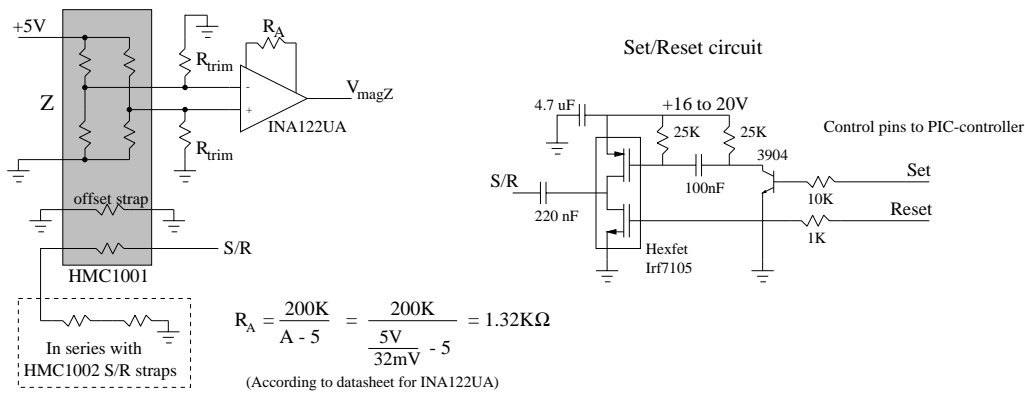
Figure 5.8: Interface to the Z-axis sensor and the set/reset circuit.

5.4.4 Evaluation of 3-axis magnetometer

The magnetometer circuitry is well documented in application notes and data sheets for the Honeywell MR-sensors (HMC1001-2, 1999). The magnetometer is tested according to test specification TH2.2, as described in appendix L. A calibration procedure was performed for the prototype magnetometer. Some wobble in the device used for rotating the magnetometer did show in sampled data. But calibrated data still produced almost perfect circles in the two planes, in which the magnetometer was rotated. For engineering and flight model a more robust construction is needed for rotating the magnetometer, when performing calibration procedures to compensate for magnetic distortion due to structure and other subsystems. Using data from (HMC1001-2, 1999) an error for the magnetometer can be estimated, according to (Caruso, 1999):

Error type	Specified for HMC1001/2	Field error	Angular error
Noise	29 nV	1.8 μGauss	<0.0002°
Linearity	0.5 %FS	5 mGauss	0.57°
Hysteresis	0.1 %FS	1 mGauss	0.11°
Repeatability	0.1 %FS	1 mGauss	0.11°
Total RSS error		5.2 mGauss	0.59°

Table 5.2: Error is found using maximum specified errors for HMC1002/2 and assuming full scale (FS) of signal is ± 0.5 Gauss. Using typical errors of HMC1001/2 the angular error will be 0.16 °.

5.5 PIC micro-controller

The controller for the ADCS chosen in cooperation with the group responsible for implementation of the attitude control algorithms. The PIC micro-controller selected for the ADCS is a PIC16C774 from Microchip. This micro-controller was chosen for fulfilling the requirements H3.1 to H3.4. The choice of using the I^{2}C bus together with necessary I/O-ports for sensors and actuators limited the selection of possible micro-controllers. The tasks related to attitude determination, which is the need for sampling sensors once a second and on request send them to the OBC, is in no way a problem with the PIC16C774. The implementation of attitude control on the PIC micro-controller is handled by (Frederiksen et al., 2002).

It was not set as a requirement, that the micro-controller should be approved for usage in space and this is also not the case for the PIC16C774. It is expected that the ROM inside the PIC micro-controller is resistant to single-event upset. It has been decided not to implement external RAM in the ADCS-subsystem, so only the internal RAM in the PIC16C774 will be available. The downside of this choice is that it wont be

possible to update algorithms running on the PIC micro-controller as there is only 256 bytes internal RAM available. The disadvantages avoided by not using external RAM are:

- External RAM would increase the time for implementing and testing the hardware.

- The external RAM modules would consume more power.

- The external RAM modules would take up more space and weight in the satellite.

- RAM is sensitive to single-event upsets.

ROM on the PIC micro-controller is expected not to be sensitive to single-event upsets. If the PIC stops executing, due to single-event upsets in internal RAM, this will be detected by the OBC and the PIC will be reset. The same type of micro-controller was chosen by (Lazar et al., 2002) for the PSU-subsystem.

The PIC16774 does not have enough analog ports for sampling all the sun sensors, temperature sensors and the magnetometer. For that reason the temperature sensors and the sun sensors are multiplexed using two 8 channel analog multiplexers. One multiplexer samples the six temperature sensors and a 2.5V DC reference voltage. The other samples the six sun sensors and a 1.22V DC reference voltage. The two reference voltages are used for magnetometer and thermistors, and are sampled in order to get some information on the system during initialization.

5.6 Software on PIC micro-controller

In this project software functions were developed in the C-programming language for the PIC micro-controller, to sample data from the attitude determination sensors. These functions have been used for verifying that the sensors work according to requirements. After having verified that the sensors work, it was decided that (Frederiksen et al., 2002) should be responsible for designing and implementing software on the PIC micro-controller. Software developed for the PIC micro-controller consists of algorithms for attitude control and the developed functions for sampling sensor data. Accordingly it was decided, that this group developing the attitude determination, would be responsible for designing and implementing software on the OBC. This includes making the interface to the DHCS subsystem and to the attitude control implemented in the PIC micro-controller.

Here is given a short description of software implemented on the PIC micro-controller for sampling sensors.

5.6.1 Sampling of sun and temperature sensors

Sampling of sun sensors and temperature sensors is implemented in one function. This is because the PIC micro-controller uses common digital output ports for selecting channels on the multiplexers. This results in the following pseudo code for sampling 6 sun sensors and 6 temperature sensors.

```
enable multiplexers
enable A/D-converters
for (x= 1 to 6)
  channel = x
  sample sun-sensor(x)
  sample temperature-sensor(x)
end
disable A/D-converters
disable multiplexers
```

In order to reduce noise in data from sun sensors and outliers in data from temperature sensors, the sun sensors and temperature sensors will be sampled 16 times, and the mean value will be found.

5.6.2 Sampling 3-axis magnetometer

The timing is important when generating SET/RESET pulses for the magnetometer and sampling the sensor outputs. After a Set or Reset pulse is generated, it is necessary to wait for the pulse to end and the slew rates of the instrumentation amplifiers have to be taken into account. The following pseudo code with delays is used in the tests of the prototype.

```
enable A/D-converters

Reset_signal low
delay 10us                     // Important delay to save HEXFET
Set_signal high                // Generates Set pulse
delay 30us
sample SetX
sample SetY
sample SetZ
delay 500us                    // Wait for capacitors to recharge
Reset_signal high
delay 10us                     // Important delay to save HEXFET
Set_signal low                 // Generates Reset pulse
delay 30us
sample ResetX
sample ResetY
sample ResetZ

disable A/D-converters
```

NOTE! It is important that the RESET and SET pulses of the magnetometer, are never high at the same time. This is to make sure that one HEXFET in the set-reset circuit is off before the other one turns on.

5.6.3 I^2C interface

The I^2C bus has been chosen for communication between subsystems. Housekeeping and error messages are send from subsystems to the OBC and the OBC can send commands and relevant info to the subsystems.

The data from the sensors will be send from the ADCS micro-controller to the OBC for processing. Accordingly the output from the ADS on the OBC will be send to the attitude control to perform the necessary changes of the satellites attitude.

Further information about the protocol used for I^2C communication is described in appendix G.

5.7 Sensor specifications

After hardware validation of prototype print, engineering model and flight model, the following sensor specifications for each of the three hardware versions are specified. The specifications for the sensors output signals are defined at the I^2C bus. This means that the algorithms implemented in the PIC micro-controller influence the specifications.

5.7.1 Sensor specifications for Prototype

Hardware validation tests for the sensors in the prototype print can be found in appendices L, K and M. The PIC micro-controller is a unit providing sensor information from the three sensor types. Output signals from sensors are specified as values read using the I^2C bus. The sensor readings will be part of housekeeping data being sent from the PIC micro-controller.

	Min	Typical	Max	Units	Note
Sun sensors					
Output Range	0		4096	bit	2 bytes of data
Input Range	0		1428	W/m^2	Expected maximum input
Short circuit current		1.3		mA @ 1428 W/m^2	Determined from test
Resolution		349		mW/m^2	
Temperature coeff.		0.233		%/$^\circ$C	Determined from test
Cosine error			3.5	$^\circ$C	From test (not incl misalignment)
Noise peak-peak			± 6.5	bit	From test with approx. max output
Temperature sensors					
Output Range	0		256	bit	1 byte of data
Input Range	-50		85	$^\circ$C	
Resolution		0.033		$^\circ$C	
Error		± 1	± 3	$^\circ$C	Determined from test
3-axis magnetometer					
Output Range	0		4096	bit	2 bytes of data
Input Range	-1		1	Gauss	
Resolution		488		μGauss	
Angular error		0.16	0.59	deg	Determined from specifications
Field error			5.2	mGauss	Determined from specifications
Noise		1.8		μGauss	Determined from specifications

Table 5.3: Specifications for sensors for attitude determination in prototype

5.8   Status on Hardware

At the current state of the hardware design the following goals have been achieved regarding the development of sun sensors and the on board magnetometer.

5.8.1   Development State of Circuit Print

The circuit print of the ADCS subsystem was developed as prototype print to test and optimize the general functionality of the hardware. It was used for sampling of sensor data from the magnetometer, sun sensors and temperature sensors. After minor modifications and optimizations of this hardware part it was redesigned into a smaller version and manufactured for the engineering model. On the CDROM the circuit print for the ADCS PCB can be found.

The prototype version of the circuit print itself was tested regarding functionality and performance but not regarding environmental effects, such as temperature changes, radiation or vibration and shock. These tests will be performed on the assembled engineering model of the satellite structure including the engineering model of the ADCS print.

However, the functionality tests performed on the ADCS prototype print showed to be a success and sampling of data from the different sensors was possible. Furthermore communication was tested between the ADCS subsystem and the OBC. However, these tests did not include sampling of sensor data.

5.8.2   Development State of Sun Sensors

The detectors of the sun sensors were chosen and their interface circuitry was designed. The interface to the micro-controller was developed and the sampling of data from the sun sensors showed to be possible.

Several tests were performed on the sun detectors to ensure they are suitable for their task in space. These included various test setups:

- Tests were performed during the development of the sun sensors and the circuitry connected to them. As the detectors are run in short circuit mode, the parameters of this circuit had to be determined to ensure the detectors would be able to measure sun light. This testing is described in appendix J.

- Several Light intensity tests were performed. These included a test of the angle sensitivity (cosine characteristics) of the sun sensors and tests with different light sources as described in appendix K and B.

- Temperature tests were performed on the detectors in relation to a constant light source to determine the temperature sensitivities of the sensors. This test is described in appendix I and was used to determine the temperature coefficient of the detectors.

- A radiation test was performed on the detectors at the Aalborg Hospital North using the radiation equipment used for cancer treatment and other purposes. Here the detectors were exposed to a total radiation dose of 48.000 Rad by electrons at an energy level of 20 MeV. This was an attempt to test sun sensors to the similar amount of radiation in a LEO orbit during a time of a half year. The detectors were tested for a change in their performance after the exposure, which showed not to be of any size measurable.

The Integration of Temperature Sensors

The temperature sensors were already chosen in a space approved version and hereby the time and effort of testing these components was saved. The temperature sensors were used in a test setup described in appendix I and in other similar performance tests they showed to work as expected. Validation tests of the temperature sensors have also been described in appendix M.

The Sun Sensor Sockets

To assembly the temperature sensors and sun detectors in one unit and to simplify the mounting of the sensors on the sides of the satellite sockets were developed. These were designed in cooperation with (Overgaard and Hedegaard, 2002) and are described in chapter 6.

Accordingly several tests shall be performed on these assembled sensor units to test the functionality of the sensors when exposed to different environmental effects, such as vacuum, temperature changes and vibration and shock.

5.8.3   Development State of Magnetometer

The magnetometer was assembled on the prototype print and its functionality was tested here by rotating it around given axes and measuring the change in the magnetic field. This test has been described in appendix L.

Further tests of the magnetometer will follow on the engineering print in the satellite structure. A calibration of the magnetometer data will be necessary to compensate for the disturbing effects caused by the satellite structure and the other subsystems on-board the satellite. For this calibration several tests will be necessary. Further eventual misalignments of the magnetometer inside the satellite structure will be measured to enable a compensation of this error. A final accuracy of the magnetometer can not be determined before it is implemented in the satellite structure.

5.8.4   Further Development and Assembly of the complete ADS

As most of the elements of the ADS have been developed and tested separately, a combined test of the functionality of all sensors and components inside the satellite structure of the engineering model will be

necessary. This will include a test of the data sampling from the different sensors as well as the conversion of the data to values to be used in the ADS software.

Further tests will be performed on the entire engineering model of the AAU CubeSat including temperature tests, vacuum tests, radiation exposure and vibration and shock treatment. Especially the radiation tests will be of interest in this case as they may introduce bit flips or other effects in the software of the satellite. No final decisions have been made regarding environmental tests.

5.9 Summary

In this chapter the design of the ADS hardware is described. It is integrated in a PCB with the ACS hardware. The designs of sun sensors, temperature sensors and magnetometer are described. All sensor types were tested and evaluated to be functional. Software has been developed for the PIC micro-controller to sample sensors. The remaining software on the PIC-controller is developed by (Frederiksen et al., 2002). In table 5.3 specifications are given for the tested prototype.

chapter 6

Mechanical Design

This chapter will give a general view of the mechanical properties of the CubeSat satellite and the attitude determination system. It will give an introduction to the satellite structure including the positions of subsystems, the mass budget and the mass distributions. It will be followed by a description of the ADS print and finally describe the sensors regarding their positions and orientations in the different coordinate frames.
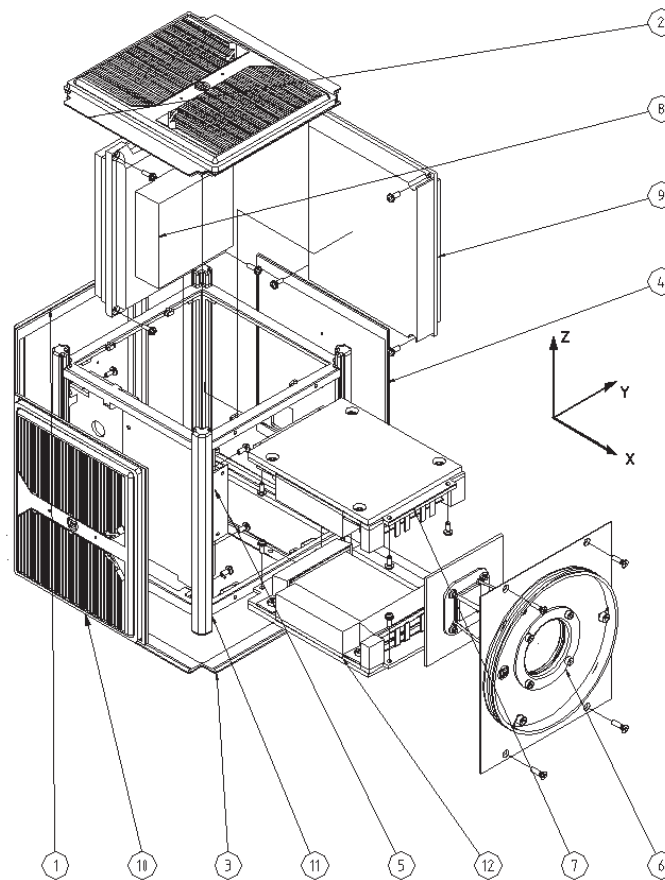
6.1 The Satellite Structure

Figure 6.1: The assembly of subsystems in the satellite. Parts numbered 1 to 12 are described on page 47

The satellite structure of the AAU CubeSat consists of the following subsystems and elements, which are placed inside the aluminum frame (11) of the satellite as shown on figure 6.1.

The On-board Computer: The On-board Computer (OBC) (8) is placed at the end of the on-board camera (6) and positioned on the opposite side from the communication antenna.

The Camera Payload: The camera payload (6) is placed in the middle of the satellite, while all other subsystems are placed directly behind the satellite sides. The lens of the on-board camera is the largest part of this subsystem, as it runs from the satellite surface inside the antenna ring and merges into the camera chip, which is placed on top of the OBC-subsystem (8). Compared with many other subsystems the camera payload is one of the heaviest subsystems on-board the AAU CubeSat.

The Power Supply: The power supply subsystem (PSU) contains ten solar panels mounted on five of the satellites surfaces (1, 2, 3, 4 and 10), the batteries (7 and 12), which are mounted on each side of the camera, and the PSU (9). The circuit board of the PSU is placed on the opposite side of the communication unit (5) as shown on figure 6.1.

The Communication Unit: The communication unit (5) is, apart from the camera, the only major subsystem which has not been designed but was purchased instead. It is placed on the opposite side from the PSU subsystem and includes the communication antenna, which is placed on the satellite side around the camera lens (6).

The ADCS System: The ADCS subsystem consists of a circuit board including magnetometer, which is assembled with one of the battery packs on one board (7), three electro-magnetic coils for attitude control, which are placed on the satellite sides (1, 2 and 10), and the sun sensors and thermistors, which are mounted between solar panels on the five satellite sides (1, 2, 3, 4 and 10) and between the antenna ring and mounting for lens (6).

The Kill Switch: On the second board besides the battery pack (12) another circuit print is mounted, which is used for the electronics that will interface the kill switch. This kill switch print is a part of the PSU subsystem and will turn the power supply of the satellite on when the kill switch is released during deployment of the CubeSat from the P-Pod.

6.2 The Mass Budget and Distribution

The mass budget of the CubeSat satellite is not allowed to exceed 1kg and the weight of the satellite is calculated to be 0.920kg before beginning the assembly of the engineering model.

During the design of the mechanical structure of the satellite the mass distribution and moments of inertia have been calculated, also including even small elements inside the satellite, such as wires, screws and glue.

The moments of inertia of the satellite have been defined as principal moments of inertia around the principal axes. These principal axes are defined in the SCB frame, which is located in the satellites center of mass, and are representing the SCP frame. The principal axes defined in the SCB frame can be seen in the equations 6.1. These are used for simulations described in this report. Note that equation 6.1 to 6.3 are determined before the engineering model has been assembled and they may be updated later.

$$x_p = \begin{bmatrix} 0.979mm \\ -0.203mm \\ 0.031mm \end{bmatrix} \qquad y_p = \begin{bmatrix} 0.204mm \\ 0.977mm \\ -0.058mm \end{bmatrix} \qquad z_p = \begin{bmatrix} -0.018mm \\ -0.063mm \\ 0.998mm \end{bmatrix} \qquad (6.1)$$

The moments of inertia around these axes are given as a diagonal principal inertia matrix shown in equation 6.2.

$$J_p = \begin{bmatrix} i_p & 0 & 0 \\ 0 & j_p & 0 \\ 0 & 0 & k_p \end{bmatrix} = \begin{bmatrix} 1983221.309gmm^2 & 0 & 0 \\ 0 & 2100895.792gmm^2 & 0 \\ 0 & 0 & 1882314.372gmm^2 \end{bmatrix} \qquad (6.2)$$

Based on the coordinates a rotational matrix can be set up to rotate the vectors from the SCB frame to the SCP frame. By using the XYZ-axes of the SCB frame and the coordinates of the principal axis in the same frame and applying these values to Wahba's Problem (SVD method described in chapter 10) a rotational matrix A_{SCB}^{SCP} can be determined. This matrix is shown in equation 6.3.

$$A_{SCB}^{SCP} = \begin{bmatrix} 0.9790 & 0.2031 & -0.0183 \\ -0.2031 & 0.9791 & 0.0001 \\ 0.0179 & 0.0037 & 0.9998 \end{bmatrix} \tag{6.3}$$

6.3 Integration of the ADCS Subsystem

The electronics of the attitude determination and control subsystem is integrated on the same print board. This is located next to one of the battery packs of the PSU, as described in figure 6.1.

The ADCS subsystem includes 4 components, which are described here.

- Electronics

- Magnetorquers

- The Magnetometer

- The Sun Sensors

6.3.1 The ADCS Print Board

The ADCS print has been designed as shown in figure 6.2. The print board shown in this figure measures 88.5mm by 62mm (1). The allowable space on the surface of this print, which is left for components and wires, is shown in white and consists of the free space, which is pointing towards the inside of the satellite (3), and the free space, which is lying between the surface of the print and the side panel of the satellite (2). The completed engineering model print has been designed to fulfill these space requirements.
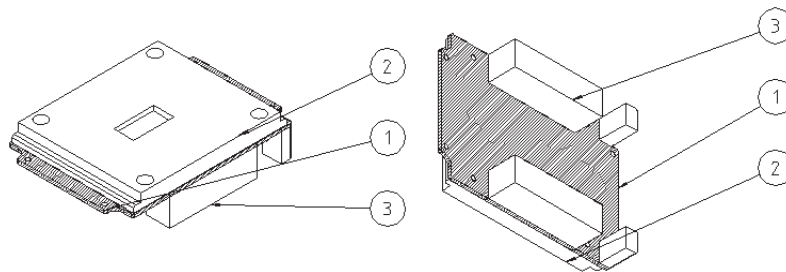

Figure 6.2: The Layout of the ADCS print

6.3.2 The Magnetorquers

The three magnetorquers used as actuators in the satellite, are placed on three side-panels of the satellite and are surrounding the solar panels. As seen on figure 6.1, the magnetorquers are placed perpendicular on all three axes of the SCB frame on the three sides (1, 2 and 10) in figure 6.1.

Further information about the design and placement of the coils can be obtained in the report regarding the attitude control (Frederiksen et al., 2002).

48

6.3.3 Position and Orientation of the Magnetometer

The magnetometer used in the attitude determination consists of the two magneto-resistive sensors HMC1002 and HMC1001 from Honeywell, which are placed on the ADCS print, as shown if figure 6.3.
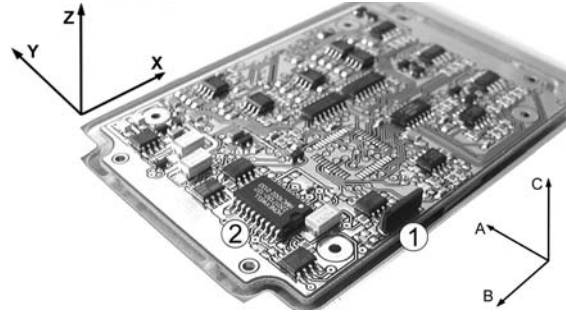

Figure 6.3: The placement of the sensors HMC1001 (1) and HMC1002 (2) on the ADCS print.

Both components are placed on the same side of the print board as the PIC micro-controller. The measurements of the HMC1001- and HMC1002-components are obtained in a magnetometer coordinate frame. The magnetometer frame is defined in figure 6.3 as A, B and C axes and a rotation A_{mag}^{scb} is needed to rotate magnetometer data into the SCB frame. Axes of the magnetometer frame should be parrallel to axes in the SCB frame. However, misalignments from mounting the magnetometer into the satellite, may introduce a small rotation. This rotation A_{real}^{mag} is included in the rotation matrix A_{mag}^{scb}, as specified in equation 6.4. Axes in the magnetometer frame correspond to axes in the SCB frame, by a 90°rotation in the x-y SCB frame:

$$A_{mag} = Y_{scb} \qquad B_{mag} = -X_{scb} \qquad C_{mag} = Z_{scb}$$

$$B^{scb} = A_{mag}^{scb} B^{mag} = \begin{bmatrix} 0 & 1 & 0 \\ -1 & 0 & 0 \\ 0 & 0 & 1 \end{bmatrix} A_{real}^{mag} B^{mag} \tag{6.4}$$

Misalignment of the Magnetometer

As the magnetometer sensors are mounted on the ADCS print board, which again is mounted inside the satellite frame, there are two possibilities for misaligning the magnetometer in the SCB frame.

The first possible misalignment may occur between the satellite frame and the print board. However, as these components have been designed and manufactured with high accuracy and the print board is of relatively big size compared with the magnetometer components, this misalignment will be smaller than a possible misalignment between the magnetometer sensors and the print board.

As the sensor components are relatively small and soldered onto the board, it may proof to be difficult to avoid minor misalignments. These misalignments will be detected and determined during the calibration of the magnetometer. Since the magnetometer uses two sensor components, it is a possibility that the component measuring in the z-axis (HMC1001) is not mounted completely perpendicular to the x-y plane. This can be corrected by gently bending it into place.

The procedure for removing misalignment between magnetometer sensors, should be the following. The magnetometer does not need to be integrated into the satellite structure for this procedure:

1. Rotate the magnetometer in x-y, x-z and y-z plane while sampling data

2. Data should show a 90°phase shift between axis in the rotated plane (guaranteed for x-y plane).

3. If phase shift is not 90°for x-z or x-y plane, then adjust z-axis sensor and redo from 1

Now the sensors should be perpendicular to one and another. Glue shall be applied to the component HMC1001, in order to secure that it stays in place. Now misalignment of the sensors with respect to print board and the satellite structure, should be determined from the calibration procedure described in test specification TH2.2.

With the misalignment of the magnetometer determined, the rotation A^{scb}_{mag} shall reduce misalignment errors of the magnetometer to 0.1°.

6.3.4   The Position and Orientation of the Sun Sensors

The six sun sensors and the thermistors are mounted in sockets and placed on the six side panels of the satellite. The sun sensors including thermistors are named as specified in figure 6.4.
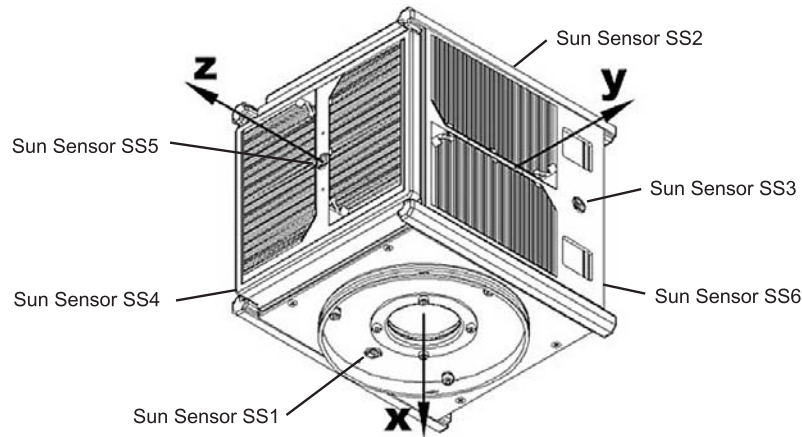

Figure 6.4: The positions of the Sun Sensors on the satellite and in the SCB frame.

Three different types of sockets are made for the sun sensors. In table 6.1 it is specified what types of sensors are used for each of the six sun sensors with thermistors.

Socket type	Sun sensors			Thermistors		
type A	SS2	SS3	SS4	T2	T3	T4
type B	SS5	SS6		T5	T6	
type C	SS1			T1		

Table 6.1: types of sockets used for each sun sensor and thermistor.

Sockets for the Sun Sensors

To place the sun sensors and thermistors close to each other and on the side panels of the satellite, sockets have been designed and fabricated. This was done in cooperation with the group responsible for the mechanical design of the satellite (Overgaard and Hedegaard, 2002).

The material used for manufacturing these sockets is Aluminum 7075 T6, which is a light and high tensile alloy and used in the aerospace industry. The sockets have had a surface treatment, as there has been performed a phosphor acid anodization to prevent oxidation and to increase the performance of the glue used to mount the sockets onto the side panels of the satellite.

The size of the sockets is 10x5 mm with a height of 2.75 or 10mm as shown on figure 6.5. There are three different types of sockets.
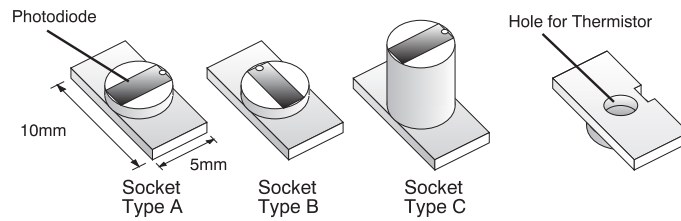

Figure 6.5: The Sun Sensors mounted in sockets.

Two of these are flat with the photodiode mounted in two possible directions. This is due to the solder blob which is sitting on the surface on the end of every photodiode. When the incoming sun light would come from the soldered side of the photodiode and lie in a low angle, this solder blob would create a shadow on the photodiode introducing an error to the measurements. However, this error will only occur if the photodiode points towards the light source with its solder blob. all sun sensor sockets have been designed to point the soldering blob towards the on-board camera, as this side of the satellite never would point towards the sun on purpose. Hereby none of these errors will be introduced under the normal performance of the satellite.

The third type of sun sensor sockets is higher than the other standard types, as shown on figure 6.5. This will be mounted on the camera side of the satellite and inside the antenna ring (Sun Sensor SS1). It is designed to be high enough to avoid a shading of the sun sensor by the antenna ring.

Five sets of 6 sun sensor sockets were manufactured for the assembly of the sensors for the engineering and flight model and several test purposes.

The sockets will be assembled with the sun detectors and temperature sensors using a space approved epoxy glue. Accordingly these sensor units will have to be set up in a vacuum chamber before the glue hardens. This is necessary due to draw the remaining air out of the epoxy in order to prevent a later outgassing or damage of these components.

The sun sensor sockets will be mounted onto the satellite sides using the same epoxy glue as used for the assembly of the sensors. The sun sensor sockets are placed through holes from the inside of the side panels, as shown in figure 6.6. This method for mounting the sun sensors was chosen because it secures that the sockets are aligned smooth with the surface of the satellite sides.
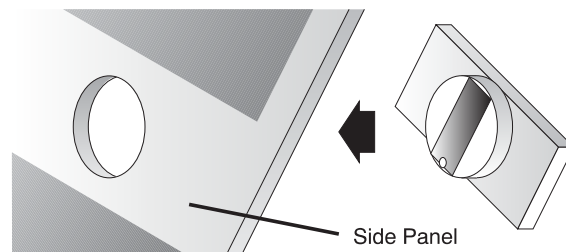

Figure 6.6: Mounting of a sun sensor through hole in satellite side.

Misalignment of the Sun Sensors

The alignment of the sun sensors is a critical part of the design as misalignment may easily occur. There are two possibilities of misalignment errors. The first possibility is a misalignment of the mounting of the

sun sensor sockets onto the satellites side panels. However, this misalignment should be very small with the method developed for mounting the sockets.

A misalignment during the mounting onto the side-panels has not been assumed to be as critical as the second cause for misalignment, which is the assembly of the sun sensors. As the photodiodes only measure 3.4 by 1.3 mm would it be a difficult task to ensure they are mounted correctly onto the sockets. Especially as their back-sides are uneven due to soldering tin and can not be used to align them with the sockets. The surface of the photodiodes will be the only reference to align them with the surface of the sockets. If this solution is chosen, care should be taken not to damage the sensing surface of the sensors.

Because of the assumed difficulties with mounting photodiodes into the sockets, extra sockets have been fabricated. A total of six sun sensors are needed in the flight model and another six for the engineering model. Thirty sockets have been fabricated and the same number of photodiodes have been purchased. Assembling a total of thirty sun sensors, each sensor will be graded after how well the photodiode is aligned in the socket. The set of six sun sensors with the highest grade will be used for the flight model. The second best graded set will be used for the engineering model. Each set shall consist of the necessary types of sockets, developed for the different sides on the satellite.

Misalignment errors of sun sensors should be low enough to secure requirement H2.1. Considering the deviation of photodiodes from a perfect cosine characteristic, as described in section 5.2, the misalignment error of the photodiodes shall be no more than $0.1\,°$. This will result in a maximum error for each sun sensor which can fulfill requirement H2.1.

Shadow effects on sun sensors

Shading effects were taken into account when designing the sun sensors. The sensors have a $180\,°$ field of view, which means that any objects sticking out from the satellite surface may cause a shadow to fall on sun sensors. The soldering blob needed on the photodiodes for attaching a wire, may cause shadows if the satellite points the camera towards the Sun. In both camera and power save mode, this should not be a problem. The photodiode for sun sensor SS1 is mounted on the camera side and has been elevated using a higher socket. This secures that the antenna ring does not cast a shadow on this sensor. Shading may still occur on the sun sensors caused by the two long antennas of the communication unit. However, this is considered to be a problem which very seldom occurs, because the antennas fill very little in each sun sensors field of view.

Proper handling of sun sensor components

When assembling the sun sensors and when mounting them onto the satellite, the following cautions should be taken, to secure high quality of the sensors.

- Handling of photodiodes, thermistors and sockets should take place in a clean environment.

- Gloves should be used when handling components. It is especially important to avoid fingerprints on photodiodes and sockets. The sensitive surface of the photodiodes must not be damaged. The surface treatment of the sockets is also very fragile. Fingerprints and dirt can reduce the effectiveness of glue.

- The sockets should not be handled with metal tweezers or the like, because they can scratch and destroy the surface treatment. For the same reason the sockets should not be fastened in a vice or the like, without using a soft intermediate layer.

- Care should be taken to avoid glue on the sensing surface of the sun sensors.

6.4 Summary

A short description of how the subsystems shall be integrated into the satellite, was presented in section 6.1. The principal moments of inertia are specified in equation 6.1 and the matrix for rotating a vector from the SCB frame into the SCP frame, is given in equation 6.2.

Integration of the attitude determination into the satellite, was described in section 6.3. A rotation matrix A_{mag}^{scb} was specified for rotating magnetometer data into the SCB frame. This rotation includes misalignment errors. Misalignment may occur between the two magnetometer sensors HMC1001 and HMC1002, and have to be corrected by bending HMC1001 into place. The misalignment of the magnetometer with respect to the satellite structure, has to be determined and included in A_{mag}^{scb}. The misalignment error after calibration shall not exceed 0.1° for the magnetometer.

An identity number was specified for each sun sensor with thermistor in section 6.3.4. The position and type of each sun sensor with thermistor was specified. The sun sensors are mounted with glue through holes in the side panels of the satellite. It is important that soldering blobs on sun sensors are positioned towards the camera. The misalignment errors for the sun sensors shall not exceed 0.1°. Rules are specified for *proper handling of sun sensor components* and these shall be followed when assembling sun sensors and integrating in the engineering and flight model.

<p style="text-align: right;">chapter 7</p>

Orbit Models

The following chapter will contain information about the ephemeris, the orbital mechanics, models and properties. The chapter will give an overview over the different orbital terms used to describe an orbital motion. Accordingly the SGP4 orbit model used in a Simulink simulation of the satellite will be described, as well as a simple Kepler model and a sun model, which will be used on-board the satellite for determining the satellites position in its orbit. Finally a model for calculating a direction to the Sun will be described.

7.1   Orbital Mechanics

To calculate orbital motions and positions in three dimensional space it requires a number of orbital parameters. These are given beforehand, calculated or given by observations, as in case of the Two Line Elements (TLE), which will be described in the following sections. Further it requires the current time and the time at which an orbiting object was in a specific position. This time is also measured and defined in a certain format called Julian Date.

7.1.1   Two Line Elements

An option to determine a satellites motion after its launch is to use Two Line Elements (TLE), also called NORAD lines.

These informations are based on, that every object, which orbits the earth and is bigger than a tennis ball, is monitored and tracked by Radar by NORAD (North American Aerospace Defense Command) ((CelesTrak, 2002)). The format has been used since the beginning of space flight and is still in use by NORAD and NASA. The origin of the Two Line Elements is unknown but some reports refer to it as T-card format ((Amsat, 2002)).

The Two Line Elements consists of two 69 character strings of data in a format as shown in figure 7.1.
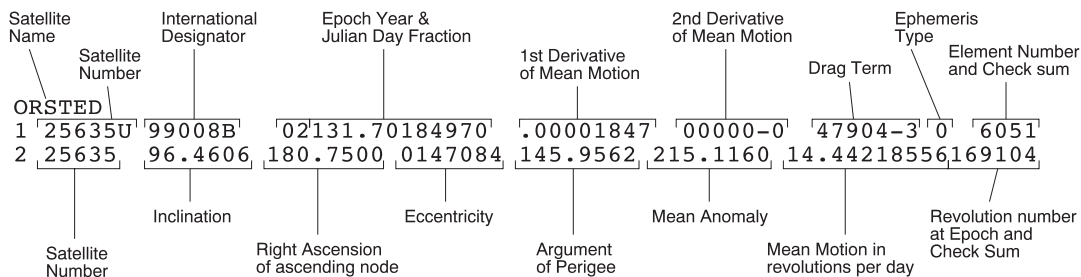

Figure 7.1: A Two Line Element Set (TLE) for the Ørsted Satellite

The parameters given by the Two Line Elements, which concern the orbital motion of the satellite, are the following:

Time of Epoch: Time of epoch represents the time when the orbital parameters given in the TLE were obtained. In the TLE format it is given as epoch year (The first two numbers) and the Julian day and fraction of the same year.

1.st Derivative of Mean Motion: This term represents the change in the mean motion of the satellite. The first derivative of the mean motion given in the TLE is the half value of the change of the mean motion in revolutions per day squared and is caused by atmospheric drag pulling the satellite into a lower orbit and hereby accelerating it up.

2.nd Derivative of Mean Motion: This term represents the second derivative of mean motion. However, usually is this term not used and set to zero in the TLE.

Drag Term: The drag term or radiation pressure coefficient consists of a coefficient describing the effect of drag on the satellite. The Drag Term is based on the satellites surface and mass and it is used in the SGP4 orbit model.

Inclination: The angle between the Earth's equatorial plane and the orbital plane is called inclination and measured relative to the earths orbital plane as shown in figure 7.2. If the inclination lies between $0°$ and $90°$, it is called a prograde orbit, as the satellite is moving in an eastern direction. An Inclination between $90°$ and $180°$ is called retrograde, as the satellite moves in an western direction.
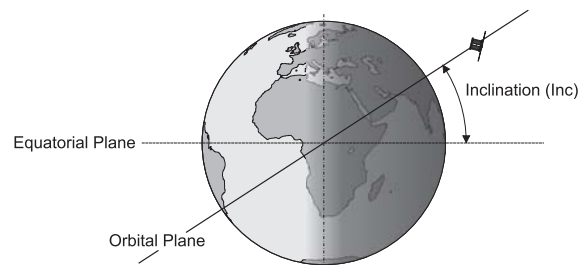

Figure 7.2: The Inclination of the satellite orbit is the angle between the orbital plane and the equatorial plane.

Right Ascension of the Ascending Node: The angle between the Vernal Equinox (The X-axis of the ECI frame) and the line, which is given by the intersection between the orbital plane and the equatorial plane as shown in figure 7.3. The ascending node is a line given by the two points where a satellite passes through the Earth's equatorial plane while moving up over the equatorial plane and going down below it again.

Eccentricity: The eccentricity defines how elliptical or circular an orbit is. An eccentricity of 0 is equal to a circular orbit, while an elliptic orbit has an eccentricity between 0 and 1, a parabolic orbit approximately 1 and a hyperbolic orbit above 1.

Argument of Perigee: The argument of perigee is the angle between the ascending node and perigee as shown in figure 7.3. The major axis, which is equal to the largest diameter of an elliptic orbit and which passes through the earths center. The Perigee is in this case the line parallel to the major axis which is going from center of the earth to the closest end of the ellipse.

Mean Anomaly: The Mean Anomaly represents the angle describing the satellites position in its orbital path. The angle is given measured from perigee, where it is zero, and referenced to a circular orbit with radius equal to the orbits semi major axis. The mean anomaly in the TLE is the orbital position of the satellite at epoch time.

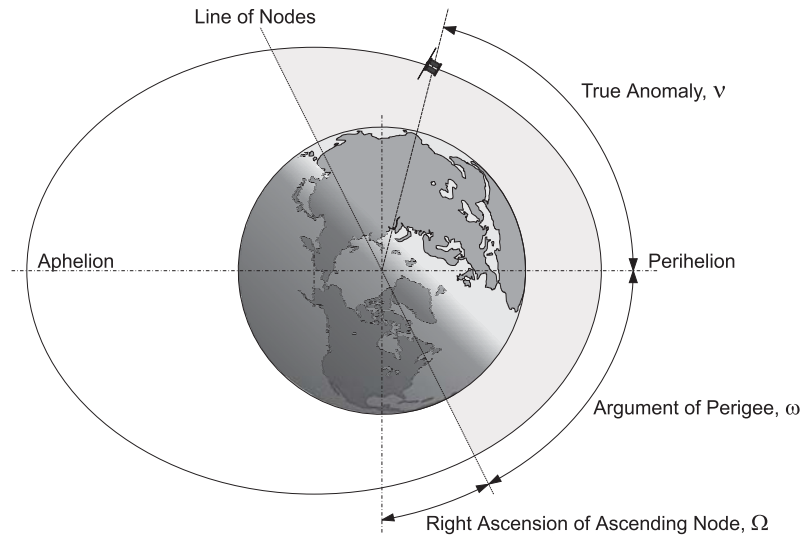**Mean Motion:** The Mean Motion consists of the number of revolutions, which the satellite completes per day.

Figure 7.3: The parameters characterizing the orbit

Revolution Number at Epoch The last parameter in the TLE gives the number of the orbit at the epoch time, when the TLE was taken.

7.1.2 Other Parameters

Two other important parameters used in orbital calculations are the Universal Gravitational Constant and Earth Equatorial Radius.

The Universal Gravitational Constant μ is a parameter describing a planets gravitational force which is acting on the satellite. In case of the Earth it is equal to $3.986005e^{14}\ m^3/s^2$.

The second parameter describes the earths mean radius at the equator $E_{EarthEq}$ and it is approximately equal to 6378.140 km.

7.1.3 Julian Date

A very common time format when dealing with astronomical calculations and satellite orbit propagations is the Julian Date. It is counted in days plus a fraction of the day, which begins at noon universal time. The Julian Date is counted in days since the 1.st of January 4713 BC at noon universal time.

The on-board algorithms of the AAU CubeSat will not use the entire Julian Date and instead use the Julian Date since noon UTC the 1.st of January 2000. This means there will be an offset of 2451545 days subtracted from the ordinary Julian Date format to use it on the on-board algorithms.

7.2 The Orbit Model

To determine the position and motion of a satellite in orbit based on the data from the Two Line Elements, mathematical orbit models are used. Two examples of orbit models are the SGP4 orbit model and the Kepler orbit model, which will be used on-board the satellite to calculate the position in the orbit for the purpose of determining the attitude of the satellite..

56

7.2.1 The SGP4 Orbit Model

The most used and most reliable orbit determination model is the SGP4 model. It was developed in 1970 for the use of near Earth satellites ((Felix R. Hoots, 1988)).

The higher accuracy of the SGP4 model compared with the accuracy of an ordinary Kepler orbit model relies on the use of informations, as for example the atmospheric drag acting on the satellite, the flatness of the earth and gravitational effects.

They use the informations contained in the Two Line Elements to determine a satellites current orbital position and motion. The data used to generate the Two Line Elements also is based on the use of a SGP4 model for Earth near satellites, and a SDP4 model for deep space satellites.

For the simulations of the attitude determination a SGP4 orbit model is used to create the reference position of the satellite.

7.2.2 The On-board Orbit Model

For determination of the orbital position an orbit model is used on board the satellite. A simple Kepler orbit model was developed instead of using the more complex and precise SGP4 orbit model.

The on-board orbit model uses the actual Julian Date since 2000 as input as well as the following parameters of the Two Line Elements; Time at Epoch, Inclination, Right Ascension of Ascending Node, Eccentricity, Argument of Perigee, Mean Anomaly and Mean Motion.

Mean Anomaly: The first step is to determine the current mean anomaly of the satellites orbital position. This is achieved by using the time since epoch T_{se}, which is the current time in Julian Date minus the Julian Date at Epoch, which is given in the TLE.

The current Mean Anomaly M_t is calculated in degrees using equation 7.1, which includes the mean anomaly at epoch M_{Epoch} and the mean motion n_{rev} from the TLE.

$$M_t = M_{Epoch} + 360 n_{rev} T_{se} \tag{7.1}$$

Semi Major Axis: The Semi Major Axis A_{km}, representing the largest radius of an eccentric orbit as shown in figure 7.4, is given by equation 7.2.

$$A_{km} = 331.25 e^{\frac{2}{3}log(\frac{1}{1440} MeanMotion_{Epoch})} \tag{7.2}$$

Argument of Perigee and Right Ascension of Ascending Node: The Argument of Perigee ω and the Right Ascension of the Ascending Node $RAAN$ are both wandering with a constant speed relative to the ECI frame. To compensate for this effect in the orbit model, the daily change is determined as $\dot{\omega}$ and $\dot{RAAN}$ in equation 7.3 and 7.4. The parameters used here are the orbital Inclination Inc, the orbital Eccentricity Ecc, the Semi Major Axis of the orbit A_{km} and the Earth's Equatorial Radius $E_{EarthEq}$.

$$\dot{\omega} = 4.98204 ((\frac{E_{EarthEq}}{A_{km}})^{3.5})(5\cos(Inc)^2 - 1)((1 - Ecc^2)^2)^{-1} \tag{7.3}$$

$$\dot{RAAN} = 9.9641 ((\frac{E_{EarthEq}}{A_{km}})^{3.5})\cos(Inc)((1 - Ecc^2)^2))^{-1} \tag{7.4}$$

Accordingly the Argument of Perigee ω and Right Ascension of the Ascending Node $RAAN$ are calculated in 7.5 and 7.6 by updating the same parameters given in the TLE ($RAAN_{TLE}$ and ω_{TLE}).

$$\omega = \omega_{TLE} + T_{se}\dot{\omega} \tag{7.5}$$
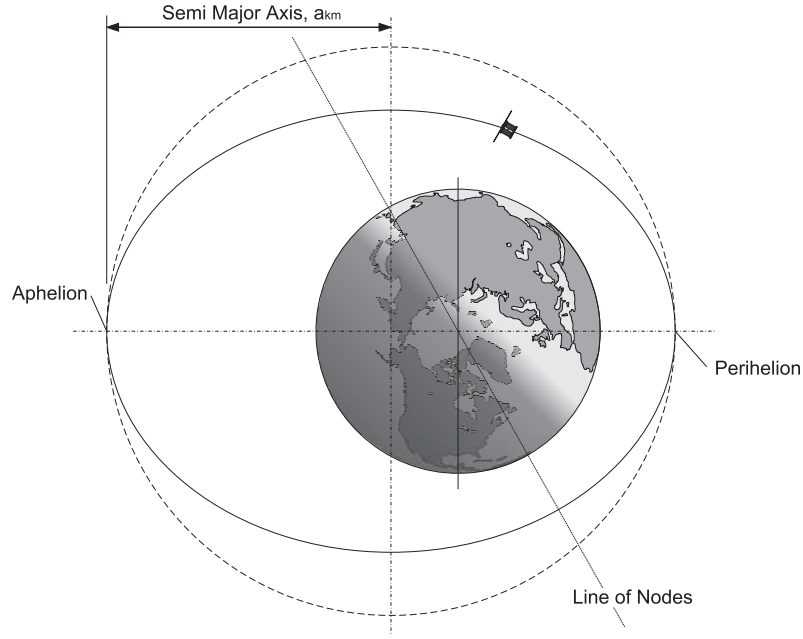
$$RAAN = RAAN_{TLE} - T_{se}\dot{RAAN} \tag{7.6}$$

Figure 7.4: Parameters characterizing the orbit

True Anomaly: The next step is to calculate the satellites True Anomaly v, which is the angle between Perigee and the actual position of the satellite measured with respect to the center of the ECI frame (The center of Earth) as shown in figure 7.3. It is determined out from the satellites current Mean Anomaly M_t and the Orbital Eccentricity Ecc as shown in 7.7.

$$\nu = M_t + 2Ecc\sin(M_t) + 5Ecc^2\frac{\sin(2M_t)}{4} \tag{7.7}$$

Argument of Latitude: The Argument of Latitude lat represents the angle between the line of nodes and the current position of the satellite with respect to the center of the ECI frame. It is calculated as the sum of the Argument of Perigee ω and the True Anomaly ν (7.8).

$$lat = \omega + \nu \tag{7.8}$$

Position Vector in ECI Frame: Based on the Argument of Latitude lat, the Right Ascension of Ascending Node $RAAN$ and the Inclination of the satellites orbit Inc, the position of the satellite can be determined as a unit vector in the ECI frame, by using equation 7.9

$$
\begin{aligned}
x_{sat} &= \cos(lat)\cos(RAAN) - \sin(lat)\sin(RAAN)\cos(Inc) \\
y_{sat} &= \cos(lat)\sin(RAAN) + \sin(lat)\cos(RAAN)\cos(Inc) \\
z_{sat} &= \sin(lat)\sin(Inc)
\end{aligned}
\tag{7.9}
$$

Orbital Radius: To calculate the orbital position of the satellite in kilometers, the position vector given in equation 7.9 is multiplied with the radius of the satellites orbital position r_{sat} (in Kilometers) as shown in equation 7.10.

$$r_{sat} = A_{km}\frac{1 - Ecc^2}{1 + Ecc\cos(\nu)} \tag{7.10}$$

58

7.2.3 Verification of the Orbit Models

The verification of the orbit models includes the testing of both the on-board Kepler orbit model and the more complex SGP4 model in relation to requirement S4.1 and as described in the test specifications TS4.1.

To verify the orbit models data from the ØRSTED satellite was used, which is described in F. This data has been taken with the satellites GPS module and gives the satellites position in the ECEF coordinate frame at a certain time.

The satellite position data was used to verify the SGP4 model, used to simulate a satellites position in Simulink, and the on-board orbit model, which represents the simpler Kepler model, which later will be implemented aboard the CubeSat.

As the data from the ØRSTED measurements was taken in the ECEF frame, it first had to be transformed to data in the ECI coordinate frame, as both the SGP4 and the on-board orbit model are producing outputs in this coordinate system.

The setup of the Simulink file used to verify the SGP4 and the on-board orbit model can be seen on figure 7.5. The ØRSTED orbit data used was giving the satellites position throughout 7 days, beginning with the
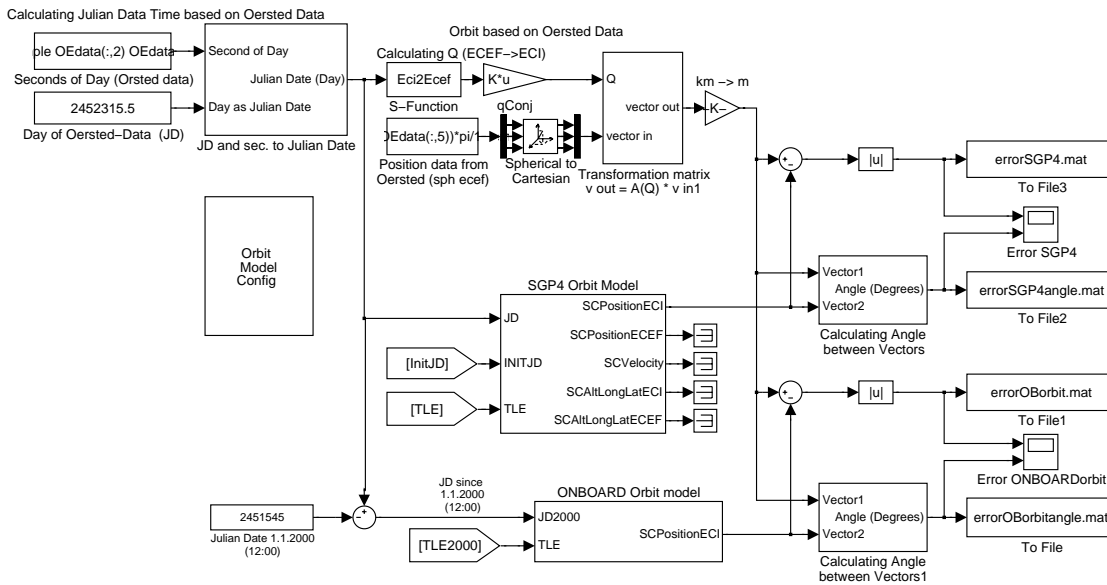

Figure 7.5: The Simulink model used to verify the SGP4 and the on-board orbit model by using data from the ØRSTED satellite.

position data of the 10.th of February 2002 and ending with the data of the 17.th of February. The two line elements or NORAD lines used were, according to their epoch time, taken on the 10.th of February.

Accordingly the errors between the models and the real data was calculated as vector errors in meters and as angular errors in degrees. The error of the SGP4 model can be seen on figure 7.6 and the error of the on-board orbit model for the CubeSat is shown on 7.7. Based on the plots of the data it can be seen, that the error of the SGP4 model based on the ØRSTED position data after 7 days was below 0.27 degrees. The error of the on-board orbit model was after 7 days below 0.43 degrees.

Based on these results it has been concluded, that the SGP4 model and the orbit model are working correctly and as expected.

The difference between their output and the data of the real satellite position measurements taken by the ØRSTED satellite are below 0.5 degrees. In an orbital height of 700 km this error angle corresponds to a distance of 61.77 km as shown in equation 7.11.

$$\text{Error}_{\text{Orbit Pos}} = (R_{Earth} H_{Orbit}) \sin(0.5°) = (6378.135 \, km + 700 \, km) \sin(0.5) = 61.77 \, km \quad (7.11)$$
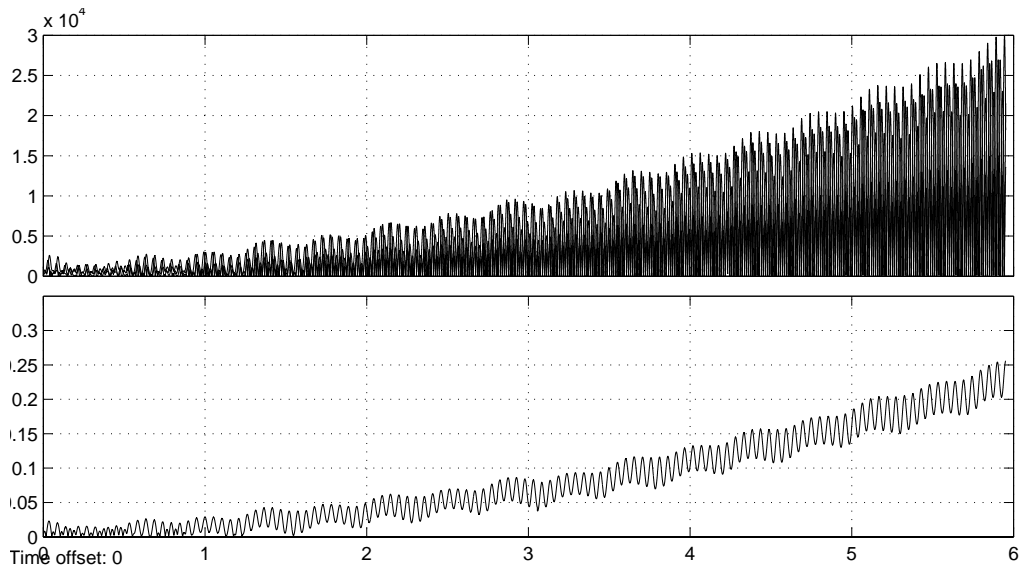
Figure 7.6: The difference between the SGP4 model and the ØRSTED position data given in meters (top graph) an as an angle in degrees (bottom graph).
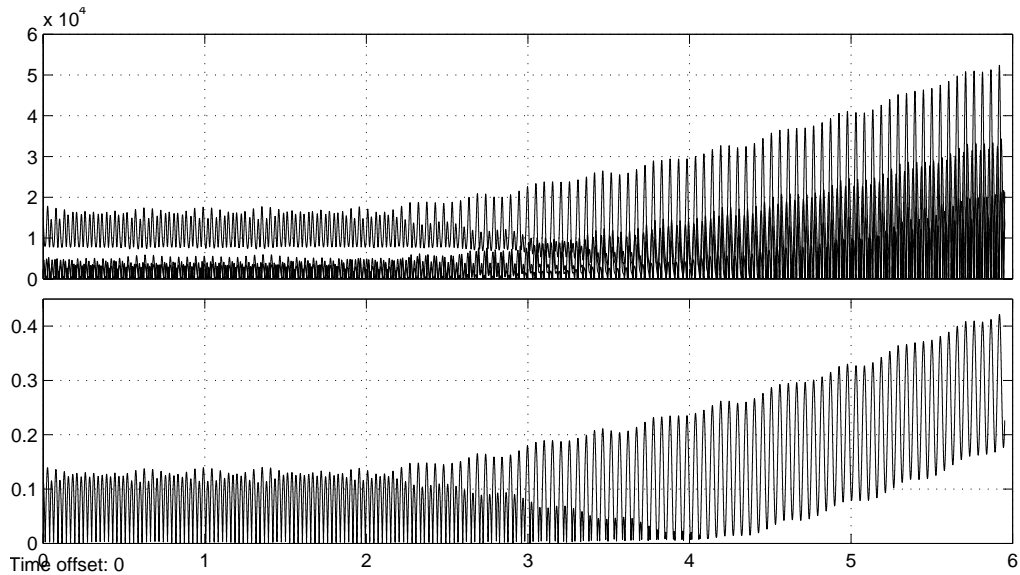

Figure 7.7: The difference between the on-board orbit model and the ØRSTED position data given in meters (top graph) an as an angle in degrees (bottom graph).

Hereby the two orbit models have been proven to be close enough to the real world data, to fulfill requirement S4.1 regarding the accuracy of 100 km. It has been verified that the models are appropriate for simulating the orbit of the satellite (SGP4) and for determining the orbital position on-board the satellite (on-board orbit model).

7.3 Summary

One of the requirements of the ADS is the satellites knowledge about its own current position. For this purpose an orbit model is implemented to calculate the position based on the current time as Julian date and the parameters describing the orbit, which are given in the Two Line Element (TLE) sets.

As the more accurate SGP4 orbit model is too complex for the implementation on-board the AAU CubeSat, a simpler Kepler orbit model is developed.

This model and the SGP4 orbit model, which will be used in a satellite simulation, were tested by comparing them with real orbit data measured by the ØRSTED satellite. Both proved to have the necessary accuracy as required, and will therefore be used on-board the satellite and as reference in the simulation.

chapter 8

Sun Model and Earth Albedo

In this chapter the truth sun model and the on-board sun model are described and validated in a simulation, by comparing them with other reference sun models. Next a insight will be given into the problems connected to the disturbances in the sun sensor measurements caused by Earth albedo. The effect of the Earth albedo is evaluated and a albedo correction is presented to reduce this effect.

8.1 The sun model

The sun model on-board the satellite is used to determine the direction to the Sun in the ECI frame for the attitude determination. Though, it is in fact the Earth which orbits around the Sun, in the Earth Centered Inertial (ECI) frame, the Sun will be changing position while the Earth is centered in Origo. The sun model includes the same parameters and equations as the on-board orbit model, described in chapter 7. However, many of the parameters, which are needed to calculate the position of the Sun in the ECI frame, are well known and not changing much through time. This simplifies the model and reduce the necessary calculations.

The Epoch Mean Anomaly $M_{SunEpoch}$ of the Sun is given for the 1st of January 2000 at noon UTC, just like the on-board orbit model uses a Julian Date referring from 2000 as input JD_{2000}. Since the Mean Motion of the Sun n_{sun} is well known too, this can be used to describe the current Mean Anomaly M_{Sun}, as shown in equation 8.1

$$M_{Sun} = M_{SunEpoch} + n_{sun} JD_{2000} = 357.528 + 0.9856003 JD_{2000} \tag{8.1}$$

The position of the Sun in the ECI frame in orbital plane (the ecliptic longitude) is given by equation 8.2. To calculate the ecliptic longitude of the Sun most of the parameters, which characterize the orbital motion of the Sun, are already inserted into the equation. Due to this the only input needed is the Julian Date JD_{2000} and the current Mean Anomaly of the Sun M_{Sun} given in equation 8.1.

$$V_{Sun} = 280.461 + 0.9856474 JD_{2000} + 1.915 \sin(M_{Sun}) + 0.020 \sin(2M_{Sun}) \tag{8.2}$$

To transfer the position in the orbital plane into the ECI frame requires the tilt of the Earth's rotational axis, which also represents the Z-axis of the ECI frame. The same parameter is also known as the obliquity of the ecliptic plane and is given in equation 8.3.

$$\epsilon = 23.4393 - 0.0000004 JD_{2000} \tag{8.3}$$

The position of the Sun is determined as a unit vector in the ECI frame. This is done in equation 8.4 by transforming the ecliptic longitude of the Sun V_{Sun} into Cartesian coordinates by including the obliquity of the ecliptic plane ϵ.

$$\begin{aligned} X_{Sun} &= \cos(V_{Sun}) \\ Y_{Sun} &= \cos(\epsilon) \sin(V_{Sun}) \\ Z_{Sun} &= \sin(\epsilon) \sin(V_{Sun}) \end{aligned} \tag{8.4}$$

The Simulation of Sun Sensor Signals

The output of the sun model used as reference in the simulation is also used to generate simulated input signals on the sun sensors of the CubeSat. The sun sensor are mounted on each side of the CubeSat referring to a positive and negative direction on the axes of the SCB frame. Accordingly the simulation of sun sensor signals is simply archived by rotating the sun direction vector into the SCB frame and applying a signal on each sensor which is pointing in the same direction. This is done by taking the angle between the normal vector of each sun sensor and the sun vector into account. Sun sensors pointing in the opposite direction of the sun vector are left blank.

8.1.1 Verification of sun models

The verification of the sun models is fulfilled according to requirement S4.3 and as given in the test specifications TS4.3. In this verification the on-board sun model and the truth sun model, in figure 8.1 called *SunPosModel*, are compared to other existing sun models.
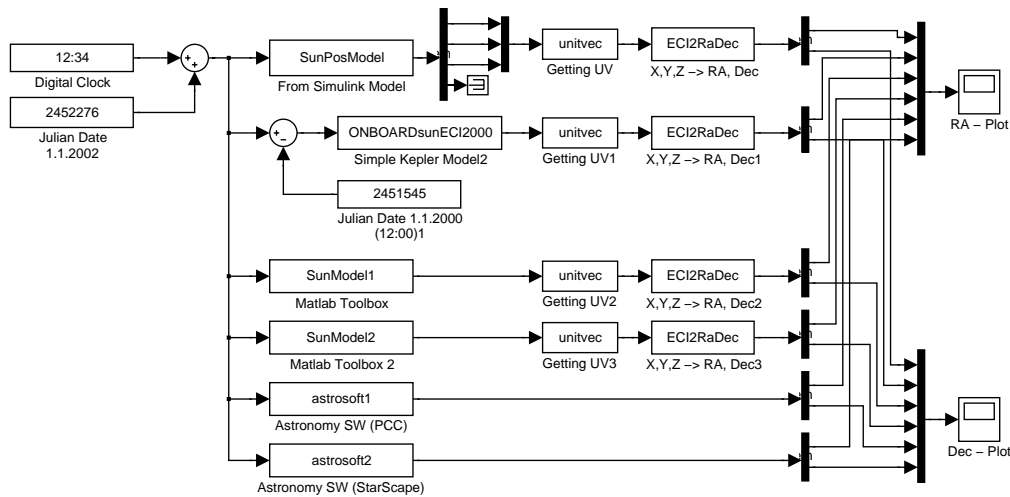

Figure 8.1: The Simulink model used to verify the sun models.

References for the sun model

To ensure the correctness of these two sun models they have been compared with the following algorithms as reference:

1. A sun model called *SunV1* which generates the sun vector in the ECI frame. This sun model is from the *SPACECRAFT CONTROL TOOLBOX V4.0*, developed and published by *Princeton Satellite Systems* in 2000. The toolbox contains a number of models and algorithms for simulating attitude and orbit control in the Matlab environment.

2. A sun model called *SunV2*, which computes the sun vector using a moderate precision model, which also is obtained from the *SPACECRAFT CONTROL TOOLBOX V4.0*.

3. Time and position samples of an astronomy software program for DOS called *PC-Cosmos-3.0*. It was developed in 1990 by Astrosoft Inc. (Microsoft Cooperation) and used for astronomical and educational purposes. It is used by applying different Julian dates as input and reading the according positions of the Sun given in the ECI frame.

4. Time and position samples of a free-ware astronomy software called *StarScape for Windows Version 1.54*, which uses astronomical data based on the Yale Star Catalog. This software runs on *Windows 3.1*, was published by Skyline Software in 1994. It is available on the Internet for free. It is used in a similar way as *PC-Cosmos-3.0* by using certain Julian Dates as input and reading the output containing the position of the sun in the ECI frame.

The two Matlab functions of the Satellite Toolbox are applied directly, while there are taken 12 samples of the suns position over the year 2003 (Each sample on the 12. of the month at 12:00 UTC) by using the two astronomy programs. The Simulink model used for comparing these functions and plotted values is shown in figure 8.1 and the results are plotted in figure 8.2 and 8.3.
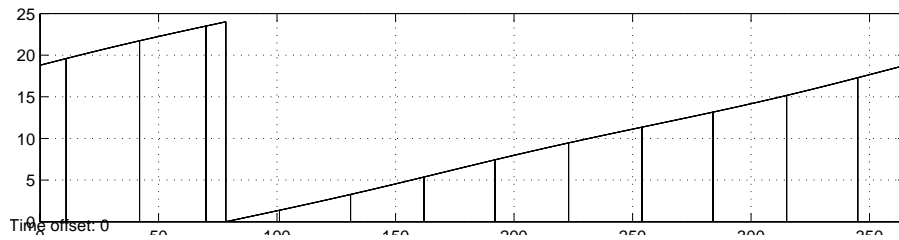

Figure 8.2: A plot of the suns Right Ascension throughout a year given by the 4 Matlab functions and the 12 samples from the astronomy software.
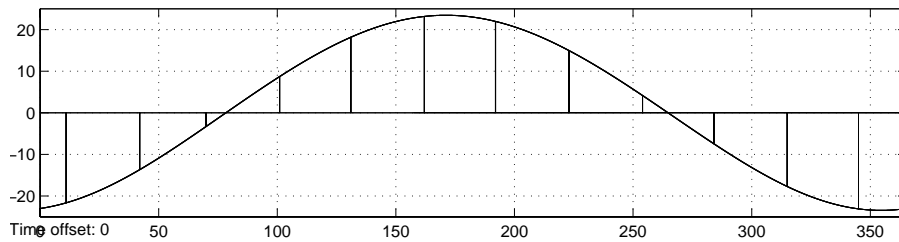

Figure 8.3: A plot of the suns Declination throughout a year.

The plots of the four functions and the samples of the astronomy software can be seen on figure 8.2, showing the right ascension, and on figure 8.3, showing the declination of the sun throughout the year 2002. The position plotted over time for the sun models implemented in Simulink are very similar, and also pass through the twelve samples from the astronomy software. This also includes the sun model used on-board the satellite.

It is was discovered that the truth model *SunPosModel*, differ slightly from the rest. The error between the sun model *SunV1* and each of the other models is plotted in figure 8.4. The error between the truth model and the other models is about $0.25°$.

Using the sun model *SunPosModel* as a truth model, an error is simulated for the on-board sun model. As the difference between the all sun models is very small and fulfills the requirement S4.3 regarding accuracy, it is decided, not to verify the sun models further. Especially as sun sensors are expected to have a much higher error due to Earth albedo, the error of the on-board model is negligible.

8.2 Earth Albedo

Earth albedo is an expression for the reflectivity of Sun light by the Earth surface and atmosphere. The Earth Albedo is varying as it is depending on the visible surface of the Earth and the amount of clouds in
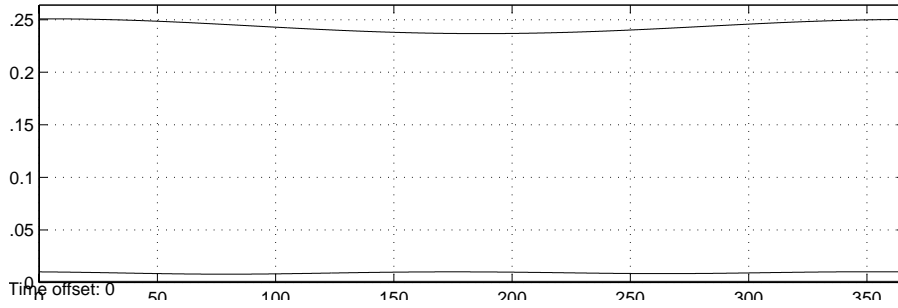
64

Figure 8.4: The differences between the sun model of the Matlab Satellite Tool-box 'SunV1' and the three other sun models in degrees.

the atmosphere. The average value of the Earth albedo is 30% ±5% of direct solar flux (Wertz, 1978). As the AAU CubeSat is relatively close to the Earth at a height of 700 km, the surface of Earth albedo covers 130° of the satellites field of view, as calculated in equation 8.5.

$$\alpha_{Earth} = 2\arcsin\left(\frac{R_{Earth}}{R_{Earth} + H_{SatelliteOrbit}}\right) = 2\arcsin\left(\frac{6378.135 km}{6378.135 km + 700 km}\right) = 128.6° \approx 130°$$

(8.5)

Because of this surface area giving albedo light, the sun sensors will get input from albedo light in several different angles, while light from the Sun can be assumed to come from a single direction. A simple model of how Earth albedo affect the sun sensor readings is developed for use in simulations. The following assumptions are made for this purpose.

A sun sensor pointing towards the Earth horizon will almost have 50% of its field of view covered with albedo light and the incoming albedo light. Due to this effect the input on the sensor would be about 50% of the Earth albedo, which is approximately 15% of the incoming sunlight. In the same way would a sensor pointing in direction of nadir receive 100% of the Earth albedo, which accordingly would be 30% of the incoming sunlight.

8.2.1 Earth albedo model

The following assumptions are specified to model the effect of Earth albedo on a single sun sensors:

1. The Earth albedo is approximately 35% of the sun light intensity.

2. The sun sensors have a field of view of 180°

3. When the angle between the sun sensors pointing direction and the nadir vector is smaller than 25°, the entire Earth surface and 100% of albedo will be measured

4. When the sun sensor tangents the horizon (Angle between nadir vector and Sun sensor vector equal 65°), 50% of the Earth will be visible and 50% of Earth albedo will be measured.

5. When the sun sensor is pointing away from the Earth surface and in a direction perpendicular on the Earth horizon (Angle between nadir vector and Sun sensor vector larger than 147.5°) the amount of incoming albedo light is zero.

6. The Earth albedo disappears a few minutes before eclipse and appears a few minutes after coming out of eclipse. More specifically, no Earth albedo is present when the angle between sun vector and nadir vector is lower than 65°.
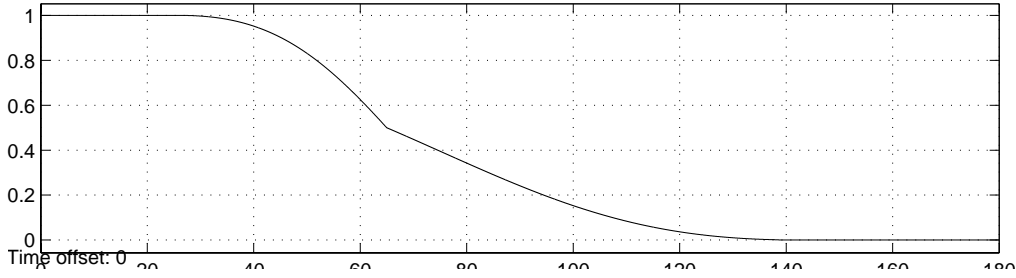
Figure 8.5: A plot of the modeled Earth albedo as function of angle between sun sensor pointing direction and nadir vector.

A plot of the approximate amount of albedo in relation to the angle between the sensors pointing direction and the nadir vector can be seen in figure 8.5.

The albedo model is only an attempt of simulating the effect of Earth albedo on the sun sensors. It does not take all factors into account, as for example the situations when only a part of the Earth is lit up by sunlight while the other part remains dark. The purpose of the model is in simulations to apply an error to the sun sensors, which is not accounted for in the on-board sun model.

8.2.2 Albedo Correction

Instead of trying to separate the Earth albedo disturbance from the sun sensor measurements, Earth albedo is added to the sun vector from the on-board sun model. In this way it is not the direction to the Sun, which is used in the deterministic attitude determination or extended Kalman filter, but a Sun vector including albedo effect.

Earth albedo is added in the sun model by adding a nadir-vector to the sun vector with a length of 30% of the sun vector. The nadir vector is found using the on-board orbit model. It is possible to come up with more sophisticated albedo corrections, which would reduce the simulated sun sensor error even more. However, without a precise model for simulating Earth albedo, it is decided to keep the albedo correction simple.

Test of the Albedo correction

To evaluate the impact of the albedo disturbance on the sun sensors and the necessity of using an albedo correction a simulation is set up in Simulink.

Two scenarios of using a sun model with and without albedo correction are tested in a simulation. The measurements from the sun sensors including the albedo disturbance are measured for a satellite pointing the camera away from the sun and for an attitude pointing a corner with solar cells towards the sun. The two constant attitudes of the satellite, corresponding to camera mode and power save mode, are given by the two quaternions q_{CAM} and q_{PS}, as described in equation 8.6.

$$q_{CAM} = \begin{bmatrix} 0 \\ 0 \\ \sin(\frac{270°}{2}) \\ \cos(\frac{270°}{2}) \end{bmatrix} = \begin{bmatrix} 0 \\ 0 \\ 0.7071 \\ -0.7071 \end{bmatrix} \qquad q_{PS} = \begin{bmatrix} 0 \\ 0 \\ \sin(\frac{225°}{2}) \\ \cos(\frac{225°}{2}) \end{bmatrix} = \begin{bmatrix} 0 \\ 0 \\ 0.9239 \\ -0.3827 \end{bmatrix} \qquad (8.6)$$

These attitudes in the ECI frame, correspond to a rotation of the SCB frame of 270° and 225° around the Z-axis in the ECI frame.

Simulated sun sensor measurements in the SCB frame are rotated into the ECI frame and compared with the sun position, which is determined by the sun model, and with a sun model using an albedo correction.

The angular errors between the vectors during one orbit in the sunlight are plotted and shown in figure 8.6 and 8.7.
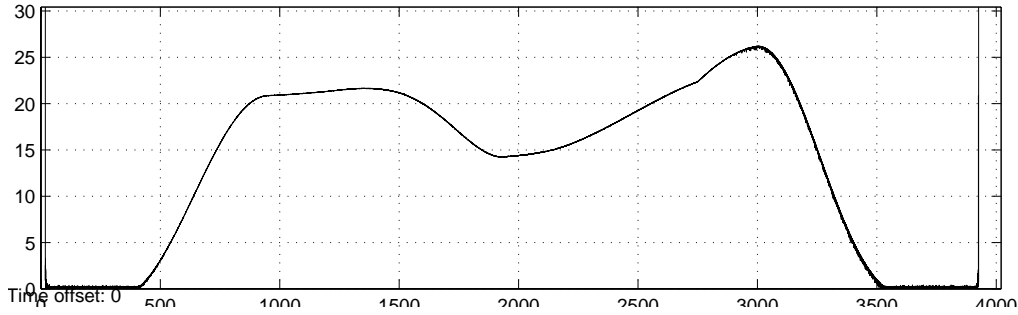

Figure 8.6: The error angle between the sun sensor measurements and the sun direction without albedo correction
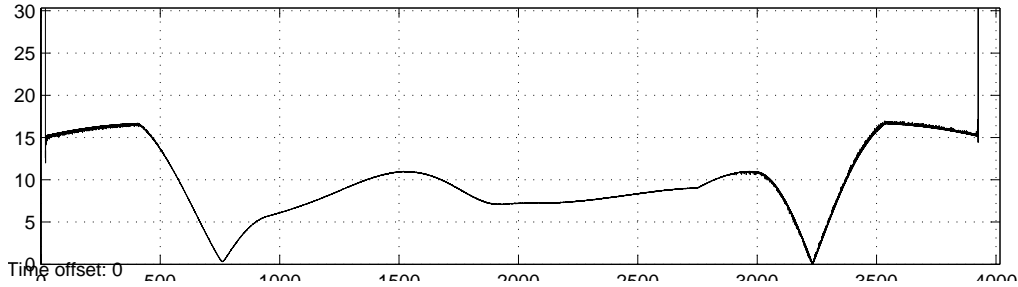

Figure 8.7: The error angle between the sun sensor measurements and the sun model used including the albedo correction

Based on the two simulations it can be seen, that the albedo correction reduces the angular error between the measured data and the on-board model from around $20°$ to less than $10°$. The RMS values of these error angles are accordingly $8.8910°$ when albedo correction is used, and $18.2296°$ when the sun data is compared with a sun model without albedo correction. These RMS values were taken over the interval, when the sun sensors are exposed to albedo.

The variance of the error between the unit measurement vector and the unit sun vector from the sun model without albedo correction, was found to be 0.0021.

In the test scenario where the satellite points three solar panels towards the Sun, the plotted angular errors are almost similar to the ones plotted in figure 8.6 and figure 8.7. The RMS values of these error angles of the satellite in power save mode are accordingly $9.3129°$ when albedo correction is used, and $18.5865°$ when the sun data is compared with a sun model without albedo correction.

On the plot the error of the albedo corrected vector is highest just after the end of the eclipse and before the begin of the next eclipse. This is due to the fact, that the sun vector of the on-board sun model contains an albedo correction while there is no albedo visible yet. Due to this the error of the sun model without albedo correction is close to zero as no other light source is visible except the sun.

To avoid this the albedo correction can be modified to be zero during the time, when albedo light is not present or very low. An option to solve this problem is to connect the sun sensor measurements to the albedo correction, as this is the most reliable source to detect, if albedo is present. It can be achieved by measuring the inputs to the sun sensors and measuring, if there are more than three sensors which are getting an input above a given threshold, and which in this way could not come from the sun or be caused by minor disturbances.

8.3 Summary

For the determination of the satellites attitude with sun sensors a knowledge about the direction to the Sun in the ECI frame is required. This is obtained by the use of an on-board Sun model, described in section 8.1, which calculates the direction to the Sun based on the current time given as Julian date.

The on-board sun model and the truth sun model used when simulating the performance of the attitude determination have been verified by comparison to other sun models and astronomy software.

A major disturbance acting on the measurements of the direction to the Sun is the Earth albedo. It consists of approximately 30% $\pm$5% of the Sun light, which is reflected by the large surface and atmosphere of the Earth seen from the satellites position. A model for simulating Earth albedo was developed. The simulated Earth albedo caused RMS angular errors in the measured sun vector of approximately $18\,^\circ$ to 19°.

To reduce the effect of the Earth albedo an albedo correction has been included in the on-board sun model. When introducing the albedo correction simulations revealed a reduction in angular error of the sun vector to approximately 8° to 9°. However, as the albedo correction is not needed in situations, when only the sun but no albedo is visible, an error is introduced in these cases. Therefor it is recommended to implement a further algorithm which turns the albedo correction on or of depending on, if and how much albedo light is measured by the sun sensors.

chapter 9

Magnetic field model

A magnetic field model is needed on-board the satellite, for determining a magnetic field vector in the ECI frame. A thruth model of the magnetic field is also needed for simulation of the attitude determination performance. The International Geomagnetic Reference Field (IGRF) model will be used in both cases. The IGRF model is updated with a set of coefficients to represent the main field at a particular epoch, usually every five years. Coefficients used for the IGRF2000 model are based on data from the Danish satellite Ørsted.

9.1 The IGRF model

The magnetic field vector B can be expressed as a sum of spherical harmonics $B_{n,m}$, as given in equation 9.1.

$$B = \sum_{n=1}^{\infty} \sum_{m=0}^{\infty} B_{n,m} \tag{9.1}$$

The contribution of spherical harmonics are of degree n and order m, and is given by equation 9.2.

$$B_{n,m} = \frac{K_{n,m} a^{n+2}}{R^{n+m+1}} \left\{ \frac{g_{n,m} C_m + h_{n,m} S_m}{R} [(s_\lambda A_{n,m+1} + (n+m+1) A_{n,m}) \hat{r} - A_{n,m+1} \hat{e}_3] \right.$$
$$\left. - m A_{n,m} [(g_{n,m} C_{m-1} + h_{n,m} S_{m-1}) \hat{e}_1 + (h_{n,m} C_{m-1} - g_{n,m} S_{m-1}) \hat{e}_2] \right\} \tag{9.2}$$

a Mean radius of the Earth 6371 km

R Magnitude of position vector from geometric center of the Earth. This is provided from an orbit model, providing the position vector of the satellite.

r̂ Unit vector in direction of R is found using the orbit model.

ê Mutually perpendicular unit vectors $\hat{e}_1$, $\hat{e}_2$ and $\hat{e}_3$ parallel to the x, y and z axes of the ECEF frame.

n Degree of contributing spherical harmonics

m Order of contributing spherical harmonics

$\mathbf{K_{n,m}}$ Coefficients that relate Schmidt functions to associated Legendre functions.

$\mathbf{A_{n,m}}$ Derived Legendre polynomials of degree n and orders m.

$\mathbf{s_\lambda}$ Sine of the geographic latitude λ

$\mathbf{g_{n,m}}$ $\mathbf{h_{n,m}}$ Schmidt-normalized Gauss coefficients of degree n and order m. The Gauss coefficients used for the magnetic field model are obtained from (DSRI, 2002) for the epoch 2000.

(Roithmayr, 1992)

9.2 Verification of magnetic field model

IGRF models of differing orders are testet according to test specification TS4.2. As described in appendix F, data from the satellite Ørsted is used for validating the model. This data contains position data for the satellite together with the measured magnetic field. The Simulink model for finding errors between an IGRF model and Ørsted data can be seen in figure 9.1.
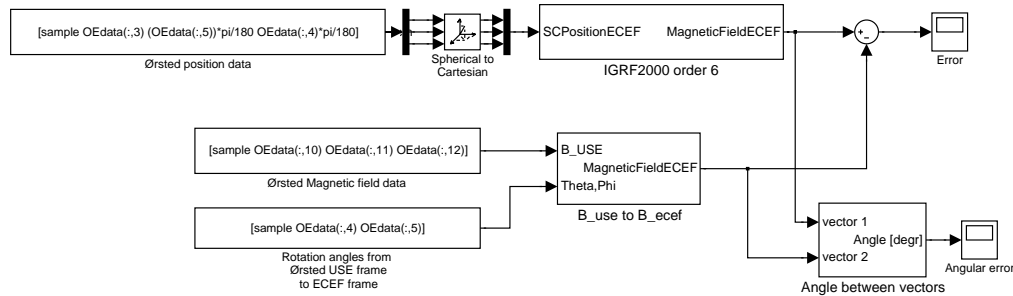

Figure 9.1: Simulink simulation for testing IGRF models of orders 2 to 13 against Ørsted data.

IGRF2000 models of different orders from 2 to 13 are compared to Ørsted data from feb 9 year 2000 to feb 10 year 2002. The resulting magnetic field strength errors in nT and the angular errors are plotted in appendix F. In table 9.1 RMS errors and maximum errors between Ørsted data and IGRF models of differing orders are listed.

Error of magnetic field strength [nT]												
Order	2	3	4	5	6	7	8	9	10	11	12	13
Error$_{rms}$	3972	1849	677	328	205	128	120	114	114	114	114	114
Error$_{max}$	7849	4275	1648	838	810	853	855	840	837	842	843	844

Angular error of magnetic vector [deg]												
Order	2	3	4	5	6	7	8	9	10	11	12	13
Error$_{rms}$	5.585	2.441	0.999	0.522	0.309	0.215	0.197	0.189	0.188	0.188	0.188	0.188
Error$_{max}$	18.44	6.260	3.837	1.449	1.175	1.130	1.137	1.115	1.111	1.118	1.119	1.120

Table 9.1: Errors between Ørsted data and IGRF models of order and degree 2 to 13

9.2.1 Choice on-board IGRF model

The RMS error between Ørsted measurements of the magnetic field and an IGRF model of order six is 205 nT and the max error is 810 nT. Choosing models of lower order rapidly encreases this error. The RMS error of the IGRF model of order six fulfills requirement S4.2.

9.2.2 Choice of Geomagnetic field truth model

A truth model of the Earth magnetic field is needed when simulating the performance of the attitude determination system. The accuracy of the on-board IGRF model relative to the Geomagnetic field truth model, is chosen to include modelling errors, magnetometer errors and errors due to uncertainty of satellite position.

The expected modeling error is given for the on-board IGRF model of order 6 in table 9.1. In (Bak, 1999) it is stated that simply using an IGRF truth model of higher order than the on-board model, will not give a true representation of the modeling error. Though, for simplicity it has been chosen to simulate this error using an IGRF model of higher order.

The satellite position is used as an input to the on-board magnetic field model. This means that an error in the determined position results in an error of the determined magnetic field. In section 7.2.3 the error of the on-board orbit model is constant within the first 2.5 to 3 days after new TLEs have been uploaded. In appendix F, the resulting RMS error of the on-board magnetic field model for this time period is determined to be $0.21°$.

The maximum error specified for the magnetometer in table 5.2 is $0.6°$ but the typical error is $0.16°$, derived from specifications for the magnetometer. However, this does not include distortion of magnetic field, due to the structure and other components in the satellite. For simulations the total magnetometer RMS error including distortion of the magnetic field, is assumed to be $0.5°$. This is after calibration for constant magnets of the magnetometer. In section 6.3.3, an error of $0.1°$ has been assumed due to misalignment of the magnetometer. After integration of magnetometer, these values may be updated for simulations.

The error budget to be simulated using a truth model is given in table 9.2. The errors are expected uncorrelated and the Root-Sum Square (RSS) error is determined.

Error source	RMS angular error
Modelling error (order 6)	$0.31°$
Position uncertainty (2.5 days old TLE)	$0.21°$
Magnetometer error (Calibrated)	$0.5°$
Magnetometer misalignment (Calibrated)	$0.1°$
RSS Error	$0.63°$

Table 9.2: Error budget to be simulated with the truth model relative to the on-board model.

It is found that in order to simulate an error as specified in table 9.2 an IGRF model of order 10 is used as truth model. However, the variance of the error between an IGRF model of order 10 and an order 6 model, as used on-board, is to small. For this reason, when testing the extended Kalman filter, in chapter 11, data is used from an order 10 and an order 4 IGRF model. Simulations have shown that the RMS error between two such models is approximately $0.61°$. The on-board magnetic field model to be implemented for the attitude determination, is of course still of order 6.

chapter 10

Deterministic Attitude Determination

This chapter presents the deterministic attitude determination. The algorithms which can be used to determine the attitude based on the on-board models and vector measurements. There will be given a short description of the TRIAD algorithm and the algorithms connected to the solution of Wahba's Problem. Finally the benefits and disadvantages of the different algorithms will be evaluated to choose the most suitable one for the Deterministic Attitude Determination of the AAU CubeSat.

10.1   Introduction

The method of determining the attitude of the satellite consists of using the data collected by the sun sensors and magnetometer and the output of the on-board models describing the magnetic field and the direction to the sun in reference to the satellites position. These vector pairs determined in the orbital frame and measured in the spacecraft body frame are used in an deterministic attitude determination algorithm, which will produce the attitude of the spacecraft as an output, consisting either of a rotational matrix or quaternion.

According to (Markley, 2002) the earliest algorithm for determining the attitude of a spacecraft, when given two vector measurements, is the TRIAD algorithm. Other algorithms find the optimal attitude matrix, that minimizes the loss function as proposed by Wahba (Wahba, 1965).
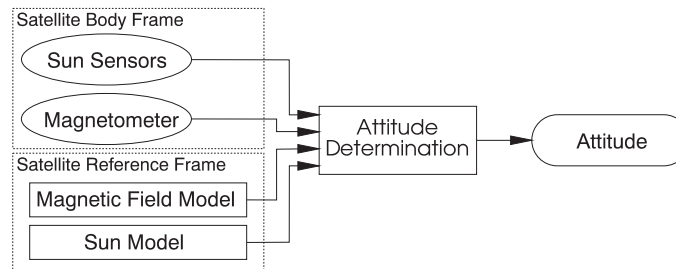

Figure 10.1: The vectors from the sensors and from the models are used for determining the rotation from the satellite reference frame to the satellite body frame. This rotation is the attitude of the satellite.'

10.2   The TRIAD Algorithm

The TRIAD algorithm is simple to implement but does not treat the observations optimally (Markley, 2002). It consist on constructing two triads of orthonormal unit vectors using the vector information available. Initially it assumes that one of the vector measurements is more exact than the other. The vector measurements in the spacecraft body frame are named b_1 and b_2, and the vectors in the reference frame r_1 and r_2. It is assumed that the first vector measurement b_1 is the most reliable. Based on this three triads are set up as in equations 10.1, 10.2 and 10.3 (Hall, 2002).

$$t_{1b} = b_1 \qquad\qquad t_{1r} = r_1 \tag{10.1}$$

$$t_{2b} = \frac{b_1 \times b_2}{|b_1 \times b_2|} \qquad\qquad t_{2r} = \frac{r_1 \times r_2}{|r_1 \times r_2|} \tag{10.2}$$

$$t_{3b} = t_{1b} \times t_{2b} \qquad\qquad t_{3r} = t_{1r} \times t_{2r} \tag{10.3}$$

Finally the attitude matrix A_{triad} based on the three triads can be written as shown in equation 10.4.

$$A_{triad} = [t_{1b} t_{2b} t_{3b}][t_{1r} t_{2r} t_{3r}]^T \tag{10.4}$$

However, when applying this algorithm on two exact vector pairs it will result in a rotation matrix, which represents the rotation of the second vector (r_2 to b_2) with a much lower precision than the rotation of the first vector (r_1 to b_1).

10.3   Wahba's Problem

In 1965 Grace Wahba proposed that the attitude of a satellite is found as a least squares estimate of the rotation matrix, which carries the known frame of reference into the satellite fixed frame of reference (Wahba, 1965).

In equation 10.5 A is an orthogonal matrix, which rotates unit vectors from a reference frame r_i to a body frame b_i. This is done by minimizing the loss function $L(A)$ (Markley, 2002).

$$L(A) = \frac{1}{2} \sum a_i |b_i - Ar_i|^2 \tag{10.5}$$

The nonnegative weights a_i are used for weighting the vector pairs. Wahba's loss function can also be written as in equation 10.6.

$$L(A) = \sum a_i - tr(AB^T) \tag{10.6}$$

Where B is given by equation 10.7.

$$B = \sum a_i b_i r_i^T \tag{10.7}$$

Based on 10.6 the loss function $L(A)$ is minimized by maximizing $tr(AB^T)$.

In (Markley and Mortari, 1999) 8 different methods for minimizing Wahba's loss function were described and compared with respect to accuracy, robustness and computational burden. These results can be used for finding the most suitable algorithms to solve Wahba's Problem, which would be the alternative to the TRIAD algorithm when determining the attitude of the satellite.

10.4   Methods for minimizing Wahba's Loss Function

The algorithms considered in (Markley and Mortari, 1999) for minimizing Wahba's loss function are the following:

Davenports q-method: This method to solve Wahba's Problem has been used in spacecraft applications for quite a while. The q-method determines the rotational matrix A as a quaternion by computing the symmetric 4x4 matrix K.

$$K = \begin{bmatrix} B + B^T - ItrB & z \\ z^T & trB \end{bmatrix} \qquad\qquad z = \begin{bmatrix} B_{23} - B_{32} \\ B_{31} - B_{13} \\ B_{12} - B_{21} \end{bmatrix}$$

The eigenvector of K with the largest eigenvalue will in this way give the optimal quaternion representing the rotation.

$$Kq_{opt} = \lambda_{max} q_{opt} \tag{10.8}$$

The key part of this algorithm consists of determining the eigenvector λ_{max}, which also is required in some of the other algorithms QUEST, FOAM, ESOQ and ESOQ2. In case of the Attitude Determination System only two vector observations are available; the magnetic field and the direction of the sun. This fact speeds up the fast algorithms as the eigenvector λ_{max}, can be defined as in equation 10.9.

$$\lambda_{max} = \sqrt{a_1^2 + a_2^2 + 2a_1 a_2 [(b_1 * b_2)(r_1 * r_2) + |b_1 \times b_2||r_1 \times r_2|]} \tag{10.9}$$

Single Value Decomposition (SVD): The single value decomposition represents a method, which is easy to understand and to analyze compared with the other methods. It consists of performing a single value decomposition on the matrix B and using the outputs of the unitary matrixes U and V to calculate the optimal rotational matrix A_{opt}.

$$A_{opt} = U diag \begin{bmatrix} 1 & 1 & (detU)(detV) \end{bmatrix} V^T$$

However, the computation is significant and the SVD method is mainly used for analytical studies.

Quaternion Estimator (QUEST): The quaternion estimator is one of the fastest algorithms so far and also one of the most widely used for solving Wahba's problem. It is based on the task of solving the equation 10.10.

$$det(K - \lambda I) = 0 \tag{10.10}$$

for the eigenvalue λ. The optimal quaternion is in this case given by the equation 10.4.

$$q_{opt} = \frac{1}{\sqrt{\gamma^2 + |x|^2}} \begin{bmatrix} x \\ \gamma \end{bmatrix}$$

In which γ and x are given by equation 10.11 and 10.12.

$$\gamma = (\lambda_{max}^2 - (trB)^2 + tr(adjS))(\lambda_{max} + trB) - detS \tag{10.11}$$

$$x = [(\lambda_{max}^2 - (trB)^2 + tr(adjS))I + (\lambda_{max} - trB)S + S^2]z \tag{10.12}$$

$$L(A_{opt}) = \lambda_0 - \lambda_{max} \tag{10.13}$$

In these equations the only unknown variable is λ_{max}. If the optimized loss function given by 10.13 is small, λ_{max} can be obtained by Newton-Raphson iteration starting with λ_0 as initial value. As the QUEST method is a fast algorithm, it is also used for real time applications. However, as the method of solving the characteristic equation is said to be one of the worst ways of finding eigenvalues, the QUEST method also is less robust than Davenports q-method.

Fast Optimal Attitude Matrix (FOAM): The Fast Optimal Attitude Matrix algorithm computes its quantities without having to perform the single value decomposition as in the SVD method. Instead it requires to solve the same equation to determine λ_{max} as in the QUEST method. The optimal rotational matrix is accordingly given by the following equations 10.14 and 10.15.

$$A_{opt} = (\kappa\lambda_{max} - detB)^{-1}[(\kappa + ||B||_F^2)B + \lambda_{max} adjB^T - BB^T B] \tag{10.14}$$

$$\kappa = \frac{1}{2}(\lambda_{max}^2 - ||B||_F^2) \tag{10.15}$$

When only two vector observations are used, the optimal attitude estimate also can be given as in equation 10.16 and 10.17.

$$A_{opt} = b_3 r_3^T + (a_1/\lambda_{max})[b_1 r_1^T + (b_1 \times b_3)(r_1 \times r_3)^T] + (a_2/\lambda_{max})[b_2 r_2^T + (b_2 \times b_3)(r_2 \times r_3)^T] \tag{10.16}$$

$$b_3 = (b_1 \times b_2)/|b_1 \times b_2| \qquad r_3 = (r_1 \times r_2)/|r_1 \times r_2| \tag{10.17}$$

FOAM is the slowest of the four fast algorithms (QUEST, FOAM, ESOQ and ESOQ2), but also the most robust and reliable. (Markley and Mortari, 1999).

Estimator of the optimal quaternion (ESOQ or ESOQ1) The ESOQ method is using a priori attitude estimates of the attitude to perform a fast calculation of a quaternion. The ESOQ algorithm is based on the equation 10.18 from Davenports q-method.

$$det(H) = det(K - \lambda_{max}) = 0 \tag{10.18}$$

The optimal quaternion is hereby calculated as the four dimensional cross product of any three columns of the matrix H. This is done by deleting the k'th row and i'th column of H and using it on equation 10.19.

$$(q_{opt})_i = c(-1)^{k+i} det[(H)_{ki}] \tag{10.19}$$

The deleted component in the quaternion is accordingly determined by normalizing the quaternion.

Instead of calculating the quaternion for every step it is also possible to apply first order updates instead. This is possible as higher order updates do not improve the performance of the iterative methods.

Second Estimator of the optimal quaternion (ESOQ2): The last of the fast four algorithms is the ESOQ2 method. This algorithm works similar to the ESOQ method but also takes the rotational angle ϕ and rotational axis e of the quaternion into account. This gives the following equation 10.20.

$$M = (\lambda_{max} - trB)[(\lambda_{max} + trB)I - S] - zz^T \tag{10.20}$$

The rotation axis of the quaternion will be the null vector of the matrix M. Finally the optimal quaternion can be defined as in 10.4.

$$q_{opt} = \frac{1}{sqrt|(\lambda_{max} - trB)y|^2 + (z*y)^2} \begin{bmatrix} (\lambda_{max} - trB)y \\ z*y \end{bmatrix}$$

Similar as in the ESOQ method it is also here possible to use first order updates which favors ESOQ2 for real-time applications.

Optimal Two Observation Quaternion Estimation Method The Optimal Two Observation Quaternion Estimation Method is based on Davenports q method and specific developed for a two observational case (Markley, 2002). It uses three vector pairs for the determination of the attitude in shape of a quaternion; the measurement-vectors in SCB frame, the model-vectors in SCO frame and two vectors orthogonal on the vectors in SCB and SCO frame shown in equation 10.21.

$$r_n = (r_1 \times r_2)/|r_1 \times r_2| \qquad b_n = (b_1 \times b_2)/|b_1 \times b_2| \tag{10.21}$$

The transformation from the reference in the SCO frame to the body frame would include an rotation around r_n through an arbitrary angle ϕ_r, followed by an rotation around b_n through an arbitrary

angle ϕ_b. Finding the angle ϕ, being the sum of the two angles ϕ_r and ϕ_b, which minimizes the loss function 10.22.

$$L(A) = a_1 + a_2 - (1 + b_n * r_n)^{-1}(\alpha cos(\phi) + \beta sin(\phi)) \tag{10.22}$$

In this equation the two variables α and β are given by equation 10.23 and 10.24.

$$\alpha = (1 + b_n * r_n)(a_1 b_1 * r_1 + a_2 b_2 * r_2) + (b_n \times r_n)(a_1 b_1 \times r_1 + a_2 b_2 \times r_2) \tag{10.23}$$

$$\beta = (b_n + r_n)(a_1 b_1 \times r_1 + a_2 b_2 \times r_2) \tag{10.24}$$

With $\gamma = \sqrt{\alpha^2 + \beta^2}$ the two equations giving the optimal rotation quaternion q_{opt} can be seen in 10.4.

$$q_{opt} = \begin{cases} \frac{1}{2\sqrt{\gamma(\gamma+\alpha)(1+b_n*r_n)}} \begin{bmatrix} (\gamma+\alpha)(b_n \times r_n) + \beta(b_n + r_n) \\ (\gamma+\alpha)(1 + b_n * r_n) \end{bmatrix} & \text{for } \alpha \geq 0 \\ \frac{1}{2\sqrt{\gamma(\gamma-\alpha)(1+b_n*r_n)}} \begin{bmatrix} \beta(b_n \times r_n) + (\gamma-\alpha)(b_n + r_n) \\ \beta(1 + b_n * r_n) \end{bmatrix} & \text{for } \alpha \leq 0 \end{cases}$$

The two weighting factors a_1 and a_2 are determined a priori based on the inverse variances of the random errors connected to the measurements. (Markley, 2002).

10.5   Accuracy

One of the factors for choosing the most suitable algorithm for the purpose of the attitude determination is the accuracy. In this case the accuracy will not just be seen as under theoretical and ideal circumstances, as this just would result in a attitude determination with a perfect performance. Under ideal circumstances with no errors or disturbances in the measured vectors all algorithms will run with an accuracy which is far sufficient.

Instead the realistic circumstances will be taken into account when evaluating the accuracy of the different algorithms. This means including errors and deviations which will occur when an attitude is found, based on ideal vectors and vector measurements, which include disturbances and inaccuracies. In this way the term accuracy also will give an overview over the robustness of the algorithm; how it will tackle unprecise or faulty vector measurements to give a reasonable output.

A description of this can also be seen from figure 10.2.
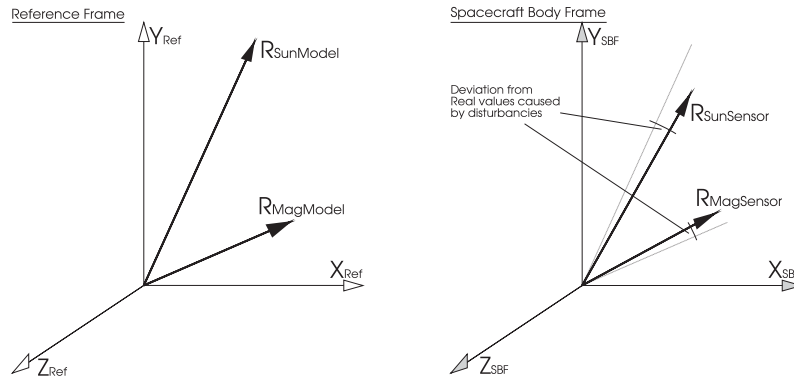

Figure 10.2: Disturbances in the vector measurements will result in vector pairs, that are different in both coordinate frames (SCB-frame and Reference frame). Hereby an error is introduced into the attitude determination, which effect will depend on the behavior of the algorithm chosen.

When introducing an error on one of two vector pairs used in the algorithm to determine the attitude, the resulting rotational matrix or quaternion will include an error which size will depend on the algorithm used.

The TRIAD algorithm is the simplest but also said to be one of the less accurate when sensor data is used, which includes disturbances. (Markley, 2002) A method to minimize this error could be to correct the sensor data before it is used to determine the attitude of the satellite, as described earlier.

The accuracy of the different algorithms, which are used to solve Wahba's Problem, was tested (Markley and Mortari, 1999) using simulated data from a star tracker scenario.

The SVD and q method are giving the truly optimal solutions as they are both based on the same well tested general matrix analysis algorithms. In this way their results are the most accurate too.

The other algorithms, QUEST, FOAM, ESOQ and ESOQ2, are less accurate as they are using characteristic polynomial equations to calculate the eigenvector, which is calculated most accurate by the q-method. In this way they can be used when the measurement noise of the vector observations is limited and well known. In case of vector measurements which are including unknown noise and disturbances the performance of the QUEST, ESOQ and ESOQ2 algorithms is rather poor, while the FOAM method is the most accurate of these four fast algorithms.

The Optimal Two Observation Quaternion Estimation Method is a relatively new alternative to the other types of algorithms to solve Wahba's Problem. Testing in Matlab using this method showed a performance very close to the performance of the optimal SVD method. Also regarding its accuracy was the error between the SVD and the Optimal Two Observation Quaternion Estimation Method less than $2E-6°$, as described in section 10.11.

10.6 Pre-Correction of Sensor Data

Instead of using the vector measurements from the sensors directly on the attitude determination and hereby introducing errors in the algorithm, another possibility would be to correct the sensor data before it is used. This could also make it possible to use less accurate and faster algorithms as the data used will not include any errors or disturbances in the first place.
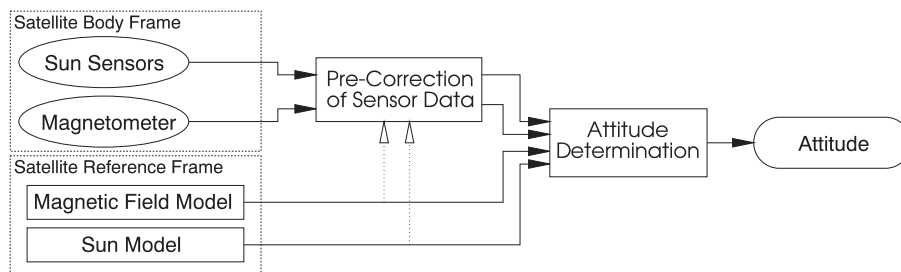
This can also be seen in figure 10.3.

Figure 10.3: The vector measurements of the magnet field and the suns direction are pre-corrected by using data from the on-board models. Hereby the inaccuracies between the modeled vectors and the measured vectors are minimized.

The benefit of pre-correcting the sensor data will be the use of a fast and simple attitude determination algorithm, while the disadvantage would be, that the pre-correction itself will cost some computational effort. However, this pre-correction may tackle the problems of disturbances in the measurements in a more case-specific and effective way.

In case of the satellites attitude determination the correction of the sensor data could be performed by using data from the on-board models, which is not frame-bound and hereby valid in any attitude. This could for example be the length of each vector and the angle between them. An option would be to correct the

measured position of the sun by using the angle between the magnetic field vector and sun vector computed by the on-board models (IGRF and Sun Model).

However, it would have to be evaluated how much computational effort this would require compared with a attitude algorithm which simply handles deviations between the vector sets as disturbances.

10.7   Speed

An important factor in the choice of the most suitable algorithm to determine the attitude are the computational requirements and the speed of the algorithm. Especially as the capabilities of the on-board computer, which is going to be used for this task, is very limited. The speed of the different algorithms are measured in flops (floating point operations).

The TRIAD algorithm determines the attitude of the satellite directly and is so far the fastest with only 118 floating point operations (Markley, 2002).

The other algorithms represent different ways of solving Wahba's Problem (Markley and Mortari, 1999). These can be split up in the slow and accurate algorithms (q-method and SVD) and the fast and less accurate algorithms (QUEST, FOAM, ESOQ and ESOQ2).

The main disadvantages of the SVD and q methods are the high computational requirements and processing times when calculating the 9 elements of the rotational matrix or the quaternion, involving an eigenvector computation. The number of floating point operations for the calculation of the rotation matrix based on two vector observations, as in case of the AAU CubeSat, lies above 650, while the q method, which in case of more than two vector observations is faster than the SVD method, requires more than 900 floating point operations.

The FOAM algorithm is significantly faster than the SVD and q method, as it requires less than 300 floating point operations. The processing requirements of the QUEST method depends on, if it uses a priori input informations or not. In case it doesn't use this information its speed is lower than the one of the FOAM algorithm and it requires less than 400 floating point operations. In the case that the a priori input data is used, the performance of the QUEST algorithm is about the same as of the ESOQ and ESOQ2; all three require less than 200 floating point operations in case of two vector observations. Some of the algorithms will produce a result which is in a matrix format. If it should be necessary to transform this rotation matrix into a quaternion, this will require 20-22 floating point operations (Markley, 2002).

Regarding the speed of the Optimal Two Observation Quaternion Estimation Method is it almost as fast as the TRIAD algorithm, as it only requires 153 or 155 floating point operations due to the fact, that it does not contain any sine or cosine operations. In this way would the TRIAD method only be 15 floating point operations faster than the Optimal Two Observation Quaternion Estimation Method if the required output is a quaternion.

10.8   Choice of Algorithm

An overview over the available algorithms to solve Wahba's Problem is visible in table 10.1. In the table 10.1 the accuracy, including the robustness, and the speed (and complexity) of the different algorithms are given. Further the output format of the different algorithms are shown (Rotation matrix or quaternion). However, all these output formats can be changed in a following computation.

The deterministic algorithm selected for the attitude determination is the Optimal Two Observation Quaternion Estimation Method. This choice was made due to the benefits of this algorithm, as its speed, the low computational requirements and the accuracy, which accordingly was tested in a simulation also by comparing it with the most optimal SVD method. Another reason for selecting this algorithm is the fact, that it is the newest one from the ones mentioned here, and therefor it would be a more interesting task of implementing it on-board the AAU CubeSat.

Algorithm	Accuracy	Speed	Output Format
TRIAD algorithm	low	Very high (<120 flops)	Rot. Matrix
q-method	High	Low (>900 flops)	Quaternion
SVD	High	Low (<650 flops)	Rot. Matrix
QUEST	Low	High (<400 flops)	Quaternion
FOAM	Medium	High (<300 flops)	Rot. Matrix
ESOQ/ESOQ1	Low	High (<400 flops)	Quaternion
ESOQ/ESOQ1 with first order update	Very Low	Very High (<130 flops)	Quaternion
ESOQ2	Low	High (<200 flops)	Quaternion
ESOQ2 with first order update	Very Low	Very High (<130 flops)	Quaternion
Opt. Two Obs. Quat. Estim. Method	High	Very High (<160 flops)	Quaternion

Table 10.1: Evaluation of different the algorithms regarding Accuracy, Speed and their output format in case of two vector observations.

10.9 Determination of Angular Velocities

The angular motion of the satellite is determined by a differentiation of the output quaternion of the deterministic attitude determination. The quaternion describing the attitude of the satellite is used to calculate the angular velocities, which are going to be used for the attitude control of the satellite.

The Euler angles around the X, Y and Z axes $\varphi = [\phi\ \theta\ \psi]^T$ are obtained from the output quaternion q by using equation 10.25.

$$\sin(\phi) = \frac{-2(q_1 q_3 - q_4 q_2)}{1} \qquad \tan(\theta) = \frac{2(q_4 q_1 + q_2 q_3)}{q_4^2 - q_1^2 - q_2^2 + q_3^2} \qquad \tan(\psi) = \frac{2(q_1 q_2 + q_4 q_3)}{q_4^2 - q_1^2 - q_2^2 - q_3^2}$$
(10.25)

Accordingly the Euler angles determined in equation 10.25 are used in equation 10.26 to determine the angular velocity of the satellite.

$$\omega(k) = \frac{\varphi(k) - \varphi(k-1)}{\Delta T}(\alpha) + \omega(k-1)(1-\alpha)$$
(10.26)

The given α is a gain value used to tune the velocity determination algorithm regarding its sensitivity. A value for α around 1 will result in a very noisy velocity determination while a low α will result in a smoother performance, as it involves the earlier velocity results and finds a mean value.

Here it shall be mentioned that the roll, pitch and yaw axes ϕ, θ and ψ are different from a traditional coordinate frame. The satellite is moving in the y-direction while the camera side, which represents the x axis of the satellite coordinate frame, points towards the earth. Accordingly the pitch of the AAU CubeSat is given by ϕ, while the roll angle is given by θ.

10.10 Problems with Collinearity

A main problem while using the deterministic attitude determination is collinearity. While using the Optimal Two Observation Quaternion Estimation Method there are two different collinearity errors, which can occur; collinearity of the magnetic field and sun vectors and collinearity of the SCB and ECI frames. A problem in all possible cases of collinearity is the fact, that there is no sufficient data to determine an attitude uniquely. This may require to use the last determined attitude as fixed value until the collinearity situation is over to avoid wrong behavior of the system. However, in some situations the collinearity effect may even cause the attitude determination algorithm not to work at all. However, it will in fact reduce the accuracy of the ADS for a short while.

10.10.1 Collinearity of Vectors

In some cases it might occur that the sun position vector is parallel with the magnetic field vector. In this case the last attitude is used until the situation is over. The benefit of this kind of collinearities is the fact, that they can be predicted in a simulation. During the satellites mission this later on will enable the ground station to plan camera missions in a way, which will avoid a case of collinearity and its effect on the pointing accuracy of the ADS. More informations about this kind of collinearity are also given in chapter E.

10.10.2 Collinearity of Coordinate Frames

In case of the Optimal Two Observation Quaternion Estimation Method a collinearity can cause a breakdown of the algorithm in a certain situation.

The different equations of this algorithm were given in section 10.4. As it is visible in these equation, a key element of this algorithm are the two vectors r_n and b_n, which are unit vectors perpendicular on the reference vector pair and measurement vector pair respectively.

These two vectors and their internal relationship play a certain role for determining the quaternion representing the attitude. This is clearly visible in section 10.4 in the equations 10.23, 10.24 and 10.4, which all include the two vectors either by using their cross product, their dot product or by adding them.

However, in a case of collinearity this may cause an error. In case of two parallel coordinate frames and an internal rotation of zero the algorithm gives as expected the correct quaternion. In case of an attitude which is collinear and pointing a $180°$ in the opposite direction of the two reference vectors, an error will occur in the algorithm. The situation for this is described in figure 10.4.
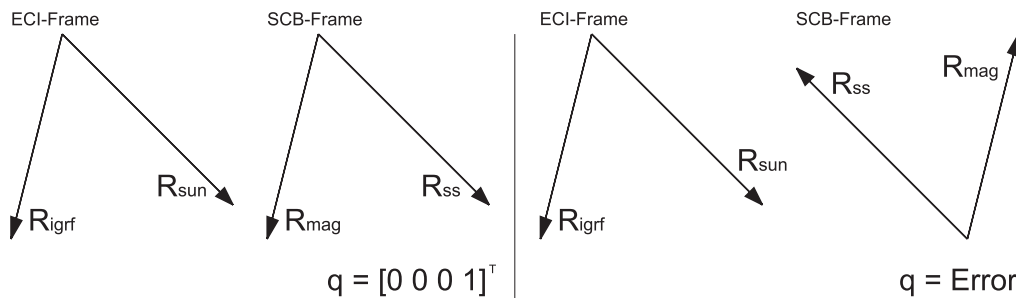

Figure 10.4: Two situations given; one with a rotation of zero, one with a 180 ° rotation, which will cause an error in the algorithm.

In this situation the two vectors r_n and b_n, given in section 10.4, will be parallel and pointing in opposite directions. Therefor their cross product will be zero, their dot product -1 and their sum will also be zero. Inserting these values in equation 10.4, this will cause a division by zero and therefor cause an error in the algorithm.

To avoid this situation it would require a filter or function which avoids values creating this collinearity error. This can be archived by using the last determined attitude and deactivate the algorithm for a short while in a similar way, as in the case of collinearity caused by the magnetic field and sun vectors.

10.11 Verification of Deterministic Algorithm

In the test specifications three simulations are described to test and validate the deterministic attitude determination. The test specifications contain the three scenarios a, b and c. In the test specification TS5.1a simulations are performed to test and validate the deterministic attitude determination. In test specifications b and c, the performance of the satellite in orbit is simulated.

Simulation scenario a

The first test is a setup of a simple functionality test. A non-collinear vector pair is set up representing the magnetic field vector and the sun vector. Accordingly changing rotation is applied to the satellite, which generates a quaternion for an attitude ranging from 0 to $360°$ around all possible axis. These attitudes in different pitch, roll and yaw axes are given with intervals of approximately $10°$. The vectors are rotated by applying the quaternion, and accordingly used together with the original fixed vectors as input for the different algorithms.

The test includes also an albedo and sun model to include the vector errors caused by Earth albedo as well as the algorithm used to calculate the sun vector based on the sensor inputs.

The quaternion determined by the Optimal Two Observation Quaternion Estimation Method is compared with the output of the rotation generator and the error is calculated in degrees. Further an attitude is determined using the SVD method. This is to verify, how close the accuracy of the chosen algorithm is to the most optimal algorithm.

The following simulations are performed to test the functionality and performance of the Optimal Two Observation Quaternion Estimation Method and to test the accuracy of the attitude determination.

Setup 1 : The algorithm is tested without albedo and albedo correction. The magnetic field error is set to zero and the gains of the sun sensor measurements and magnetometer are set to zero in the attitude determination.

Setup 2 : A constant $6.3°$error of the magnetic field vector is added, by applying a small rotation. Further the Earth albedo is added without activating the albedo correction.

Setup 3 : The gains used in the attitude determination algorithm are changed to the variances of the magnetometer error and the error given by the albedo test simulations described in chapter 8. the simulation includes the vector errors in number 2.

Setup 4 : The albedo correction is activated. Weights and errors from number 2 and 3 are also used.

In this simulation the satellite position, sun direction and direction of the magnetic field were given by:

$$R_{sat} = [1 \ 1 \ 0]^T \quad R_{sun} = [1 \ 0 \ 0]^T \quad andR_{mag} = [1 \ 1 \ 0]^T$$

The outputs given in these simulations can be seen in table 10.2. In this table the max error in the determined attitude is given as well as the RMS value. Further it is listed if the error on the magnetic field vector B_{error} was applied. The angle between the real sun vector and the vector measured by the sun sensors including albedo is given as γ_{albedo} and ranges from $18.182°$to $24.911°$. The angle between the magnetic field vector and the sun vector is constant $45°$in the ECI frame α_{ECI} and in the SCB frame α_{SCB}, where the angle between the vectors varies between $62.55°$and $69.25°$.

Simulation	Max Error	RMS Error	B_{error}	$\gamma_{albedo(RMS)}$	α_{ECI}	$\alpha_{SCB(RMS)}$
Setup 1	$2.09E{-}6°$	$5.65E{-}7°$	0	0	$45°$	$45°$
Setup 2	$12.77°$	$11.5°$	$0.63°$	$22.35°$	$45°$	$66.62°$
Setup 3	$2.563°$	$1.879°$	$0.63°$	$22.35°$	$45°$	$66.62°$
Setup 4	$2.086°$	$1.203°$	$0.63°$	$22.35°$	$45°$	$66.62°$

Table 10.2: Errors of the deterministic algorithm.

In this simulation it has been shown, that the maximum angular errors are approximately $2.1°$. Angular errors on the sun vector were reduced considerably by weighting the vector inputs. Also the albedo correction had an effect of reducing errors.

The difference between the SVD method and *The Optimal Two Observation Quaternion Estimation Method* showed to be below $2E{-}6°$. In other simulations in different orbital positions and angles between sun and magnetic field vector the error of the ADS showed to be smaller or corresponding to the given example.

This test has illustrated that it is possible at a given position to use the *The Optimal Two Observation Quaternion Estimation Method* for determining the attitude of the satellite regardless its attitude.

Simulation scenario b

The second simulation of the deterministic attitude determination is performed according to test specification TS5.1b. It describes a simulation of the satellite in orbit without albedo or albedo correction. In the simulation the angular velocities and the rotation quaternion shall be determined. The Simulink model in figure 10.5 is used for this simulation.
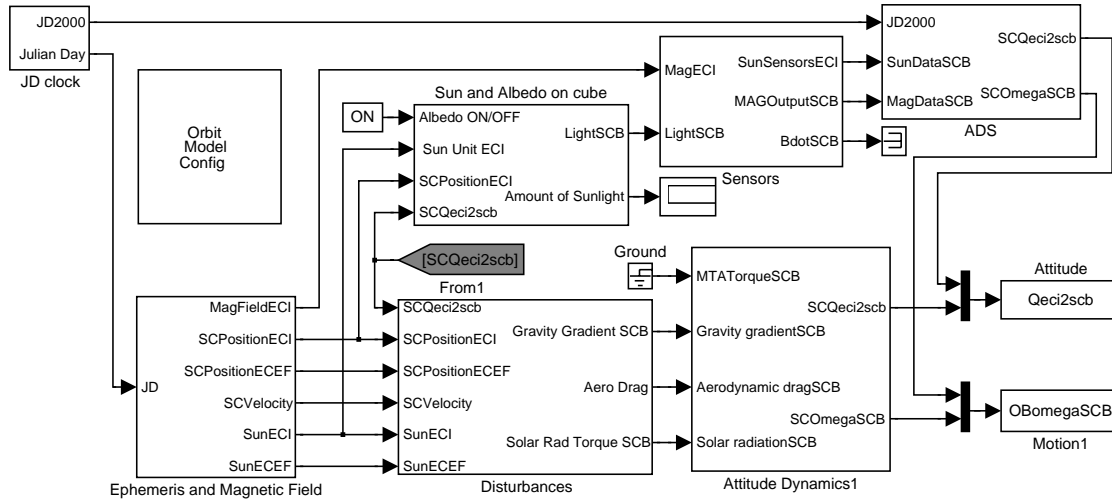
Figure 10.5: The Simulink model used for test scenarios *b* and *c*

In the simulation truth models are used for simulating orbit, magnetic field and sun model in the block *Ephemeris and magnetic field*.
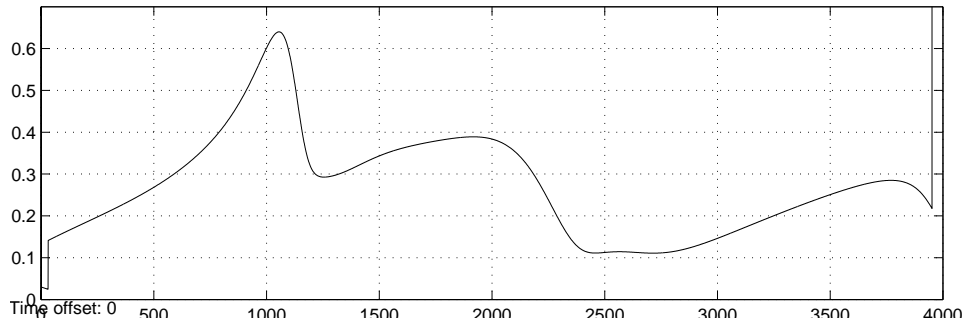

Figure 10.6: The error in the attitude determination of simulation scenario *b* given in degrees.

In the plot shown in figure 10.7 around the positions 1050 and 1250 there are major changes on the velocity determination visible. This is due to the fact, that the accuracy of the determined attitude changed violently in the same positions as visible in figure 10.6. This increased accuracy is interpret by the velocity determination algorithm as a change of the attitude and hereby an according motion is calculated, resulting in an increase of the velocity determination error.

The determined angular velocities given as roll, pitch and yaw are shown on figure 10.7 together with the plot of the according real values of the angular velocities.
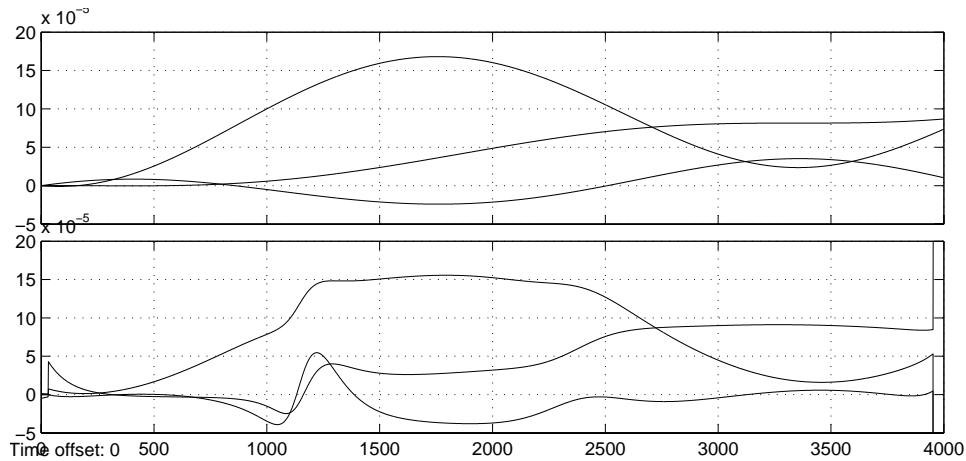
Figure 10.7: The angular velocities ϕ, θ and ψ given as reference (top) and determined by the ADS (bottom) during scenario *b*.

Here a major error is clearly visible in the determination of the angular velocities. This is due to the fluctuations in the accuracy of the determined attitude shown in figure 10.6. When comparing figure 10.7 with figure 10.6 this is clearly visible. These fluctuations caused by noise in the sensors, are having a larger impact on the velocity determination as it is more sensitive to these errors.

Regarding the possibility of collinearities it was concluded, that non occurred during the simulation.

Simulation scenario c

The test performed according to *c* in the test specifications TS5.1a consists the simulation used in test *b* with the Earth albedo and an albedo correction added to the system.

The error of the determined attitude has been increased compared with the results of the test performed in simulation scenario *b*, and is shown in figure 10.8. The accuracy of the attitude determination is below
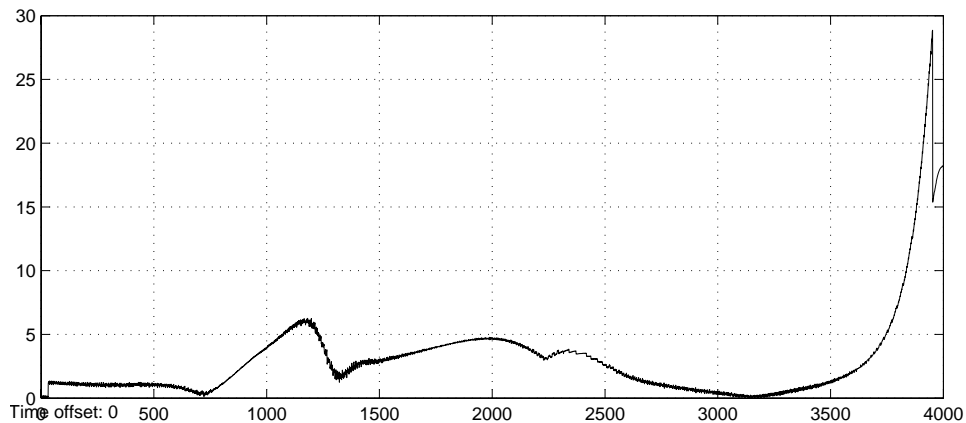

Figure 10.8: The error in degrees between the real attitude of the satellite and the estimated attitude during simulation scenario *c*. It is taken over an interval of sun light between two eclipses, which are visible as changes in the performance in both outer sides of the plots.

$6.26°$ during most of the orbit in sunlight. Only just before the eclipse the error in the attitude rises due

to the missing albedo light and the still activated albedo correction. This has been described earlier in the chapter 8 and is caused by the albedo correction algorithm.

This accuracy still leaves some space to fulfill the main requirement S5.1 regarding a complete pointing accuracy of the ADCS below $8°$.

Also during this simulation no collinearities occurred either between the sun vector and magnetic field, nor did a collinearity of the coordinate frames occur as described in section 10.10. However, further simulations will be required to ensure it will not create any major problems.

10.11.1 Discussion of Results

Based on the simulations it can be concluded that the deterministic attitude determination is capable of determining the attitude of the satellite with an accuracy of less than $8°$. However, the simulation only showed a minor part of the satellite orbit and more simulations over longer intervals are required to ensure that the requirements regarding the pointing accuracy of $8°$ can be fulfilled.

The simulations also showed that a much better velocity determination algorithm is necessary. This is due to the much unprecise results of the determination of the angular velocity in test setup c. The current algorithm used and described in equation 10.26 might not be suitable for the high level of disturbances present in the measurements. An alternative option might be to determine the angular velocities mainly based on the magnetic field vector, as these measurements contain the smallest error compared to the sun sensors.

10.12 Summary

For the development of a deterministic attitude determination several possible algorithms were available, including the simple TRIAD algorithm and several methods of solving Wahba's problem. Base on the accuracies, complexities and speeds of the different algorithms, the Optimal Two Observation Quaternion Estimation Method was chosen as algorithm to be used on-board the satellite and implemented in a simulation of the attitude determination system.

Several simulations were performed to verify the reliability and accuracy of the algorithm and its ability to determine an attitude quaternion. These tests showed the algorithm to be suitable for the task.

A simple rotational velocity determination was implemented based on the differentiation of the determined attitude quaternions. However, these calculated velocities showed to be unprecise in situations without any disturbances, and not useful at all when disturbances were included in the simulations.

A simulation including all disturbances and elements of the ADS showed to result in an accuracy below the $8°$ as set up in requirement S5.1. However, further simulations of the ADS and the entire ADCS are necessary to ensure the performance of the system to lie within the required limits of accuracy and performance.

chapter 11

Extended Kalman filter

In this chapter an attitude determination solution using the extended Kalman filter is presented. First the operation of the extended Kalman filter is outlined. In section 11.2 the dynamic equations for the satellite are described. The matrices and vectors of the state model to be used in the extended Kalman filter are described in section 11.3. At the end of the chapter, simulation results are presented for the filter.

11.1   Operation of extended Kalman filter

The extended Kalman filter consists of the three phases: *Initialization*, *Prediction* and *Filtering*. In *initialization* the initial values for the state estimate and the error covariance are set. Then the *Prediction* and *Filtering* are repeatedly performed. The *Prediction* makes an a priori update of the state and covariance matrice. The measured sensor data is used for updating the a priori value to determine the a posteriori state vector. In figure 11.1 the operation of the Kalman filter is illustrated.
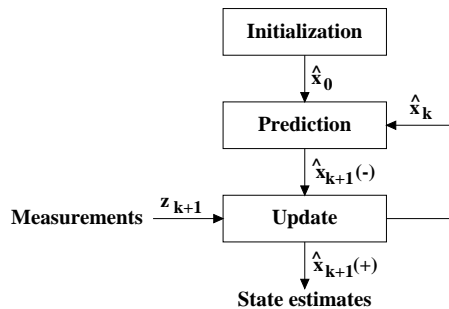

Figure 11.1: An a priori estimate of the state $\hat{x}_{k+1}(-)$ is updated using measurements z_{k+1} to obtain the a posteriori state estimate $\hat{x}_{k+1}(+)$.

In (Humphreys, 2002) the extended Kalman filter has been used for attitude determination on-board the Utah State University's satellite USUSAT. The extended Kalman filter in USUSAT uses magnetometer and solar panel data and is in that way very similar to this case. In (Humphreys, 2002) the estimated states include an attitude quaternion, angular velocity and disturbance torques. For the AAU CubeSat the state vector will include the attitude quaternion and angular velocity. A difference from the procedure in (Humphreys, 2002) is, that instead of estimating the disturbance torques as states, the input control torques generated with the magnetorquers are modeled as inputs.

Quaternions are used for describing the orientation of the satellite. In appendix C some general quaternion rules are described, which are used on the following sections.

11.2 Attitude dynamics equations

The dynamic equations of motion for a rigid body satellite describe the relationship between external torques n_{ext} acting on the spacecraft and the change of angular momentum L_{eci} in the inertial frame and the angular momentum L_{scp} in the spacecraft principal axis frame. In equation 11.1 $[\omega \times]$ is the cross product matrix (see appendix C) of the angular velocity ω of the SpaceCraft Principal axes (SCP) frame with respect to the ECI frame.

$$\left(\frac{dL}{dt}\right) = -[\omega \times]L_{scp} + n_{ext} \tag{11.1}$$

From rewriting equation 11.1 an expression for the time derivative of angular velocity is expressed as in equation 11.2:

$$\dot{\omega} = J^{-1}(-[\omega \times]J\omega + n_{ctrl} + n_d) \tag{11.2}$$

The external moments have been broken into control and disturbance components $n_{ext} = n_{ctrl} + n_d$. The 3×3 inertia matrix J is the diagonal inertial matrix defined in the SCP frame.

11.3 Extended Kalman filter

The system can be represented by a nonlinear continuous model and a nonlinear discrete measurement model in equations 11.3 and 11.4, respectively. In equation 11.3 the variable $x(t)$ is the state, $u(t)$ is an input to the system and $w(t)$ is zero-mean white process noise. In equation 11.4 the measurement vector z_k is related to the state vector x_k by the nonlinear function $h(k)$ and corrupted by uncorrelated and zero-mean measurement noise v_k.

$$\dot{x}(t) = f(x(t), u(t), t) + w(t) \tag{11.3}$$

$$z_k = h(x_k) + v_k \tag{11.4}$$

The process noise $w(t)$ is described by equation 11.5 where $Q(t)$ is the strength of process noise. The discrete noise v_k has the covariance described by equation 11.6, with R_k representing the measurement noise covariance matrix.

$$E[w(t)w^T(t')] = Q(t)\delta(t - t') \tag{11.5}$$

$$E[v_k v_s{}^T] = R_k \delta_{k,s} \tag{11.6}$$

The extended Kalman filter linearizes the nonlinear functions $f(x, u, t)$ and $h(x)$, *on the fly*, about the estimated trajectory. In equations 11.7 Δx_k is the difference between the true state x_k and the estimated state $\hat{x}_k$, and Δz_k is the innovation of the output vector, as defined in equation 11.7.

$$\Delta x = x - \hat{x}, \qquad \Delta z = z - \hat{z} = z_k - h(\hat{x}_k) \tag{11.7}$$

The discrete linear state space models in equation 11.8 and 11.9 are represented with equations 11.7.

$$\Delta x_{k+1} = \Phi_k \Delta x_k + G_k u_k + w_k \tag{11.8}$$

$$\Delta z_k = H_k \Delta x_k + v_k \tag{11.9}$$

The matrix Φ is the state transition matrix for propagating the Ricatti equations. Φ is approximated using the first few terms of the Taylor series expansion of e^{FT_s}, where T is the sampling time:

$$\Phi_k \approx I + FT_s \tag{11.10}$$

The linearized matrices F, G and H are found using first order linear approximations:

$$F(t) = \left.\frac{\partial f(x, u, t)}{\partial x}\right|_{x=\hat{x}} \qquad G(t) = \left.\frac{\partial f(x, u, t)}{\partial u}\right|_{x=\hat{x}} \qquad H_k = \left.\frac{\partial h(x)}{\partial x}\right|_{x=\hat{x}} \tag{11.11}$$

In order to use the formulation of the extended Kalman filter above, the state vector and matrices F, G and H must be defined for the satellite.

11.3.1 State vector

The states to be estimated are the attitude quaternion $\bar{q}$ and the angular velocity ω.

$$x = \begin{bmatrix} \bar{q} \\ \omega \end{bmatrix} \tag{11.12}$$

The quaternion $\bar{q}$ represents a rotation of the ECI frame with respect to the SCP frame. The angular velocity ω is the rotation rate of the SCP with respect to the ECI frame. The standard state vector is reduced to the body-referenced state vector in equation 11.13. The 4×1 attitude quaternion $\bar{q}$ is replaced with the 3×1 vector component of the error quaternion δq.

$$\tilde{x} = \begin{bmatrix} \delta q \\ \Delta \omega \end{bmatrix} \tag{11.13}$$

The reduced state vector is introduced in order to represent the state without the quaternion redundancy (Humphreys, 2002) (Bak, 1999). The error quaternion $\delta\bar{q}$ is the rotation between the true quaternion $\bar{q}$ and the estimated quaternion $\hat{\bar{q}}$, as defined in equation 11.14. When this rotation is small it can be assumed that the real part of the quaternion error $\hat{\bar{q}}$ is close to 1, while information is contained in the complex part. This assumption can be violated during initial convergence, where the error quaternion $\delta\bar{q}$ may be large.

$$\bar{q} = \delta\bar{q} \otimes \hat{\bar{q}} \tag{11.14}$$

Using the state vector defined in equation 11.13 together with the equations 11.8 and 11.9 means that the attitude quaternion $\hat{q}$ and the angular rate $\hat{\omega}$ are not estimated directly in the extended Kalman filter. Instead $\delta\hat{q}$ and $\Delta\hat{\omega}$ are estimated. The a posteriori angular rate $\hat{\omega}_{k+1}(+)$ can be estimated using equation 11.15.

$$\hat{\omega}_k(+) = \hat{\omega}_k(-) + \Delta\hat{\omega}_k(+) \tag{11.15}$$

The quaternion may be updated using equation 11.16 (Humphreys, 2002) (Bak, 1999). During initial convergence a violation may occur of the small angle assumption introduced in equation 11.13. This happens when the root in equation 11.16 becomes negative. When this condition is detected, equation 11.17 can be used (Humphreys, 2002).

$$\hat{\bar{q}}_{k+1}(+) = \frac{\delta\hat{\bar{q}}_{k+1}(+)}{\sqrt{1 - ||\delta\hat{q}_{k+1}(+)||^2}} \otimes \hat{\bar{q}}_{k+1}(-) \tag{11.16}$$

$$\hat{\bar{q}}_{k+1}(+) = \frac{1}{\sqrt{1 + ||\delta\hat{q}_{k+1}(+)||^2}} \begin{bmatrix} \delta\hat{\bar{q}}_{k+1}(+) \\ 1 \end{bmatrix} \tag{11.17}$$

In *primary operation*, as defined in section 3.5, the deterministic solution, described in chapter 10, will be used to re-initialize the filter, if the extended Kalman filter does not converge for some predetermined time.

11.3.2   Control input vector

The control input torque n_{ctrl} is generated by the use of magnetorquers. The magnetorquers are placed perpendicular to the x, y and z axes of the SCB frame. The torques generated with the magnetorquers are given in the SCB frame. They are generated by the interaction of the geomagnetic field B and the magnetic moment generated with the currents through the coils, as described in equation 11.18:

$$n_{ctrl} = \bar{m} \times B^{scb} = d(nA\bar{I}^{scb}) \times B^{scb},$$ (11.18)

where d is the duty cycle of the control signal, n is the number of turns in each coil, A is the square area of the coil, and $\bar{I}^{scb}$ is a 3×1 vector with the measured current through each coil. The magnetic field vector B^{scb}, used for determining the control input torques, is the magnetic field measured with the magnetometer.

The input vector $u(t)$ is of dimension 3×1 and consist of the control torques n_{ctrl} rotated to the SCP frame.

$$u = \begin{bmatrix} n_{ctrl}^{scp} \end{bmatrix}$$ (11.19)

11.3.3   Measurement vector

Before using the sensor measurements in the extended Kalman filter, data is processed to create a magnetic field vector and a sun vector, as illustrated in section 3.5. The 3×1 measured sun vector s^{scb} together with the 3×1 measured magnetic field vector b^{scb} are used for constructing the measurement vector z_k.

The sensitivities of the magnetometer sensors differ widely for the HMC1001/2 sensors from Honeywell. This means that either a precise sensitivity of the sensors should be determined, by using another magnetometer with known sensitivity as reference, or that the magnetic field vectors in ECI and SCB should be made into unit vectors. By making unit vectors the problem of determining a precise sensitivity is avoided. Both the sun vector and magnetic field vector are made into unit vectors. This gives consistency with the deterministic method, which only accepts unit vectors as inputs.

The measurement vector is given in the SCB frame.

$$z_k = \begin{bmatrix} b^{scb} \\ s^{scb} \end{bmatrix}$$ (11.20)

11.3.4   State transition matrix

The state transition matrix Φ is given in equation 11.10 and requires the F matrix. The F matrix is divided into F_1 and F_2 for the quaternion update and the angular velocity update, respectively.

$$F = \begin{bmatrix} F_1 \\ F_2 \end{bmatrix}$$ (11.21)

The matrix F_1 is derived in appendix C:

$$F_1 = \begin{bmatrix} -[\hat{\omega}\times] | \frac{1}{2}I_{3\times3} \end{bmatrix} = \begin{bmatrix} 0 & -\hat{\omega}_3 & \hat{\omega}_2 & \frac{1}{2} & 0 & 0 \\ \hat{\omega}_3 & 0 & -\hat{\omega}_1 & 0 & \frac{1}{2} & 0 \\ -\hat{\omega}_2 & \hat{\omega}_1 & 0 & 0 & 0 & \frac{1}{2} \end{bmatrix}$$ (11.22)

The matrix F_2 is derived by using equation 11.2:

$$f_2(\tilde{x}) = \dot{\omega} = J^{-1}(-[\omega\times]J\omega + n_{ctrl} + n_d)$$ (11.23)

and noticing that linearization of $f_2(\tilde{x})$ about the estimated state by using equation 11.11, results in:

$$F_2 = \begin{bmatrix} 0_{3\times3} | \Theta(\hat{\omega}) \end{bmatrix} = \begin{bmatrix} 0 & 0 & 0 & 0 & \frac{\hat{\omega}_3(J_{yy}-J_{zz})}{J_{xx}} & \frac{\hat{\omega}_2(J_{yy}-J_{zz})}{J_{xx}} \\ 0 & 0 & 0 & \frac{\hat{\omega}_3(J_{zz}-J_{xx})}{J_{yy}} & 0 & \frac{\hat{\omega}_1(J_{zz}-J_{xx})}{J_{yy}} \\ 0 & 0 & 0 & \frac{\hat{\omega}_2(J_{xx}-J_{yy})}{J_{zz}} & \frac{\hat{\omega}_1(J_{xx}-J_{yy})}{J_{zz}} & 0 \end{bmatrix}$$ (11.24)

Using equation 11.10 the state transition matrix can be written as in equation 11.25. The sampling interval T_s is set to 1 second and is left out from the equation. The principal moments of inertia are given in chapter 6.

$$\Phi = I + FT_s = \begin{bmatrix} 1 & -\hat{\omega}_3 & \hat{\omega}_2 & \frac{1}{2} & 0 & 0 \\ \hat{\omega}_3 & 1 & -\hat{\omega}_1 & 0 & \frac{1}{2} & 0 \\ -\hat{\omega}_2 & \hat{\omega}_1 & 1 & 0 & 0 & \frac{1}{2} \\ 0 & 0 & 0 & 1 & \frac{\hat{\omega}_3(J_{yy}-J_{zz})}{J_{xx}} & \frac{\hat{\omega}_2(J_{yy}-J_{zz})}{J_{xx}} \\ 0 & 0 & 0 & \frac{\hat{\omega}_3(J_{zz}-J_{xx})}{J_{yy}} & 1 & \frac{\hat{\omega}_1(J_{zz}-J_{xx})}{J_{yy}} \\ 0 & 0 & 0 & \frac{\hat{\omega}_2(J_{xx}-J_{yy})}{J_{zz}} & \frac{\hat{\omega}_1(J_{xx}-J_{yy})}{J_{zz}} & 1 \end{bmatrix} \quad (11.25)$$

11.3.5 Process noise coupling

The input matrix G is determined by differentiation of equation 11.2 with respect to the control torque n_{ctrl}. With the input vector $u(t)$ as defined in section 11.3.2 the linearization of process noise coupling matrix G is defined as in equation 11.26. The control input torques n_{ctrl} are given in the SCB frame and are rotated to the SCP frame.

$$G = \begin{bmatrix} 0_{3\times3} \\ J^{-1}A_{scb}^{scp} \end{bmatrix} = \begin{bmatrix} 0 & 0 & 0 \\ 0 & 0 & 0 \\ 0 & 0 & 0 \\ \frac{1}{J_{xx}} & 0 & 0 \\ 0 & \frac{1}{J_{yy}} & 0 \\ 0 & 0 & \frac{1}{J_{zz}} \end{bmatrix} \quad (11.26)$$

11.3.6 Measurement sensitivity matrix

The measurement vector defined in section 11.3.3 provide a magnetic field vector and a sun vector both defined in the SCB frame. Equation 11.27 is the measurement vector estimate $\hat{z}_k$, using the magnetic field vector and sun vector estimated with on-board reference models.

$$\hat{z}_k = h(\tilde{x}_k) + v_k = \begin{bmatrix} A_{scp}^{scb} A(\bar{q})b^{eci} \\ A_{scp}^{scb} A(\bar{q})s^{eci} \end{bmatrix} + v_k, \quad (11.27)$$

First the magnetic field vector and sun vector is rotated from the ECI frame to the SCP frame. This is done with the rotation matrix $A(\bar{q})$ using the latest a priori estimate of the attitude quaternion. Then a rotation A_{scp}^{scb} from the SCP frame to the SCB frame is needed, because the sensor measurements are performed in the SCB frame. The rotation $A(\bar{q})$ can be rewritten as the product of factors:

$$A(\bar{q}) = A(\delta\bar{q})A(\hat{\bar{q}}) \approx (I_{3\times3} - 2[\delta q\times])A(\hat{\bar{q}}) \quad (11.28)$$

The estimated magnetic field and sun vectors may be rotated into the SCP frame:

$$\hat{b}_{scb}^k = A_{scb}^{scp} A(\hat{\bar{q}})b_k^{eci} \qquad \hat{s}_{scb}^k = A(\hat{\bar{q}})s_k^{eci} \quad (11.29)$$

Using equation 11.28 the measurement sensitivity matrix H is determined as equation 11.30.

$$H_k = \frac{\partial h(\tilde{x})}{\partial \tilde{x}}\Big|_{\bar{x}=\hat{\bar{x}}_k} = 2 \begin{bmatrix} [\hat{b}_k^{scb}\times] & 0_{3\times3} \\ [\hat{s}_k^{scb}\times] & 0_{3\times3} \end{bmatrix} = 2 \begin{bmatrix} 0 & -\hat{b}_3^{scb} & \hat{b}_2^{scb} & 0 & 0 & 0 \\ \hat{b}_3^{scb} & 0 & -\hat{b}_1^{scb} & 0 & 0 & 0 \\ -\hat{b}_2^{scb} & \hat{b}_1^{scb} & 0 & 0 & 0 & 0 \\ 0 & -\hat{s}_3^{scb} & \hat{s}_2^{scb} & 0 & 0 & 0 \\ \hat{s}_3^{scb} & 0 & -\hat{s}_1^{scb} & 0 & 0 & 0 \\ -\hat{s}_2^{scb} & \hat{s}_1^{scb} & 0 & 0 & 0 & 0 \end{bmatrix} \quad (11.30)$$

11.3.7 Process noise covariance

The Q_k matrix is a 6×6 diagonal matrix. In the Q matrix the diagonal elements are given the following values: The part corresponding to the quaternion are set to 1E-9 and the remaining three values corresponding to angular velocity are set to 1E-6. These values will be optimized by tuning the parameters, when simulating the system in Matlab.

$$
Q_k = \begin{bmatrix}
1\mathrm{E}{-}9 & 0 & 0 & 0 & 0 & 0 \\
0 & 1\mathrm{E}{-}9 & 0 & 0 & 0 & 0 \\
0 & 0 & 1\mathrm{E}{-}9 & 0 & 0 & 0 \\
0 & 0 & 0 & 1\mathrm{E}{-}6 & 0 & 0 \\
0 & 0 & 0 & 0 & 1\mathrm{E}{-}6 & 0 \\
0 & 0 & 0 & 0 & 0 & 1\mathrm{E}{-}6
\end{bmatrix}
\tag{11.31}
$$

11.3.8 Measurement noise covariance

The measurement noise covariance matrix R is a 6×6 diagonal matrix. The diagonal elements of the matrix R are chosen to reflect measurement errors of magnetometer and sun sensors.

$$
R = \begin{bmatrix}
\sigma_b{}^2 & 0 & 0 & 0 & 0 & 0 \\
0 & \sigma_b{}^2 & 0 & 0 & 0 & 0 \\
0 & 0 & \sigma_b{}^2 & 0 & 0 & 0 \\
0 & 0 & 0 & \sigma_s{}^2 & 0 & 0 \\
0 & 0 & 0 & 0 & \sigma_s{}^2 & 0 \\
0 & 0 & 0 & 0 & 0 & \sigma_s{}^2
\end{bmatrix}
\tag{11.32}
$$

The first three elements in the diagonal of R are the covariance of errors related to magnetic field measurement and the last three elements are the covariance of the sun sensor errors. All vectors are normalized before they are used in the extended Kalman filter. and in section 9.2.2 the angular error between measured magnetic field is determined to be $0.63°$. This angular error results in:

$$
\sigma_b = \arctan(0.63°) = 0.010995
$$

In section 8.2.2 the variance of the unitized sun vector is found.

$$
\sigma_b{}^2 = 0.00012 \qquad \sigma_s{}^2 = 0.0021
\tag{11.33}
$$

11.4 Simulation results

The simulations of the extended Kalman filter were implemented in a Matlab script and tested according to the test specifications TS5.3a to TS5.3d.

11.4.1 Input data for test of extended Kalman filter

The true satellite attitude and angular velocity is simulated using a dynamic model for the satellite and disturbances from gravity gradient and solar radiation.
For the simulations The following initial attitude quaternion and velocities were used:

$$
\text{pitch} = -92.5323° \qquad \text{roll} = 62.4781° \qquad \text{yaw} = -15.8966°
\tag{11.34}
$$

$$
\omega_1 = 1/7000 \, rad/sec \qquad \omega_2 = 1/6000 \, rad/sec \qquad \omega_3 = 1/5000 \, rad/sec
\tag{11.35}
$$

	Start time	12.45 the 21st of June, year 2003
	Simulation time	9000 seconds
	Orbit	
Truth models	Magnetic field model	IGRF2000 order 10
	Sun model	
	SGP4	
	Albedo	0.35 of solar flux
	Disturbances	Gravity gradient and Solar radiation
	Attitude dynamics	Principal moment of inertia (section 6)
	Input torques	None
On-board algorithms	Magnetic field model	IGRF2000 order 4
	Sun model	
	Albedo correction	
	Orbit model	according to section 7
	Extended Kalman filter	

Table 11.1: Conditions used for simulating extended Kalman filter in Scenarios a to e

11.4.2 Simulation scenario a

In *scenario a* the extended Kalman filter is tested according to test specification TS5.3a. Sun sensor and magnetometer data is used throughout the entire simulation. In figure 11.2a the true attitude and the estimated attitude are represented as pitch, roll and yaw angles and in figure 11.2b the estimation error is plotted. The filter converges within 700 seconds, but as can be seen in figure 11.2b, large angular errors appear on all axes. After convergence errors as large as up to 17° occurs.
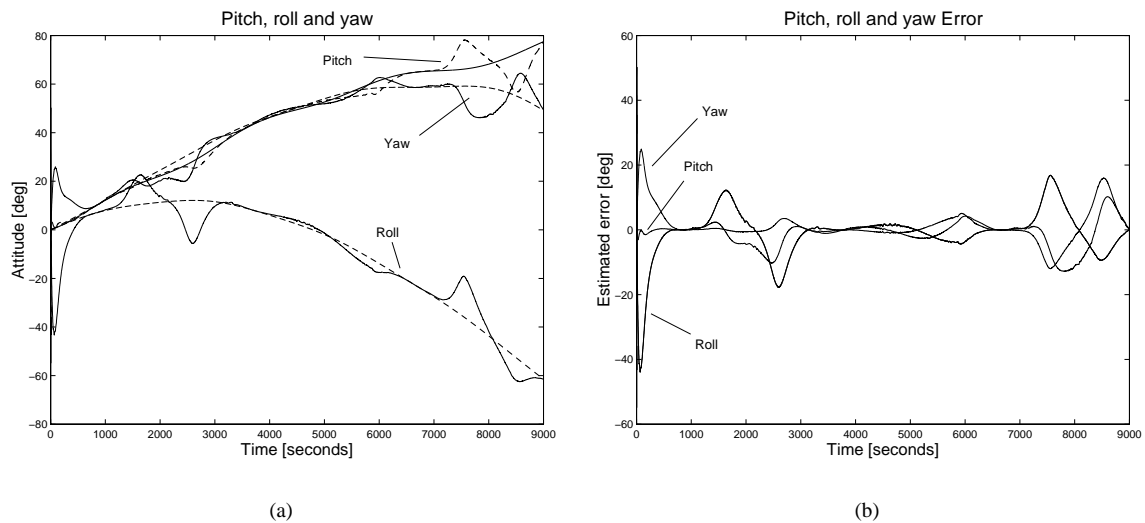
Figure 11.2: Left plot: Dashed lines are estimated attitudes and full lines are true attitudes. Right plot: Estimation errors for attitude.

The true and the estimated angular velocities are plotted in figure 11.3a. The angular velocity errors of angular velocities are plotted in figure 11.3b. As can be seen large errors up to 1E-3 radians per second are present.
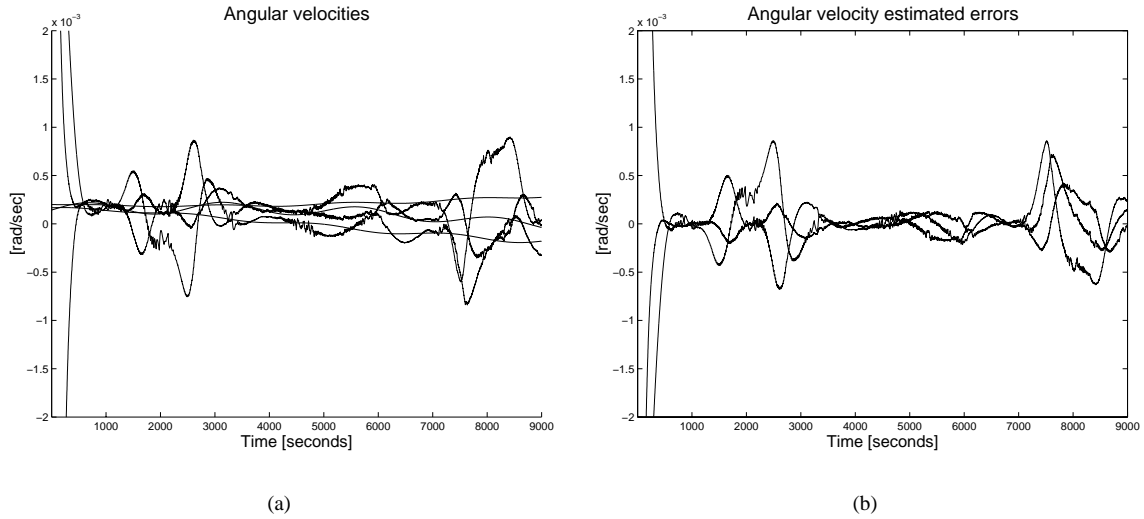
Figure 11.3: Left plot: Dashed lines are estimated angular velocities and full lines are true angular velocities. Right plot: Estimation errors for angular velocities.

The estimation errors of *scenario a* for attitudes and angular velocities are caused by the inaccuracy of the sun sensors. This is illustrated in simulation *scenario b*, where only magnetometer data is used.

11.4.3   Simulation scenario b

This simulation was performed similar to *scenario a*, except that the measured and estimated sun vectors are set to zero. Using only magnetometer data reduced the errors significantly. True and estimated attitudes are presented in figure 11.4a. Here it can be seen that the time it takes for the filter to converge, without the sun sensor data, has increased to approximately 5000 seconds. It can be seen in figure 11.4b, that after the attitude has converged, pitch, roll and yaw vary approximately $\pm 2\,^{\circ}$.

As can be seen in figure 11.5a and b, the time it takes to converge has increased to approximately 4000 seconds. Similar to the estimation errors for attitudes, the estimation errors for angular velocities are greatly reduced once the state has converged. Maximum errors after 4000 seconds are approximately 8E-4 radians per second. In the time range 3500 to 7000 seconds, errors are less than 2E-4 radians per second.

11.4.4   Simulation scenario c

This simulation was performed similar to simulation scenario b with the one difference that the initial attitude was found using the deterministic attitude determination, presented in chapter 10. The true and estimated attitudes represented as pitch, roll and yaw are plotted in figure 11.6a. The filter converges within the first 1000 seconds and the maximum error is approximately $15\,^{\circ}$. After the filter has converged the error varies within $\pm 2.5\,^{\circ}$ in figure 11.6b.
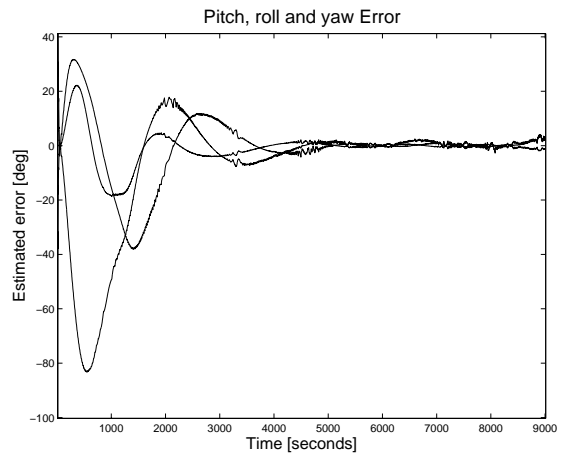
Estimated angular velocities also converge fast. However, in the plots in figure 11.7

The process noise matrix Q and initial values for the covariance matrix were tuned to give the simulated results in scenario a, b and c. New values used for the process noise matrix are 1E-14 and initial values of the error covariance matrix are 1E-1.

In figure 11.8 the pitch, roll and yaw are plotted with the standard deviation bounds (σ 2). Standard deviation bounds are calculated as two times the square roots of the covariance matrix diagonal elements. If the filter is correctly tuned state errors should lie within these bounds.
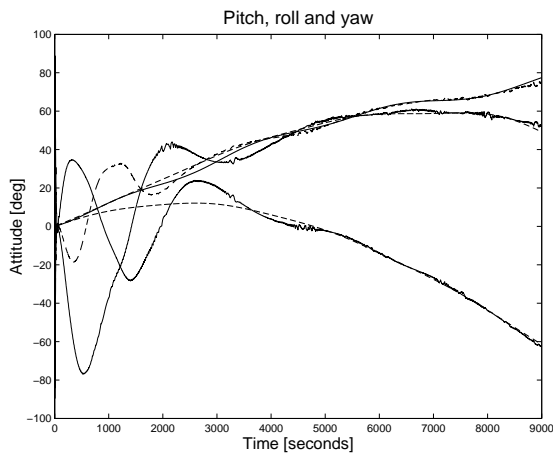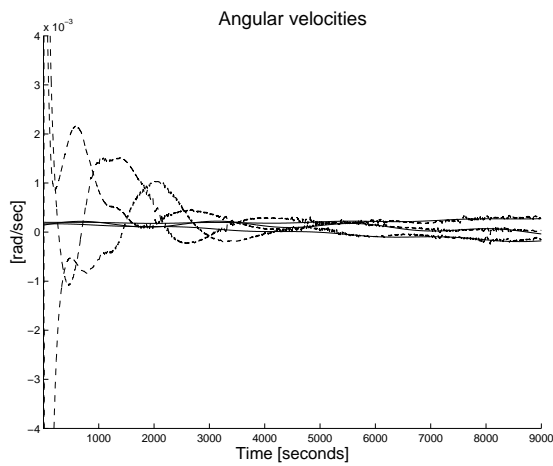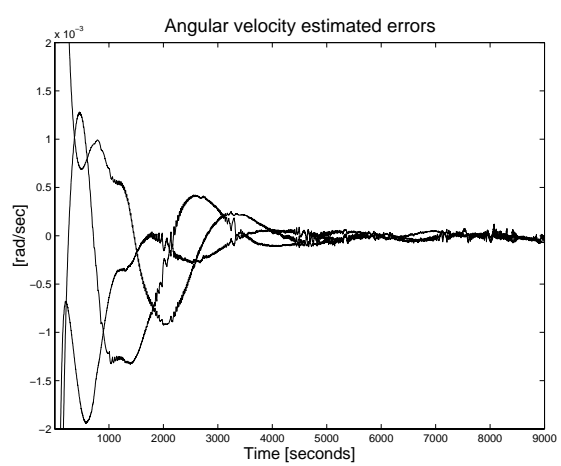
Figure 11.4: Left plot: Dashed lines are estimated attitude and full lines are true attitudes. Right plot: Estimation errors for attitude.
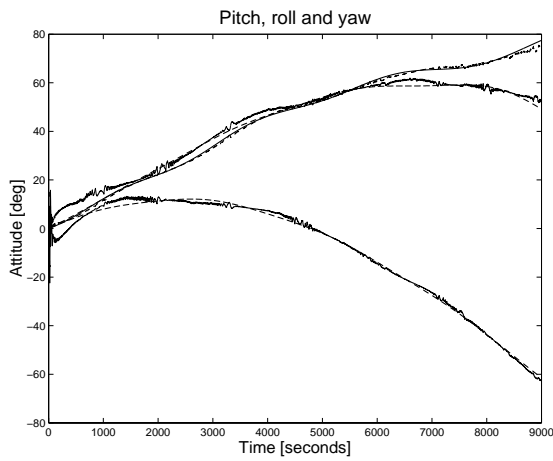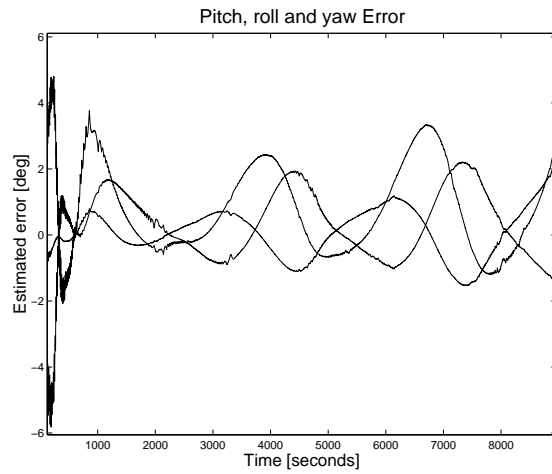

Figure 11.5: Left plot: Dashed lines are estimated angular velocities and full line is true angular velocities. Right plot: Estimation errors for angular velocities.
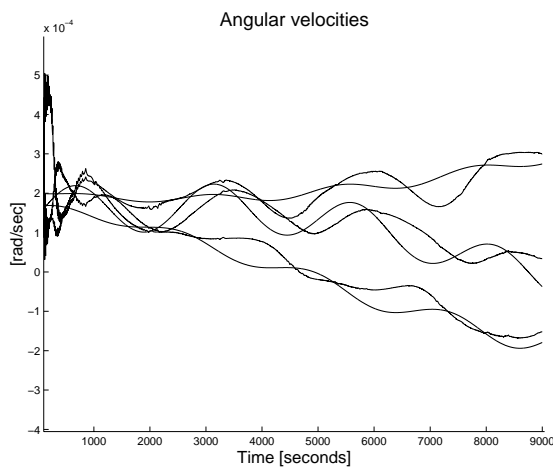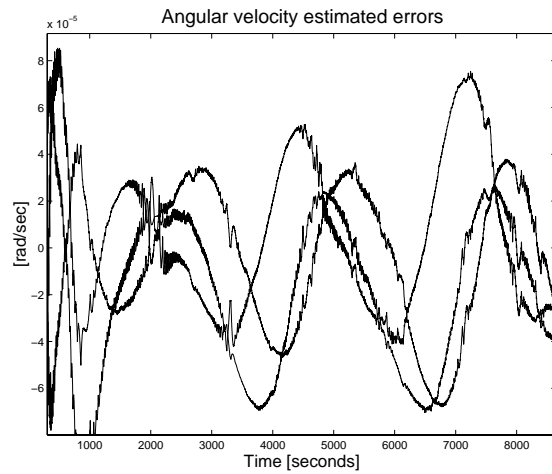
Figure 11.6: Left plot: Dashed lines are estimated attitude and full lines are true attitudes. Right plot: Estimation errors for attitude.

Figure 11.7: Left plot: Dashed lines are estimated angular velocities and full line is true angular velocities. Right plot: Estimation errors for angular velocities.
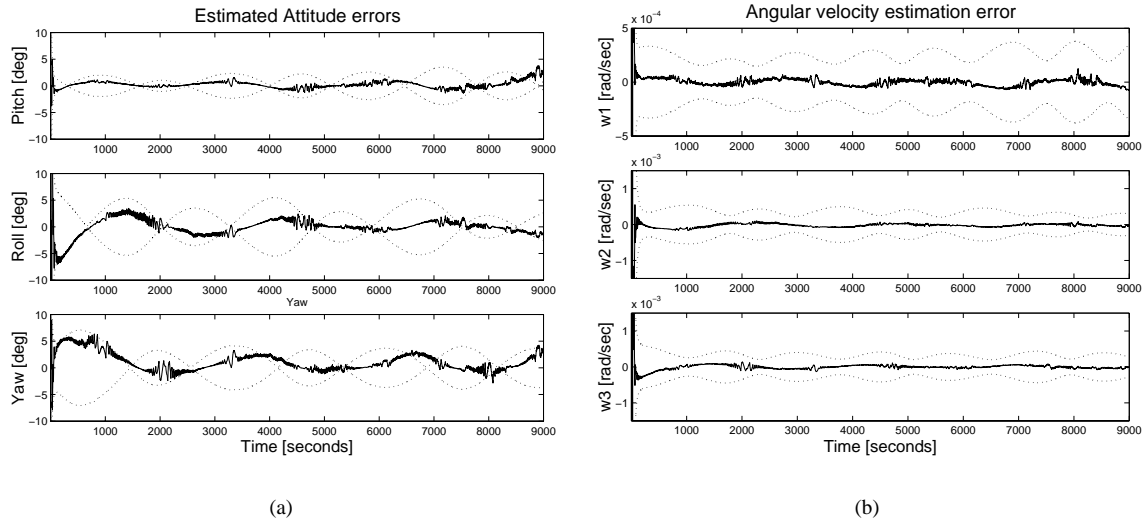
94

Figure 11.8:

11.4.5 Discussion of results

The extended Kalman filter was made to converge. Simulations did show that the use of sun sensors in combination with the magnetometer improved convergence. However the accuracy suffered from using sun sensors. It may still be possible to tune the filter, in order to get better performance also when using solar panels. A few simulations different from the one shown in this simulation were performed, where the filter showed a similar performance. However, further simulations should be performed to improve the filter design. The attitude determination was not tested in combination with attitude control. This will have to be done to see if the requirements to accuracy can be fulfilled.

11.5 Summary

An extended Kalman filter was developed for estimating angular velocities and attitudes. The filter was simulated in Matlab to test its performance. It showed that the best accuracy performance was obtained when only the magnetometer data was used. However, by using sun data together with magnetometer data it was possible to get the filter to converge faster. This resulted in a test where the filter only used magnetometer data and was started with an initial attitude obtained by the deterministic attitude determination. In this way convergence happened for the state within 1000 seconds with a maximum error of 15 $^\circ$. After convergence the errors of pitch, roll and yaw were within $\pm 2.5\,^\circ$.

chapter 12

Conclusion

The development and design of the ADS was initiated after the summer of 2001 as a part of the new AAU CubeSat project which was started up at the same time. As the entire project started from scratch was some development time required to lay a foundation for the overall design of the satellite and its mission. The mission was planned to consist of taking photos of Denmark from a Low Earth Orbit, which hereby defined the framework and the main requirements for the ADS.

It was defined that a three dimensional attitude determination and control would be required to perform the task of pointing the camera towards any cite to be photographed. Based on this and the fact, that the CubeSat satellite only has limited space and weight capabilities for subsystems, a attitude determination system was developed.

12.1 The Sensors

The first step in the design of the ADS was the choice of sensors. After a evaluation of possible sensors suitable for a satellite of the size of a CubeSat it was chosen to use a magnetometer and sun sensors.

The magnetometer was designed from magneto-resistive components from Honeywell. These components were chosen as they were classified as space approved and therefor suitable for the job. Also the implementation using a *SET/RESET* switching mode made it possible to measure the magnetic field of the Earth independent of temperature changes acting on the components.

A simple design was chosen for the sun sensors, consisting of a photovoltaic cell to be placed on each side of the cubic satellite. Hereby it is possible to determine the direction to the sun by using the output signals of the six sensors to generate a vector describing the direction of the sun relative to the spacecraft coordinate frame. As the sun sensors are *of the shelf* components, they have been tested regarding their performance at different light intensities and temperatures.

As the sun sensors are temperature dependent, six temperature sensors were applied; one to each sun sensor. The temperature sensors were chosen based on their size and temperature range and the fact, that they were space approved.

The circuitry to connect the sun sensors, temperature sensors and magnetometer with the micro-controller of the ADCS subsystem was developed in cooperation with (Frederiksen et al., 2002).

Sockets for assembling the sun sensors with the temperature sensors were designed and manufactured by (Overgaard and Hedegaard, 2002). However, they were not assembled yet due to the limited development time for the ADS. The ADS print for the engineering model of the satellite was designed and manufactured. The components on the print were mounted, including the magnetometer components. However, these prints have not been tested yet regarding their functionality and performance.

12.2   Software Architecture

The micro-controller of the ADCS is used only by the attitude determination to perform the data sampling and filtering of the data from the sun sensors. Including the *SET/RESET* switching of the magnetometer. The processing of this data and the attitude determination was chosen to be placed on the OBC. In this way the data sampled would be send from the ADCS to the OBC over the I^{2}C bus to be used in the attitude determination. The output of the ADS on the OBC will be send back to the ADCS subsystem containing the rotary motion of the satellite and the rotation between a reference attitude and the satellites current attitude. The reference attitude may either be the direction to the Sun or the direction in which to take a photo.

The sampling of data from the sensors was tested with a prototype print of the ADCS and parts of the software to be placed on the OBC was also developed. Communication between OBC and ADCS micro-controller over the I^{2}C bus was tested in a simple test.

12.3   ADS Algorithms

For the ADS algorithms were developed for determining the attitude of the satellite. For the processing of the sensor data algorithms were set up to determine sun vectors and directions of Earth's magnetic field with respect to the satellite body frame SCB. For creating reference vectors a orbit model, magnetic field model and sun model, including an albedo correction, were developed and tested. These algorithms will be used for determining the satellite position, the direction of the Earth's magnetic field as well as the direction to the Sun in the ECI coordinate frame. The albedo correction is used for lowering the errors due to Earth albedo on sun sensors. These reference vectors are used as references for the attitude determination, together with the measurements from the sensors. The algorithms were implemented and tested in both matlab and C using data from the Ørsted satellite.

For the attitude determination two algorithms were developed. The first consists of a deterministic method developed by (Markley, 2002). The method solves Wahba's problem by using the optimal quaternion estimation method based on two vector measurements. This algorithm was tested and implemented in C.

The second algorithm consists of a extended Kalman filter used for estimate the attitude and rotary motion of the satellite. Also this algorithm was tested and optimized by simulations in Matlab.

12.4   Simulations

Magnetic field errors and sun sensor errors were simulated to match the expected errors in Low Earth Orbit. The largest errors introduced to the system, were due to Earth albedo on the sun sensor readings. A model of the satellite dynamics were used to generate attitudes and angular rates. Models of the satellite orbit, magnetic field and Sun were used as truth models, to generate inputs to sensors. Attitude determination was tested for both the deterministic method and for the extended Kalman filter.

The deterministic algorithm gave a determined attitude with a accuracies below $8°$ during the tests. However, the determination of the velocity did not work as expected and will require some further development.

The accuracy of the extended Kalman filter was best when using only magnetometer data where attitutude error was approximately $\pm2°$. Convergence was fastest when also using sun sensor data. The best result was obtained when the deterministic attitude determination was used for initializing the filter. This resulted in fast convergence where the error never became larger than $15°$. After convergence the attitude error was approximately $\pm2.5°$.

The accuracies of the algorithms tested in the simulations lied below the main requirement of $8°$ accuracy. However, the tests performed did not include the ACS. The ACS will have to be included in order to determine if the pointing accuracy of $8°$ is obtained.

12.5 Future Work

Even as many goals have been reached is the design and development of the ADS still far from complete. The following points describe parts still left to be finished.

Hardware

- The sun sensors have to be assembled with the temperature sensors on the sockets.

- The ADCS print must be assembled in the engineering model with the other sub systems.

- The ADS print and sensors need testing regarding temperature changes, radiation and vacuum.

- The magnetometer of the ADS has to be calibrated while being mounted inside the satellite.

Software

- The deterministic attitude determination has to be optimized and a better velocity determination has to be developed.

- The extended Kalman filter has to be tested in simulations to optimize its performance.

- Satellite simulations need to be run over larger time intervals. Also by combining the ADS with the ACS algorithms to determine the overall pointing accuracy.

- The software has to be implemented and tested on the ADCS micro-controller and OBC.

- The communication with other subsystems has to be established and the performance of the complete ADCS needs to be tested.

appendix A

Environment in LEO

In this chapter the orbit and environment into which the AAU CubeSat is launched, is being considered. Though the launch vehicle has not been determined from the start of the design phase of the AAU CubeSat, it is expected that the satellite is launched into a LEO (Low Earth Orbit) with an altitude of 700 km. In chapter 7 orbital elements and coordinate systems used throughout this report are described. In the following section the factors of the space environment in this orbit are described.

A.1 Environment

Different factors may affect the functionality and lifetime of the satellite in space environment and during launch. To secure a successful mission of the satellite, following factors need to be considered:

Upper atmosphere - The upper atmosphere affects the satellite by generating aerodynamic drag, lift, heat and through the corrosive effects of highly reactive elements such as atomic oxygen.

Trapped radiation - Radiation trapped in the Van Allen radiation Belts degrades materials and electronic components.

Solar protons from flares - Degrades materials and electronic components, causes single-event effects in semiconductor components.

Cosmic rays - Causes single-event effects in semiconductor components.

Solar radiation: IR, Visible, UV, X-ray - Degrades materials and electronic components.

Plasma from magnetic sub storms - Charges surfaces of the satellite to high negative voltages

Out-gassing - Deposits on cold surfaces, e.g. optical apertures.

Also during launch the satellite will be exposed to extreme environmental factors, such as acceleration, vibration, shock, acoustics and possibly contamination of sensors and solar panels from launchers out-gassing materials. However, of these factors vibration and shock is the only factors considered.

Vibrations - During launch the satellite will be exposed to vibrations.

Shocks - A shock may be generated when a primary payload is deployed using pyrotechnic.

A typical thermal environment inside a launch vehicle is in (Larson and Wertz, 1992) 10-35 °C, which is within the temperature limits considered in LEO. The mechanical interface to the P-POD which deploys the CubeSat is defined in (Connolly, 2000). A kill-switch (Connolly, 2000) on the satellite will ensure that the satellite is not powered up until deployment from the P-POD. For this reason the CubeSat design does not have to include functionality during launch or electrical interfaces to the launch vehicle.

Different approaches are taken to accommodate the effects from environmental factors in LEO and during launch. In the following it is considered how to accommodate the effects from the environmental factors described above.

A.1.1 Degradation of materials and electronic components

Materials and electronic components are degraded by radiation from solar radiation and when passing through the Van Allen radiation Belts. To minimize this degradation of materials and electronic components, the appropriate amount of shielding must be used for the satellite.

Components used in each subsystem of the satellite in the satellite must be selected with care. A design guide is to choose radiation hardened components and components which have already proved to be working in LEO environment will also be a guideline for design. Finally electronic components must be radiation tested.

- Shielding - Mech

- Space approved components - CDHS, PSU, COM and ADCS

- Radiation test on hardware - CDHS, PSU, COM and ADCS

A.1.2 Single-event phenomena

Single-event phenomena occur in common electronic components as microprocessors, RAM circuits and hexfet power transistors and can be caused by solar protons from flares or by cosmic rays. These phenomena include three different effects: Single-event upsets, single-event latch-up and single-event burnout.

Single-event upsets - causes bit flips in RAM circuits. Single-event upsets neither damages the component nor interferes with its subsequent operation. Failures from single-event upsets in CDHS, COM, PSU and ADCS are compensated for within the subsystem itself. Protection methods to be considered for electronics in each subsystem: Watchdog timer, redundancy, lockstep, voting and repetition. - CDHS, COM, PSU and ADCS.

Single-event latch-up - causes the component to draw excessive current and does not operate proper until power is turned off and then back on. This type of failure is to be detected in the PSU subsystem. The PSU then for a short time switches the power off in the failing subsystem and turns it on again.

Single-event burnout - causes the component to burnout permanently. The failing component may cause the entire subsystem to fail. This should be considered when designing electronics for each subsystem. - CDHS, PSU, COM and ADCS

A.1.3 Electronically charged surfaces

Surfaces of the satellite may be electronically charged by plasma from magnetic sub-storms. – Ground structure and antennas. - COM, MECH

A.1.4 The upper atmosphere

Atmospheric drag - Depends on the ballistic coefficient, atmospheric density and velocity of the satellite relative to the atmosphere. With an altitude above ≈600 km drag is so weak that orbits usually last more than ten years.

Temperature - Temperatures are considered for components mounted on the outer surface of the satellite and electronics inside the satellite. The AAU CubeSat is being designed to orbit the earth in approximately the same altitude as the Ørsted satellite, which is orbiting in a 700 km altitude. For this reason the temperature specifications used for the Ørsted satellite (see table A.1), are also used for the CubeSat. Components have to be tested to see that they can operate in the specified temperature ranges. - Mech, CDHS, COM, PSU and ADCS

Atomic oxygen - Reacts with thin organic films, advanced composites and metallized surfaces, resulting in lost or degraded sensor performance. Chemical reactions involving atomic oxygen may produce radiantly active excited constituents which, in turn, emit significant amounts of background radiation create effects such as "shuttle glow", and interfere with optical sensors. The effects of atomic oxygen can be accommodated when choosing materials. Mech

Component	Non-Operating/Transportation	Nominal operating	Qualification
Solar panels	-70°C to +125°C	-60°C to +80°C	-70°C to +90°C
Battery pack	-20°C to +30°C	0°C to +25°C	-5°C to +35°C
Electronics	-40°C to +60°C	-20°C to +40°C	-30°C to +50°C

Table A.1: Temperature specifications for the CubeSat are the same as used for the Ørsted satellite [Ørsted]

A.1.5   Out-gassing

Out-gassing deposits on cold surfaces, e.g. optical apertures such as camera lenses or sensors. Out-gassing is avoided or minimized by selecting materials. Particles deposited on optical apertures can during operation be removed with heat from heating elements or the sun. - Mech, ADCS

A.1.6   Vibrations

During launch the satellite is exposed to vibrations. This should be considered in the design of the satellite and vibration tests should be conducted on a test model of the satellite.

A.1.7   Shocks

For deploying satellites or separating spacecraft components from the launch vehicle, pyrotechnic devices are typically used. These devices are light and reliable. However, they generate shocks that transmits to other components mounted on the launch vehicle. This should be considered in the design of the satellite and vibration tests should be conducted on a test model of the satellite.

appendix B

Estimated signal from sun sensors

In this appendix the maximum short circuit current I_{sc} to expect from the photodiodes is estimated using the spectral distribution E_e for extraterrestrial solar irradiance and a relative spectral sensitivity curve for the photodiodes. The short circuit current $I_{sc,\lambda}$ at a wavelength λ can be found as the product of the spectral sensitivity S_e of the photodiode and the spectral solar irradiance E_e. Integrating over all wavelengths, in equation B.1, will result in the total short circuit current from the photodiode:

$$I_{sc} = \int S_e(\lambda) \cdot E_e(\lambda) \, d\lambda \tag{B.1}$$

B.1 Extraterrestrial solar radiation

The solar energy flux data is plotted in figure B.1 together with blackbody radiation spectral distributions at 5800° K and 2854° K. The data used to plot the solar irradiance is "The 1985 Wehrli Standard Extraterrestrial Solar Irradiance Spectrum" and has an accumulated solar radiation of 1367 W/m^2. If data from a year with a higher total irradiance had been used, it would fit the 5800° K temperature curve better. The 2854° K blackbody radiation, which the photodiodes are tested with from Silonex, has a peak near 1000 nm as shown in the figure. The spectral distribution of extraterrestrial solar radiation has peak value near 500 nm. The spectral radiation M_λ can be derived using equation B.2, where λ is the wavelength and T the temperature in Kelvin.

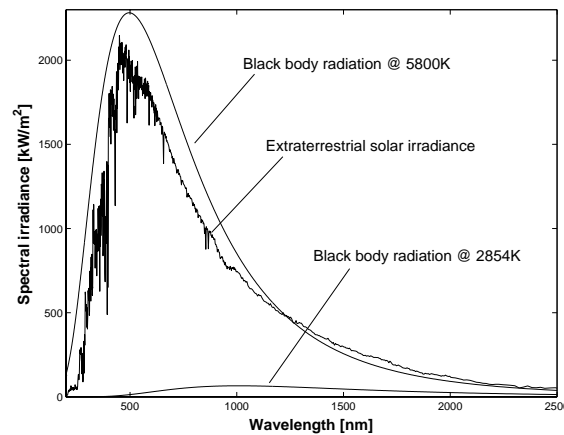$$M_\lambda = \frac{3.745 \times 10^8}{\lambda^5} \left(\frac{1}{e^{14388/\lambda T} - 1} \right) \tag{B.2}$$

Figure B.1: The black body radiation curves have been scaled with a 10e-5 factor to fit the extraterrestrial solar irradiance data.

The relative spectral sensitivity curve used for the photodiodes can be seen in figure B.2. No spectral sensitivity for the sensors has been provided from the manufacturer, so the spectral sensitivity for a BPW-34B photodiode is used. BPW-34B also has an approximate 0.55 mA peak near 930 nm and a spectral sensitivity range from 350 nm to 1100 nm. Using the function **polyfit** in Matlab a polynomial of order 12 has been fitted to data points on the BPW-34B spectral sensitivity curve to produce figure B.2.
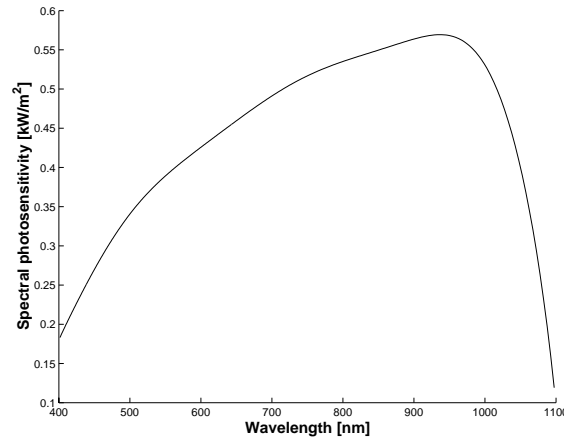

Figure B.2: The spectral photo sensitivity used for determining maximum short circuit current

The maximum short circuit current is found using the data for extraterrestrial solar irradiation in figure B.1 and photo sensitivity in figure B.2 together with the summation in equation B.3.

$$I_{sc} = \sum_{n=i} S_e(\lambda_i) \cdot E_e(\lambda_i) \cdot (\lambda_i - \lambda_{i-1}) \tag{B.3}$$

Using equation B.1 results in a short circuit current approximately 1.05 mA from a photodiode when exposed to 1763 W/m² extraterrestrial sun light.

$$I_{sc} = 1.05\,mA \quad @ \quad 1367\,W/m^2 \text{ Extraterrestrial sun light}$$

Files for estimating the maximum signal from the sun sensors can be found on: *CDROM:/sunsensors/photosensitivity/*. Data used for plotting photo sensitivity, extraterrestrial solar irradiance and terrestrial solar irradiance can be found in the files *diode.txt*, *wehrli85.txt* and *e892g.txt*, respectively. The matlab file *plotdata.m* loads data from txt-files, plots data and makes the summation in equation B.3.

B.2 Conclusion

The maximum short circuit current from the photodiodes at extraterrestrial sunlight is estimated to $I_{sc} = 1.05\,mA$. Due to uncertainty with respect to the spectral photo sensitivity curve of the photodiodes, I_{sc} should be expected larger when designing the interface to the photodiodes.

appendix C

Quaternions

A quaternion is composed of a vector and a scalar part.

$$\bar{q} = \begin{bmatrix} q \\ q_4 \end{bmatrix} = \begin{bmatrix} \sin(\theta/2)\hat{n} \\ \cos(\theta/2) \end{bmatrix} \tag{C.1}$$

In equation C.1 the unit vector $\hat{n}$ corresponds to the axis of rotation, where θ is the angle of rotation. The unit quaternion possesses only three degrees of freedom and satisfies the constraint $\bar{q}^T\bar{q} = 1$.

A *cross-product equivalent matrix* is the skew symmetric matrix defined in equation C.2.

$$[q\times] = \begin{bmatrix} 0 & -q_3 & q_2 \\ q_3 & 0 & -q_1 \\ -q_2 & q_1 & 0 \end{bmatrix} \tag{C.2}$$

It only includes the first three values of the quaternion, as these include the vector part of the quaternion.

The *quaternion product operation* $\otimes$ is similar to matrix product operations, in which two rotations are combined to gather one single rotation. The quaternion product operation can be more easily expressed, as defined in equations C.3 and C.4.

$$\bar{q} \otimes \bar{q}_b = [\bar{q}]\bar{q}_b \tag{C.3}$$

$$[\bar{q}] = \begin{bmatrix} q_4 & q_3 & -q_2 & q_1 \\ -q_3 & q_4 & q_1 & q_2 \\ q_2 & -q_1 & q_4 & q_3 \\ -q_1 & -q_2 & -q_3 & q_4 \end{bmatrix} \tag{C.4}$$

Or alternatively using equations C.5 and C.6.

$$\bar{q} \otimes \bar{q}_b = [\Xi(\bar{q})|\bar{q}]\bar{q}_b \tag{C.5}$$

$$\Xi(\bar{q}) = \begin{bmatrix} q_4 & -q_3 & q_2 \\ q_3 & q_4 & -q_1 \\ -q_2 & q_1 & q_4 \\ -q_1 & -q_2 & -q_3 \end{bmatrix} \tag{C.6}$$

The *Inverse rotation (conjugate)* $*$ of a quaternion is given by equation C.7.

$$\bar{q}^* = \begin{bmatrix} -sin(\frac{\Theta}{2})\hat{n} \\ cos(\frac{\Theta}{2}) \end{bmatrix} \tag{C.7}$$

C.1   Properties of quaternion composition

C.1.1   Commutative relation

Similar as in the case of rotation matrixes, the commutative relation of quaternions is given in equation C.8.

$$(\bar{a} \otimes \bar{b}) \otimes \bar{c} = \bar{a} \otimes (\bar{b} \otimes \bar{c}) \tag{C.8}$$

C.1.2   Product rule for quaternion composition

The derivative of a quaternion product is given as in equation C.9.

$$\frac{d}{dt}(\bar{a} \otimes \bar{b}) = \left(\frac{d}{dt}\bar{a}\right) \otimes \bar{b} + \bar{a} \otimes \left(\frac{d}{dt}\bar{b}\right) \tag{C.9}$$

C.2   Time evolution of quaternion

The time evolution of a quaternion can be described as in equation C.10 and C.11.

$$q(t + \Delta t) = q(\Delta t) \otimes q(t) \tag{C.10}$$

$$q(\Delta t) = q(t + \Delta t) - q(t) \tag{C.11}$$

For small rotations $q(\Delta t)$ the equation of the quaternion can be assumed to consist of a small rotational angle θ, which results in equation C.12.

$$q(\Delta t) = \begin{bmatrix} \frac{1}{2}\bar{\theta} \\ 1 \end{bmatrix} \tag{C.12}$$

Here $\bar{\theta}$ represents the rotation vector containing the angles around the x, y and z axes. The fourth part of the quaternion is equal to 1 due to the cosine value of a very small angle θ. By combining equation C.10 with C.11 it will result in equation C.13, which will result in equation C.14 when differentiated with respect to a small Δt.

$$q(\Delta t) = (q(\Delta t) \otimes q(t)) - q(t) \tag{C.13}$$

$$\frac{d}{dt}\bar{q}(t) = \frac{(q(\Delta t) \otimes q(t)) - q(t)}{\Delta t} \tag{C.14}$$

Accordingly the derivative of the quaternion $\bar{q}$ will result in equation C.15.

$$\dot{\bar{q}} = \begin{bmatrix} \frac{1}{2}\dot{\bar{\theta}} \\ 1 \end{bmatrix} \otimes \bar{q} = \begin{bmatrix} \frac{1}{2}\bar{\omega} \\ 1 \end{bmatrix} \otimes \bar{q} = \frac{1}{2}\Omega(\omega)\bar{q} \tag{C.15}$$

Where $\Omega(\omega)$ is given in equation C.16.

$$\Omega(\omega) = \begin{bmatrix} 0 & \omega_3 & -\omega_2 & \omega_1 \\ -\omega_3 & 0 & \omega_1 & \omega_2 \\ \omega_2 & -\omega_1 & 0 & \omega_3 \\ -\omega_1 & -\omega_2 & -\omega_3 & 0 \end{bmatrix} \tag{C.16}$$

appendix D

State Transition Matrix

In the following sections the setup of the state transition matrix and other parameters are described. These are relevant for the design of the Extended Kalman Filter, which is used in the recursive attitude estimation of the ADS.

D.1   Matrix F_1

Deriving F_1 takes its starting point with the error quaternion:

$$\bar{q} = \delta\bar{q} \otimes \hat{\bar{q}} \tag{D.1}$$

Applying equation C.9 and C.15 to equation D.1, yields:

$$\dot{\bar{q}} = \delta\dot{\bar{q}} \otimes \hat{\bar{q}} + \delta\bar{q} \otimes \dot{\hat{\bar{q}}} \tag{D.2}$$

$$\frac{1}{2}\Omega(\omega)\bar{q} = \delta\dot{\bar{q}} \otimes \hat{\bar{q}} + \frac{1}{2}\delta\bar{q} \otimes \Omega(\hat{\omega})\hat{\bar{q}} \tag{D.3}$$

Using that $(\bar{q} \otimes \bar{q}^{-1} = [0,0,0,1]^T)$ rearranging equation D.3 gives equation D.4

$$\delta\dot{\bar{q}} = \frac{1}{2}\Omega(\omega)\bar{q} \otimes \hat{\bar{q}}^{-1} - \frac{1}{2}\delta\bar{q} \otimes \Omega(\hat{\omega})[0,0,0,1]^T \tag{D.4}$$

Now using that $(\delta\bar{q} = \bar{q} \otimes \hat{\bar{q}}^{-1})$ and then letting $(\bar{\omega} = [\omega, 0]^T)$:

$$\delta\dot{\bar{q}} = \frac{1}{2}\Omega(\omega)\delta\bar{q} - \frac{1}{2}\delta\bar{q} \otimes \Omega(\hat{\omega})[0,0,0,1]^T \tag{D.5}$$

$$\delta\dot{\bar{q}} = \frac{1}{2}\Omega(\omega)\delta\bar{q} - \frac{1}{2}\delta\bar{q} \otimes \hat{\bar{\omega}} \tag{D.6}$$

The matrix $\Omega(\omega)$ is linear in its elements.

$$\Omega(\omega) = \Omega(\hat{\omega} + \Delta\omega) = \Omega(\hat{\omega}) + \Omega(\Delta\omega) \tag{D.7}$$

Using the commutative relation in equation C.8 results in:

$$\delta\dot{\bar{q}} = \begin{bmatrix} -[\hat{\omega}\times]\delta q \\ 0 \end{bmatrix} + \frac{1}{2}\Omega(\Delta\omega)\delta\bar{q} \tag{D.8}$$

$$\delta\dot{\bar{q}} = \begin{bmatrix} -[\hat{\omega}\times]\delta q \\ 0 \end{bmatrix} + \frac{1}{2}\begin{bmatrix} \Delta\omega \\ 0 \end{bmatrix}\delta q_4 + \text{HOT} \tag{D.9}$$

106

The Higher Order Terms (HOT) are negligible and $\delta p_4 \approx 1$.

$$\delta \dot{\bar{q}} = \begin{bmatrix} -[\hat{\omega} \times] \delta q \\ 0 \end{bmatrix} + \frac{1}{2} \begin{bmatrix} \Delta \omega \\ 0 \end{bmatrix} = \begin{bmatrix} -[\hat{\omega} \times] \\ 0 \end{bmatrix} \delta q + \frac{1}{2} \begin{bmatrix} \Delta \omega \\ 0 \end{bmatrix} \tag{D.10}$$

From which it is obvious that the matrix F_1 is:

$$F_1 = \begin{bmatrix} -[\hat{\omega} \times] | \frac{1}{2} I_{3 \times 3} | 0_{3 \times 3} \end{bmatrix} \tag{D.11}$$

appendix E

Collinearity of Magnetic Field and Sun Direction

The deterministic attitude determination algorithms require at least 2 vectors to determine an attitude. However, when these two vectors are collinear does this create a problem similar to having only a single vector available for the attitude determination. This is not sufficient to determine the attitude of the satellite uniquely. When the measurement vectors of the magnetic field and the suns position are parallel or collinear will it therefore not be possible to determine an attitude.

E.1 Possibility of Collinearity

As the vector describing the direction of the sun in the ECEF coordinate frame rotates around the Z axis every day, are all possible Right Ascensions of the sun possible during a day. However, the suns declination does only vary from +23.4°to -23.4°during one year.

This means, that only the angle between the earths equatorial plane and the magnetic field vector compared with the angle between the equatorial plane and the sun direction vector is of importance. When these two angles have similar values, will a case of collinearity occur during the same day.

The magnetic field over Denmark can be determined by using an 13.th order IGRF model, which also has been used for simulations and tests of the on-board magnetic field model. The coordinates of Denmark range approximately from a l attitude of 55°to 57.5°and a longitude from 8°to 13.5°. When these spherical coordinate ranges are changed to a satellite position vector in the ECEF frame, they can be used as input for the IGRF model to obtain a range of unit-vectors in the same coordinate describing the directions of earths magnetic field over Denmark.

The angle between the magnetic field vector and the earths equatorial plane is determined, by finding the angle between a magnetic field vector and a magnetic field vector with a Z-value set to zero, as shown in E.1.

$$\alpha_{mag/equat} = \frac{R_{mag} * R_{mag0}}{|R_{mag}||R_{mag0}|} \qquad R_{mag} = \begin{bmatrix} x_{mag} \\ y_{mag} \\ z_{mag} \end{bmatrix} \qquad R_{mag0} = \begin{bmatrix} x_{mag} \\ y_{mag} \\ 0 \end{bmatrix}$$

The angle between the magnetic field over Denmark and the equatorial plane varies from angles of 30.5 °to 37°. The angle between the sun and the equatorial plane, the declination, will always lie below 23.4 degrees.

Because of this will there never occur collinearity between the magnetic field vector and the direction of the sun while the satellite is over Denmark. The closest the two vectors are getting to each other will be an angle of 7 degrees when the earth is in perihelion.

However, this collinearity effect and the determination of it occurrence also depends on the measured vectors and if the sun-vector is measured and used for attitude determination or the sun vector including the earth albedo? In that case will the computations of possible collinearities be much more complex, due to the earth albedo, which can't be determined exactly based on mathematical approximations.

However, to calculate the precise orbital positions and times, when collinearity between the magnetic field and a sun-albedo vector will appear over Denmark, is going to be left to the ground station team of the AAU CubeSat, when the satellite has been launched and is taking images over Denmark.

appendix F

Verification of on-board models using Ørsted data

The IGRF magnetic field models of orders 2 to 13 were tested with data from the Danish satellite Ørsted. This has been used for the choice of which order to use for the IGRF model, on-board the AAU CubeSat. Also the on-board orbit model and the SGP4 orbit model used in simulations, were verified using Ørsted data.

In section F.1 the details on Ørsted data used for testing orbit and magnetic field models are documented. Then in section F.2 the errors are plotted for each of the magnetic field model orders.

F.1   Østed Data used for testing IGRF and orbit models.

Position and magnetic field data from the Danish satellite Ørsted is used for validating the orbit and IGRF models. The data has been provided by DMI (DMI, 2002). The IGRF2000 coefficients have been determined using magnetic field data from the Ørsted satellite (IAGA, 2002), so the data can be expected to be reliable. In the Ørsted satellite the position is determined using a GPS-receiver. Two Line Elements (TLE) for Ørsted has also been provided by (DMI, 2002). The TLE's originate from NORAD (CelesTrak, 2002) like the TLE's to be used for the CubeSat. The Ørsted data used in simulations has the following format:

Format: "Oersted Prelim Mag-L: High precision magnetic field data" in ascii file.

Files For simulating magnetic field - date 10. jan 2000 to 17. jan 2000

ml000110.txt, ml000111.txt, ml000112.txt, ml000113.txt, ml000114.txt, ml000115.txt, ml000116.txt, ml000117.txt - (Version 0.91, Level 2.3)

Files for simulating magnetic field - date 9. feb 2002 to 10. feb 2002

ml020209.txt, ml020210.txt - (Version 1.0, Level 2.3)

F.2   Errors between IGRF models and Ørsted data

Errors for Ørsted data and IGRF models are plotted for Ørsted orbits during 9. and 10. of February year 2002. To speed up simulations, only every tenth sample is plotted. This means that x-axes are in unit [10 seconds]. A little less that two days are plotted in the figures F.1 and F.2.

F.3   Magnetic field model error due to position uncertainty

The magnetic field model uses the satellite position in the ECEF frame, as an input. This means that an error in position results in an error of the determined magnetic field vector. This error caused has been determined from simulation. From verification of the on-board orbit model, described in section 7.2.3, the position error over one week was determined using data from Ørsted. Ørsted position data and corresponding on-board orbit data, generated in the orbit model verification, is used as input to two similar IGRF models of order 6. Before using position data as input to the IGRF model, the data was transferred from the ECI
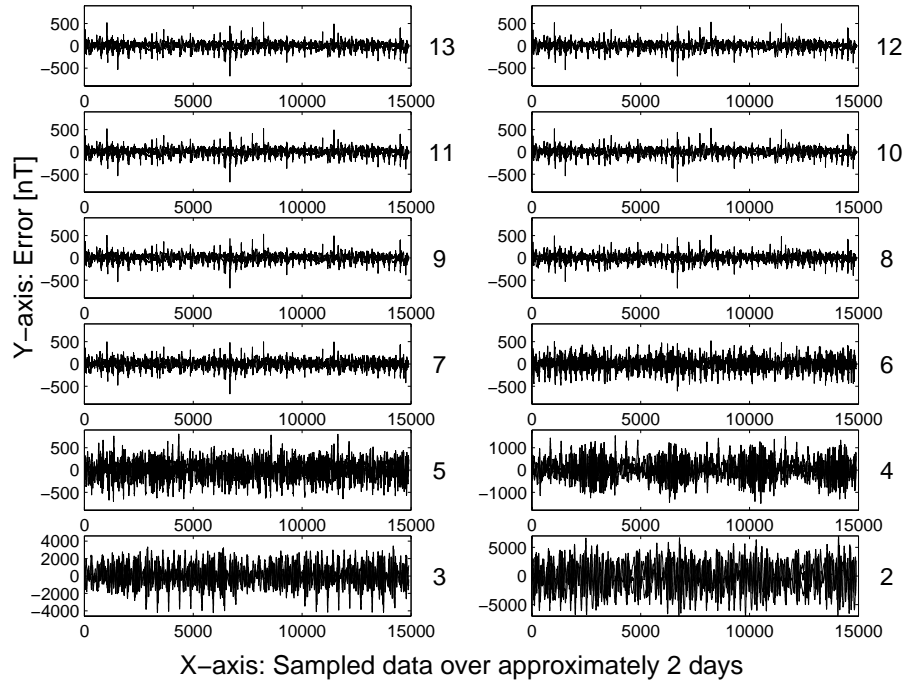
Figure F.1: To the right of each plotted error, the orders 2 to 13 of the tested IGRF model is noted
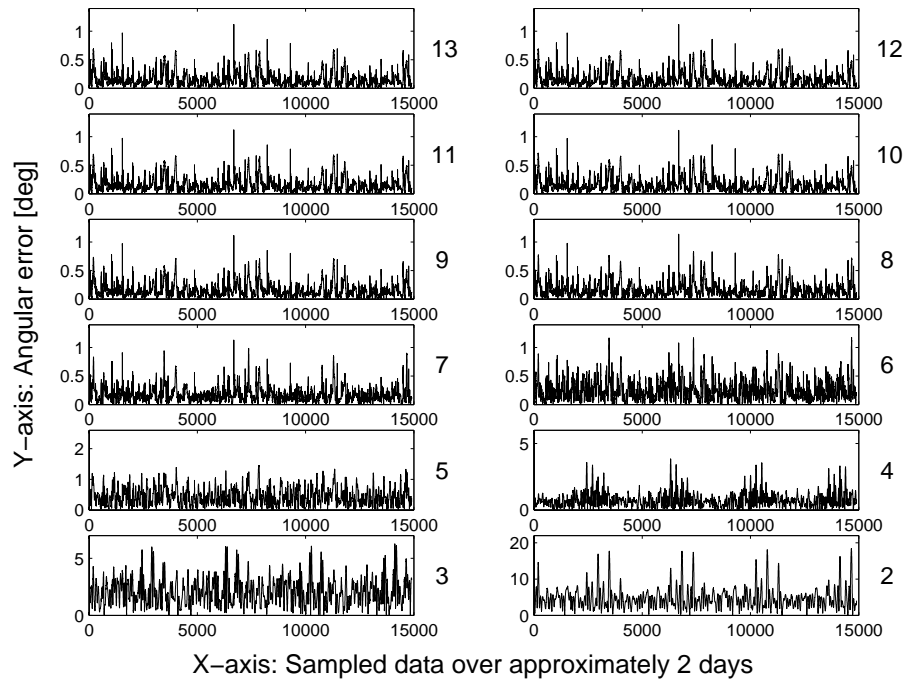

Figure F.2: To the right of each plotted error, the orders 2 to 13 of the tested IGRF model is noted

111

to the ECEF frame. The error of the on-board orbit model with respect to the Ørsted position data, has resulted in an error for the magnetic field vector, as shown in figure F.3 and F.4. Over the first 2.5 to 3 days (258000 seconds) the RMS error of the magnetic field on the three axes is 168 nT and the RMS angular error is 0.21°. The error stays constant the first three days with a maximum error of 0.4 °and over one week
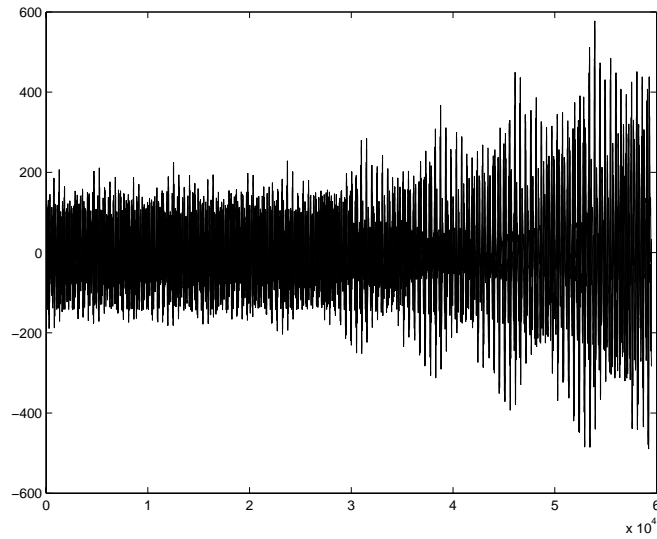
Figure F.3: On-board magnetic field model error in nT due to position uncertainty.

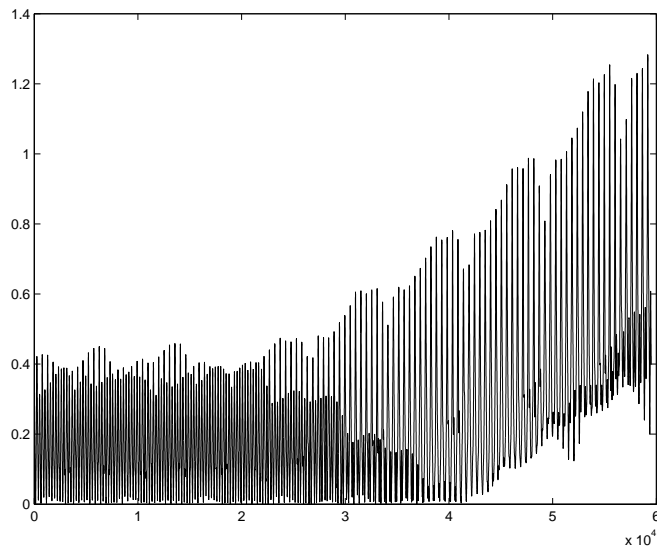it rises to maximum error of approximately 1.3 °.

Figure F.4: Angular error of on-board magnetic field model due to position uncertainty.

appendix G

Interface to PIC Micro-controller

The interface between the PIC micro-controller of the ADCS and the OBC consists of an I^2C bus. The protocol to be used for the communication on this bus between the OBC and the micro-controller was developed in a cooperation with (Frederiksen et al., 2002).

The I^2C bus is used to transfer housekeeping, system data and the data needed by the power save and camera controller, between the OBC and ADCS subsystem. The data is given in table G.1, where the module column is related to the I^2C protocol described later. The module named housekeeping will contain data form the different sensors on the ADCS-subsystem and an error vector.

Update mode changes the mode in the PIC software. The algONOFF vector can be either updated or read.

The number given in the position column is related to the position in the I^2C data array defined in the micro processor software (PIC-SW) and the name is related to the content of the variable. Some bytes are split up in two 4 bit variables to minimize memory consumption.

Module	Pos.	Name		Module	Pos.	Name	
3	0	MODE			23	Current Z	Mag Z
	1	ERROR 1			24	Temp 1	Sun 1
	2	ERROR 2			25	Temp 2	Sun 2
	3	MAGX		0	26	Temp 3	Sun 3
	4	MAGY			27	Temp 4	Sun 4
	5	MAGZ			28	Temp 5	Sun 5
	6	SUN 1			29	Temp 6	Sun 6
	7	SUN 2			30	Q1_LSB	
	8	SUN 3			31	Q1_MSB	
	9	SUN 4			32	Q2_LSB	
	10	SUN 5			33	Q2_MSB	
	11	SUN 6			34	Q3_LSB	
0	12	Current X			35	Q3_MSB	
	13	Current Y			36	Q4_LSB	
	14	Current Z			37	Q4_MSB	
	15	Temp 1		2	38	WX_LSB	
	16	Temp 2			39	WX_MSB	
	17	Temp 3			40	WY_LSB	
	18	Temp 4			41	WY_MSB	
	19	Temp 5			42	WZ_LSB	
	20	Temp 6			43	WZ_LSB	
	21	Current X	Mag X	1/4	44	algON/OFF	
	22	Current Y	Mag Y				

Table G.1: Data communicated via the I^2C bus.

Module number	Module type
0	Housekeeping
1	Update algONOFF
2	Update reference
3	Update mode
4	Read algONOFF

Table G.2: I2C module number

G.0.1 I^{2}C protocol

The I^{2}C protocol defined for the CubeSat has the structure as shown in figure G.1 and G.2, defining respectively a master write cycle and a master read cycle. The Address is the 8-bit address of the subsystem, with the least significant bit as the R/$\bar{W}$ bit, the address for the micro-controller of ADCS is 0x80.

The Chksum is calculated as the sum of all data transmitted including the module number. The Chksum is the given as the least significant byte of the sum, and the Read... and Write... represent reading and writing the data related to the chosen module.

Start	Address	Module	Chksum	Stop	Start	Address+1	Read......
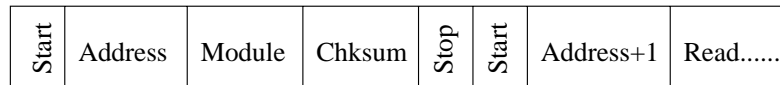
Figure G.1: Master write cycle.

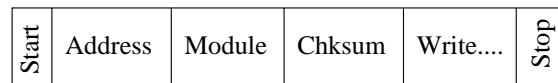| Start	Address	Module	Chksum	Write....	Stop

Figure G.2: Master read cycle.

G.0.2 Error vector

The error vector is 16 bit were each bit indicate a individual hardware or software error see table G.3. A logical "1" indicate a error. Bit 14 and 15 are reserved for further updates.

G.0.3 AlgONOFF vector

The algONOFF is a 8 bit vector G.4 with bit 5-7 that are reserved of updates.

The magnetometer performance can be changed between *SET/RESET* mode, which is set up as default, and sampling of data, using the mean values of the magnetometer components. In case of that the *SET/RESET* algorithm does not work, the data handling on the OBC will send the command to the micro-controller to change over to data sampling of the magnetometer. In this vector "ON" and "Mean" (bit 3) is a logical "1".

bit number	Error type
0	Coil X error
1	Coil Y error
2	Coil Z error
3	Magnetometer X error
4	Magnetometer Y error
5	Magnetometer Z error
6	Multiplexor 1 error
7	Multiplexor 2 error
8	Magnetometer Set/Reset error
9	Sun sensor error
10	ADC error
11	Reference 1.22 V error
12	Reference 2.5 V error
13	I^2C error
14	Not used
15	Not used

Table G.3: Error vector

bit number	Error type
0	Coil X (ON/OFF)
1	Coil Y (ON/OFF)
2	Coil Z (ON/OFF)
3	Magnetometer algorithm (Mean/Difference)
4	Magnetometer Set/Reset (ON/OFF)
5	Not used
6	Not used
7	Not used

Table G.4: AlgONOFF vector

appendix H

Circuit Prints

In the following text a short introduction to the print board for the ADCS will be given. The prints containing the elements of the ADCS subsystem were designed in cooperation with (Frederiksen et al., 2002).

H.1   The Design of the Circuit Print

The print of the ADCS is designed to have two of the batteries of the power supply for the CubeSat mounted on one of the sides. The design space left on the print for this purpose can be seen in figure H.1. On the right figure a rectangular space is left on the surface of the design space. This is used by the backsides of the sun sensor sockets, as this sides lignes up with the side panel of the satellite.

(a) Design space top side (b) Design space bottom side
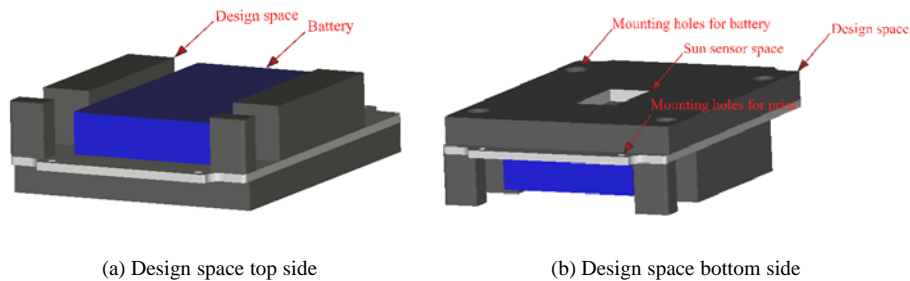
Figure H.1: The Design space on the ADCS Print

The design of the print and the locations of the different componnents can be seen in figure H.2. The components on the print referring to the numbers given can be seen in table H.1. These prints represent the engineering model of the ADCS but have not been tested yet regarding functionality and performance.
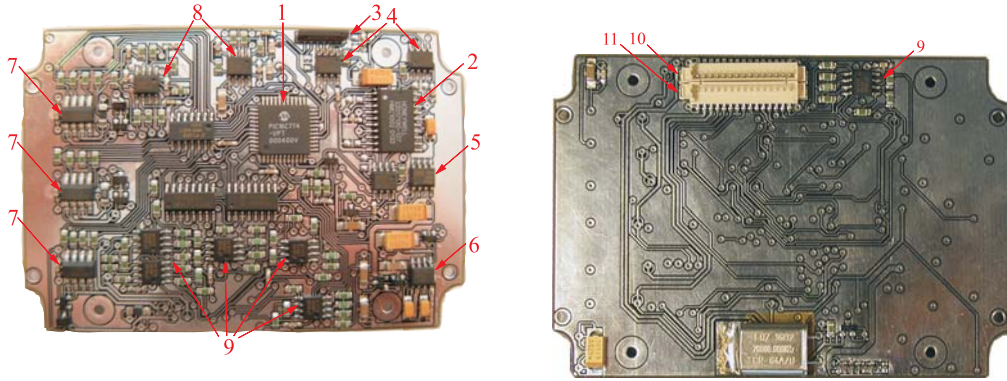
(a) The print seen form top   (b) The print seen form bottom

Figure H.2: The ADCS print board seen from top and bottom

Number	Name
1	PIC micro processor (PIC16C774)
2	Magnetometer 1
3	Magnetometer 2
4	Magnetometer amplifier
5	Hex fet
6	DC-DC converter
7	H-bro coildriver
8	Current amplifier
9	Sun/temperature sensor interface
10	Connector 1
11	Connector 2

Table H.1: Board describtion

appendix I

Temperature coefficient of sun sensors

It is necessary to know the temperature coefficient of the photodiodes, in order to compensate for temperatures in the sun sensor readings. This test report describes how the temperature coefficient of the photodiodes used in the sun sensors is determined. The photodiodes are tested with light from a xenon lamp, to simulate extraterrestrial light.

I.1 Test setup

Following equipment was used for the test:

- Orc Illuminator 6000 xenon lamp
- Climate cabinet from Vötsch
- Prototype print for ADCS
- Two photodiodes mounted on aluminum block
- Power supply (B&O SN16A)
- Thermometer (NiCr-Ni DIN K-IEC)
- PC with RS-232 interface for data logging

The Xenon lamp uses an optical fibre which fits into an outlet in one side of the climate cabinet. The photodiodes are mounted on an aluminum block and placed inside the climate cabinet where they are exposed to light from the xenon lamp. The prototype print is used for sampling the sun sensors and is placed outside the climate cabinet with wires to the sun sensors through an outlet in the top of the climate cabinet. A thermometer measures the temperature at the outlet with the sensing part placed inside the climate cabinet. The PC is connected to the prototype print via a RS-232 connection. The program "Tera Term version 2.3" is used on the PC for data logging. The test setup can is shown in figure I.1.
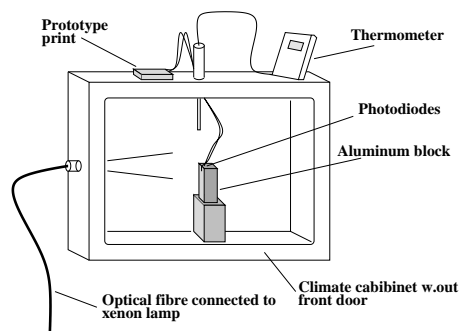

Figure I.1: Test setup for finding temperature coefficients of photodiodes

118

I.2 Test procedure

During the test the photodiodes are exposed to a constant light from the xenon lamp. In the beginning of the test the xenon lamp is turned on for approximately five minutes, before light radiance from it is constant.

1. Climate cabinet is cooled down to -38.5 °C.

2. The xenon lamp is switched on and the test begins after five minutes when the lamp is giving a constant light.

3. Data logging with constant light on the photodiodes and a constant temperature at -38.5 °C is carried out for approximately twenty minutes.

4. The temperature in the climate cabinet is set to 86°C, while the output from the photodiodes is logged.

5. After the temperature in the climate cabinet has reached 86 °C, data logging is continued for approximately twenty minutes.

I.3 Test results

The logged data from the photodiodes is plotted in Matlab, and can be seen in figure I.2. Mean values used for the temperatures -38.5°C and 86 °C are indicated in the plots. Sampled data and the Matlab file used for plotting data and determining temperature coefficients can be found on: *CDROM:/hwValidation/sunsensors/tempcoef/*.
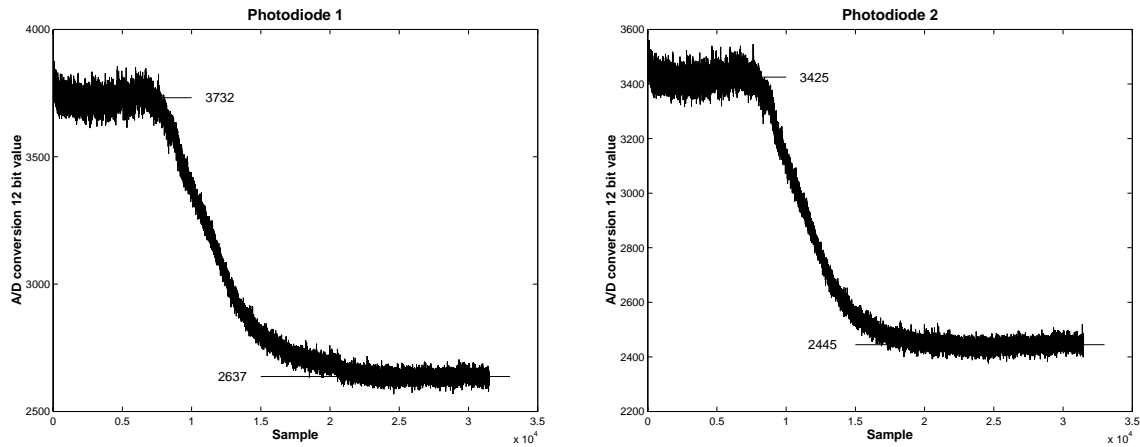

Figure I.2: The maximum output signal from the two photodiodes is not the same. This can be due to differing photo sensitivities of the photodiodes, and because of minor inaccuracies when mounting on the aluminum block.

Using the data plotted in figure I.2 and the temperature change from -38.5 °C to 86°C the temperature coefficients are found for both photodiodes in equation I.1 and equation I.2:

$$TC_i = \frac{3732 - 2637}{3732} \cdot 100\% \cdot \frac{1}{124.5°\text{C}} = 0.2356\%/°C \tag{I.1}$$

$$TC_i = \frac{3425 - 2445}{3425} \cdot 100\% \cdot \frac{1}{124.5°\text{C}} = 0.2299\%/°C \tag{I.2}$$

When the temperature rises, the output from the photodiodes falls. The temperature coefficient of the photodiodes is determined to 0.233%/°C.

From this test it can also be seen that variance of the signal becomes larger with increasing signal. Using the **var** command in Matlab on data from sample 1700 to 4500 the variances for photodiode 1 and 2 are found to be 1029 and 896, respectively. The noise is white and for the first photodiode it is approximately ± 100 bit peak-peak around its mean value 3721. The resulting angular error can be found to: $\mathrm{atan}(100/3721) \approx 1.5°$

I.4 Evaluation of results

The most significant sources of errors are the temperature measurements, the temperature control in the climate cabinet and variations in the light from the xenon lamp.

Temperature measurement errors: On the thermometer the specified accuracy is ± 1.8 °C.

Temperature control: The temperature control in the climate cabinet can not keep the temperature constant as it variates with ± 1°C. This is especially the case when trying to keep the temperature at -38.5°C and can be seen in figure I.2 in samples 1 to 6500. A constant temperature was obtained at 86°C.

Variations in light: If the light from the xenon lamp decreases or increases slowly over time this will introduce an error in the results. This error, however, seems to be negligible since the sampled data from the photodiodes from sample 25000 and upwards is constant.

The temperature measurement error and inaccuracies due to temperature variations may cause a total temperature error of 2.8°C. This error is no more than 2.28% of the temperature interval -38.5 °C to 86°C.

The test does not take errors into account, which are due to the fact that the irradiance spectrum of the xenon lamp does not completely correspond to extraterrestrial sun light. Nor does it take into account that the temperature coefficients of other photodiodes may differ from the tested. However, these errors are considered to be small.

I.5 Conclusion

The temperature coefficient for the photodiodes is determined to be 0.233%/ °C.

appendix J

Maximum short circuit current from photodiodes

The purpose of this test report is to determine the short circuit current from the photodiodes when exposed to extraterrestrial sun light. In the test the photodiodes were exposed to three different light sources, with close resemblance to extraterrestrial sun light.

J.1 Test setup

For these tests the following equipment was used:

- Mavolux luxmeter
- Orc Illuminator 6000 xenon lamp
- Osram DULUX L Lamp 18W/12-950
- Prototype print for ADCS
- Two photodiodes mounted on aluminum block
- Power supply (B&O SN16A)
- PC with RS-232 interface for logging data

A xenon lamp and an Osram DUKUX L lamp were chosen as light sources, because they have a close resemblence to daylight. The prototype print for the ADCS is used for sampling data from the photodiodes. The interface is dimensioned to convert a maximum short circuit current from the photodiodes of 2 mA to 5V.

The PC is connected to the prototype print via a RS-232 connection. On the PC the program "Tera Term version 2.3" is used for data logging. The photodiodes are glued onto an aluminum block to make them easier to handle. The luxmeter is set to measure W/m^2.

J.2 Test procedure

The output from the photodiodes is tested by exposing them to terrestrial sunlight, light from a xenon lamp and light from an Osram DULUX L lamp. Through these tests the idea is to expose the luxmeter and the photodiodes to the same amount of light. The irradiance measured with the luxmeter is noted, while the data from the sun sensors is sampled.

J.2.1 Terrestrial sunlight

This test was performed on a day with only few clouds in the sky and took place at Aalborg University. The sensing part of the luxmeter and the photodiodes were directed towards the Sun, while the data from the sun sensors was sampled.

J.2.2 Xenon lamp

Before the start of this test the xenon lamp had been switched on for five minutes in order to give a constant radiance. The photodiodes were placed 20 centimeters from the the xenon light source and sensor data was sampled and logged on the PC. Afterwards the photodiodes were removed, and the luxmeter was placed in the exact same place to measure the amount of light from the xenon lamp.

J.2.3 Osram DULUX L lamp

The photodiodes and the luxmeter were both exposed to light from the Osram lamp. The effect of the Osram lamp was only 18W and it was necessary to place the photodiodes close to the lamp. This made it difficult to test the photodiodes accurately. To improve the quality of tests with the Osram lamp, sun sensor data was sampled at three different distances to the lamp.

J.3 Test results

The sampled data from the tests and a Matlab file for determining the maximum short circuit currents can be found on *CDROM:/hwValidation/sunsensors/maxIsc/*. The irradiance measured with the luxmeter has been noted in the beginning of each file. In table J.1 the first column shows the sun sensors and the light sources. Second and third column show the values measured with sun sensors and magnetometer, respectively. Column 4 contains estimated outputs from the twelve bit A/D-converter at a light input of $1428\ \mathrm{W/m^2}$ and column 5 shows the short circuit current from the photodiodes.

Sun sensors	A/D-value	Lux-meter reading	A/D-value @ 1428 $\mathrm{W/m^2}$	I_{sc} @ 1428 $\mathrm{W/m^2}$
Daylight				
SS1	1845	895 $\mathrm{W/m^2}$	2944	1.437 mA
SS2	1861	895 $\mathrm{W/m^2}$	2969	1.450 mA
Xenon lamp				
SS1	650	870 $\mathrm{W/m^2}$	1067	0.521 mA
SS2	693	870 $\mathrm{W/m^2}$	1137	0.555 mA
Osram lamp (2.2 cm)				
SS1	252	292 $\mathrm{W/m^2}$	1232	0.602 mA
SS2	231	292 $\mathrm{W/m^2}$	1130	0.552 mA
SS3	210	292 $\mathrm{W/m^2}$	1027	0.502 mA
Osram lamp (5.1 cm)				
SS1	119	143 $\mathrm{W/m^2}$	1188	0.580 mA
SS2	115	143 $\mathrm{W/m^2}$	1148	0.561 mA
SS3	90	143 $\mathrm{W/m^2}$	899	0.439 mA
Osram lamp (8.6 cm)				
SS1	61	78 $\mathrm{W/m^2}$	1117	0.545 mA
SS2	62	78 $\mathrm{W/m^2}$	1135	0.554 mA
SS3	29	78 $\mathrm{W/m^2}$	531	0.259 mA

Table J.1: Test results of light measurement

J.4 Evaluation of results

The most significant sources of errors in these tests, are:

- The light spectrum of the light sources used in these tests differs from the light spectrum of extraterrestrial sun light.

- Difficulties in exposing both luxmeter and photodiodes to the same amount of light.

During all tests some error must be expected due to differing angles of incoming light to the photodiodes and to the luxmeter. When testing with the xenon lamp and the Osram lamp, the distance from the light source to the photodiode or the luxmeter may differ, and this will also give errors to the results.

The spectres of the light sources used in the tests differ from the spectrum of extraterrestrial light. Xenon lamps together with filters are normally used as simulators for extraterrestrial sun light (Frank L. Pedrotti, 1993). In these tests no filters were used together with the xenon lamp.

The Osram lamp is specified to correspond to daylight. Because irradiance from it was low compared to extraterrestrial irradiance, it was decided to make tests at different distances from the lamp. At short distances it was difficult to expose luxmeter and photodiodes to the same amount of light. On the other hand it was only possible to use a limited range of the A/D-converter at long distances, which result in lower accuracy.

J.5 Conclusion

The test results from the xenon lamp and the Osram lamp both indicate a maximum short circuit current near 0.5 mA. Tests using daylight as light source indicate a maximum short circuit current near 1.45 mA.

appendix K

Test of cosine characteristic for primary sun sensors

The purpose of this test report is to determine how well the characteristic of the sun sensors resemble a cosine characteristic. The test is performed with the prototype print according to test specification TH2.1.

K.1   Test setup

The tested photodiode is mounted on a rotation device with inbuilt protractor. A xenon lamp is mounted in a fixed position to the photodiodes, in such a way that the photodiode can be rotated within the full field of view, with respect to incoming light. Data is sampled from the photodiode using the prototype print and is logged with a PC.

K.2   Test procedure

With the xenon light switched on, the photodiodes are rotated through their full field of view ($180\,^\circ$) in steps of 5°. At each step a data sequence is sampled from the sun sensor.

K.3   Test results

Mean values of sun sensor readings are found for each $5\,^\circ$, and the plotted using Matlab. Sampled A/D-converter values are normalized with respect to their maximum output. Temperatures was measured to vary within 20.5° and 20.9°.
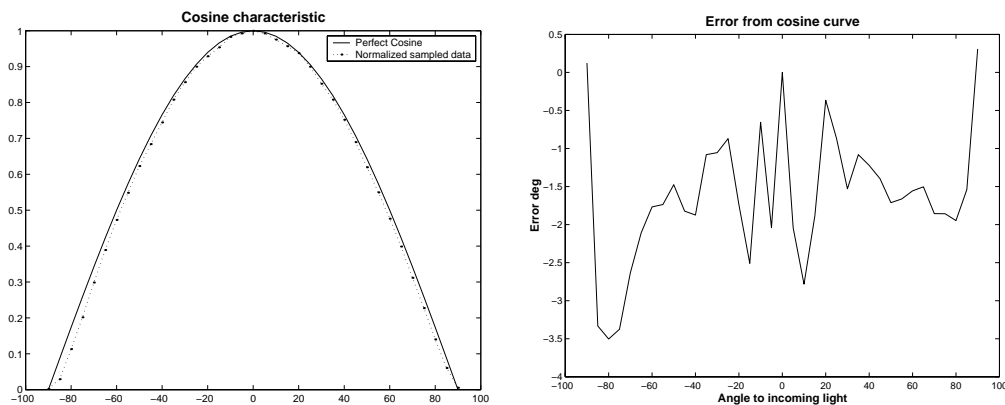
Figure K.1: Cosine characteristic for test of one photodiode and error with respect to perfect cosine curve.

K.4   Evaluation of results

In the process of performing this test, it became clear that it is important to be thorough when mounting the photodiodes, to avoid misalignment errors in engineering and flight model. It was also evident that the photodiodes do not have perfect cosine characteristics, but have a small error with respect to a perfect cosine curve. Maximum error in the cosine characteristic for the test results documented here, is $3.5\,°$and the RMS error is found to be $1.84°$. The maximum error occurs at one outer limit of the sun sensors field of view.

K.5   Conclusion

The error in the cosine characteristic of the tested photodiode is within requirement H2.1 of $4\,°\sigma$. Maximum error is $3.5°$ and RMS error is $1.84°$.

appendix L

Validation of prototype magnetometer

In this appendix the validation test for the magnetometer is described. The test is performed on the prototype print to validate the functionality of the chosen design and components, according to test specification TH2.2. From the test results the bridge offset in the sensors can be determined. A calibration procedure to compensate for hard or soft iron distortion of the magnetic field is be performed using the test data.

L.1 Test equipment

The prototype print with the integrated magnetometer is mounted on a non-magnetic device to rotate it. A simple device has been created for this purpose using LEGO. The test equipment consisted of:

- Prototype print

- Power supply (B&O SN16A)

- PC with RS-232 interface

- Simple device for rotating prototype print.

L.2 Test setup

The test is performed in a laboratory, where other magnetic fields than the Earth's magnetic field may be present. What is important through this test is that the magnetic field, in which the magnetometer is rotated, is constant.

The PC is connected through the RS-232 connection to the prototype print which is mounted on the rotation device. For the first test the magnetometer is mounted with the X and Y axes in the horizontal plane. For the second test is mounted with the X and Z axes are in the horizontal plane. A drawing of the magnetometer rotated in the two planes is shown in figure L.1

Figure L.1: To the left the magnetometer is rotated in the X-Y plane In the right figure the magnetometer is rotated in the X-Z plane

L.3   Test procedure

The procedure below is done with rotations both in the magnetometer X-Y plane and the X-Z plane.

1. Power is turned on for the prototype print.

2. For a small minute magnetometer data is sampled while not rotating the magnetometer.

3. The prototype print, which is mounted on the rotation device, is slowly rotated two turns by hand, while data is sampled.

L.4   Test results

During point 2 in the test procedure a constant magnetic field is measured. From these test results the noise level of the signal can be found. From the data logged during point 3 the rotation in the magnetic field is measured. In the following the units of the magnetometer outputs are in bits read from the 12 bit A/D-converters.
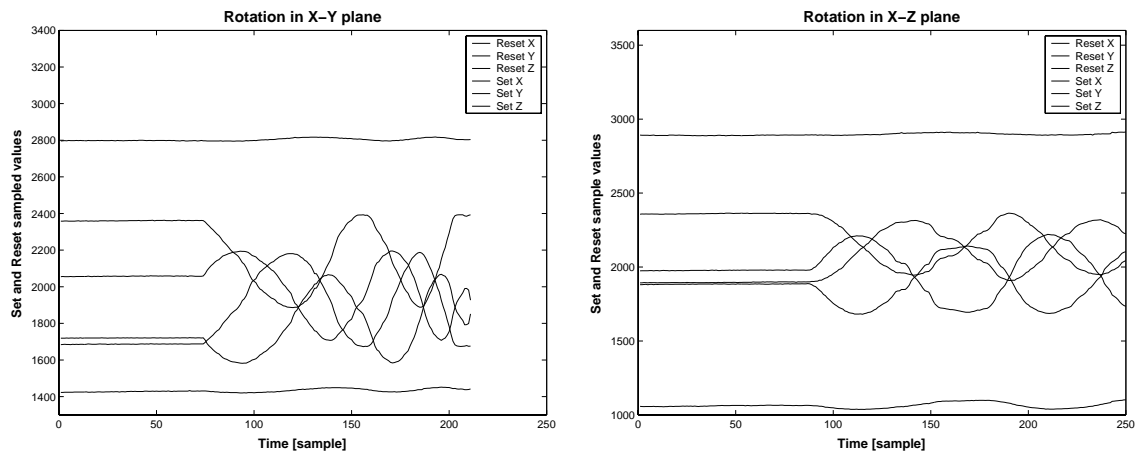
Figure L.2: Data sampled with set and reset switching plotted as function of time

From figure L.2 it can be seen that the noise of the signal is lower than the resolution of the 12 bit A/D-converters used for sampling the magnetometer data.

In figure L.3 data is plotted for the rotation plane X-Y and X-Z. Set/Reset switching technique has been used for creating the data. The sampled data has been used for calibration and resulting data has been plotted. The calibration parameters, used for introducing offsets and to scale data for each axis, are:

$$X_{off} = 62.5 \qquad Y_{off} = 100.0588 \qquad Z_{off} = -28.2571$$

$$X_{sf} = 1 \qquad Y_{sf} = 0.9529 \qquad Z_{sf} = 1.1774$$

The files with sampled magnetometer data and a matlab files for plotting data and perform calibration can be found on: *CDROM:/hwValidation/magnetometer/*.
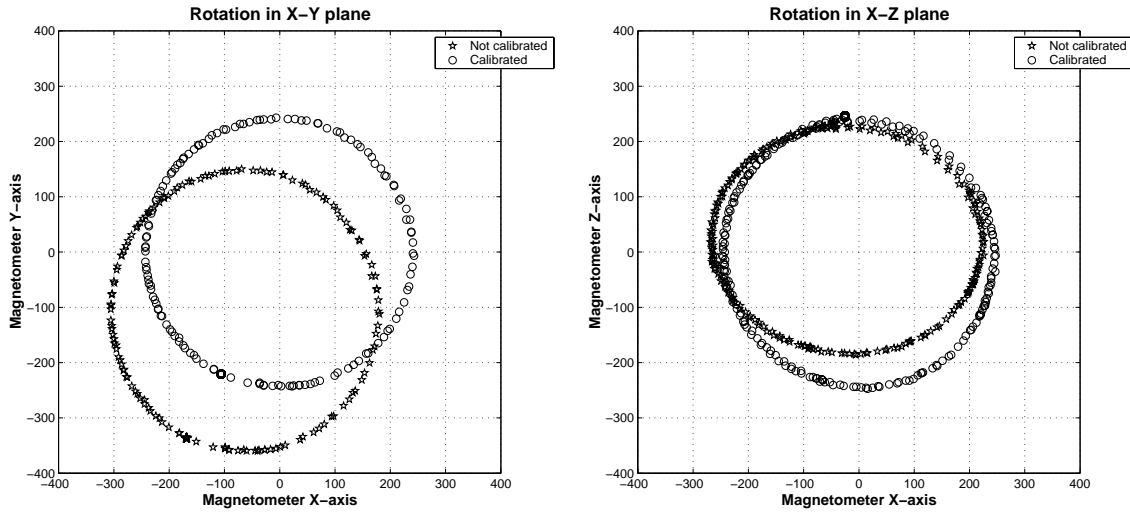
127

Figure L.3: Set Reset switching data plotted before and after calibration

L.5 Evaluation of results

The test results in figure L.3 show almost perfect circles for the calibrated data. The axis rotated about in the tests did not stay constant due to wobble in the rotation device. This can be seen from figure L.2, where the Set and Reset data not is constant for the axis rotated about. The test results show that the magnetometer is functional. However, a more robust rotation device will be used for testing engineering and flight model.

L.6 Conclusion

Tests show that the prototype magnetometer is working. Based on rotations in the X-Y pland and in the X-Z plane of the magnetometer, scaling factors and offsets can be found for each of the sensors. These were found for the prototype, and will have to be determined also for the engineering and the flight model. From the tests it can also be seen that noise from the sensors is lower than the resolution of the A/D-converters.

appendix M

Validation test of temperature sensors

The validation test of the temperature sensors was performed on the prototype print. It is validated that the output from the sensors fit the Steinhart-Hart thermistor equation equation 5.3 on page 37. This is done by comparing measurements of the temperature sensors with the measurements of a thermometer.

M.1 Test setup

Following equipment was used for the test:

- Climate cabinet from Vötsch

- Prototype print for ADCS

- Six thermistors from BetaTherm with extended wires

- Power supply (B&O SN16A)

- Thermometer (NiCr-Ni DIN K-IEC)

- PC with RS-232 interface for showing sampled data

- Ice water

The prototype print is placed on top of the climate cabinet. The thermistors are placed inside the climate cabinet and connected to the prototype print through an outlet in the top of the cabinet. The sensing part of the thermometer also measures the temperature inside the cabinet through the same outlet. The prototype print is connected to the PC with a RS-232 connection. The program Tera Term is used for reading data from the RS-232 port and displaying it on the monitor.

The ice water is used for exposing the thermistors and the thermometer to a known temperature of $0\,^{\circ}$C, to check for temperature offsets.

M.2 Test procedure

In this test the thermistors used for the temperature sensors are exposed to a temperature changing from -40°C to 85°C. At temperature intervals of approximately 5°C measured with the thermometer, data from the temperature sensors is sampled. This results in 25 sample values for each temperature sensor. Data sampled from the temperature sensors is printed out to the PC monitor in a terminal window. When a set of sampled values is to be logged, the six temperatures are manually copied from the Tera Term and into a text file. The temperature measured with the thermometer for a given sample is also written in the file. The test procedure is as follows:

1. The temperature in the climate cabinet is set to -40°C

2. Sampling of temperatures is started with the prototype print.

3. The temperature is increased from -40 to 85 °C, while sampling data at approximately 5 °C intervals.

4. The test stops when the temperature in the climate cabinet reaches 85 °C.

After having tested the thermistors in the climate cabinet, ice is used to cool down the thermistors and thermometer to a known temperature of 0°C. When a constant temperature has been reached the temperature sensors are sampled and the temperature from the thermometer is written down.

M.3   Test results

In figure M.2 the sampled values for the six temperature sensors are plotted. The X-axis shows the sampled A/D-converter values and the Y-axis displays the temperature measured with the thermometer.

Figure M.1(a) shows the data sampled for each temperature sensor, when exposed to ice water. Standard deviations of these results are within 3 bit and outliers are present. In the plots in figure M.2 the mean values for the measurements in ice water are marked with a circle. The thermometer measured 0 °C when it was in ice water.

Based on the amplifier circuitry in the temperature sensors and the Steinhart-Hart algorithm for the thermistors, a curve can be plotted to describe the relationship from temperature to A/D-converter value. The error between the curve and sampled data is plotted in figure M.1(b).

Files with data from the tests and the Matlab file used for processing and plotting the data and errors can be found on: *CDROM:/hwValidation/tempsensors/*.
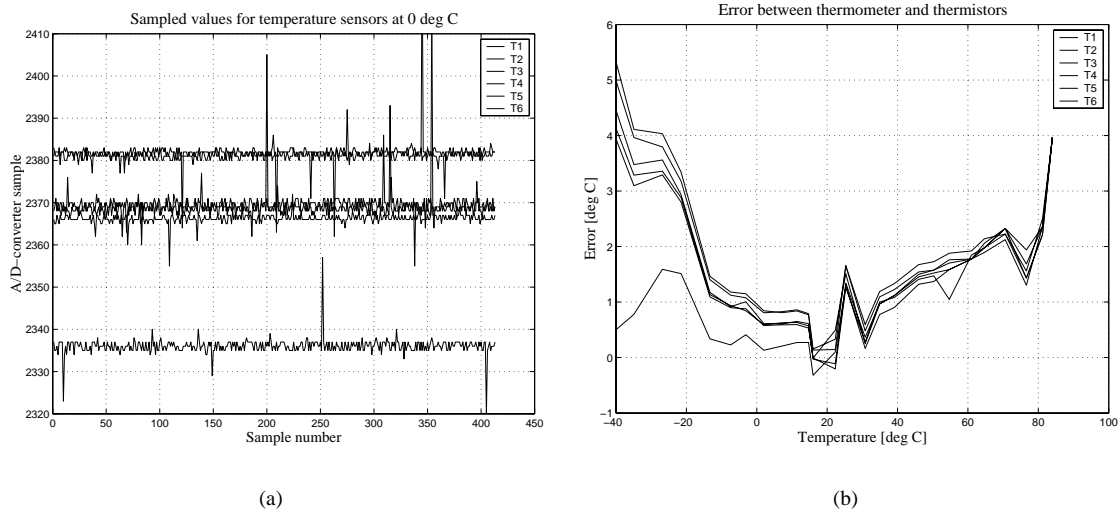

(a)

(b)

Figure M.1: (a) Temperature sensors at 0 °C. (b) Errors between temperature sensors and Steinhart-Hart curve
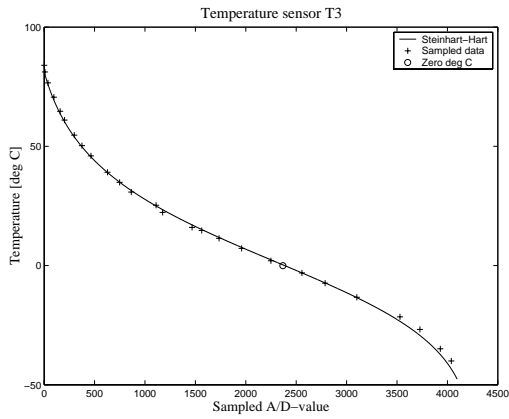
M.4   Evaluation of results

The most significant source of error in this test is the thermometer reading. The thermometer is specified to have an accuracy of ±1.8°C in the range -50°C to 199.9°C. The air inside the climate cabinet is ventilated by a fan, so the temperature around the thermometer and the temperature sensors is assumed to be the same.
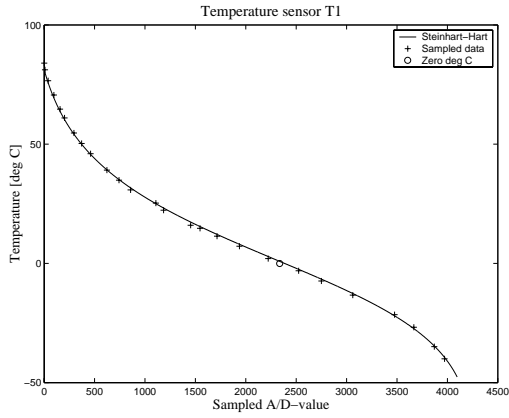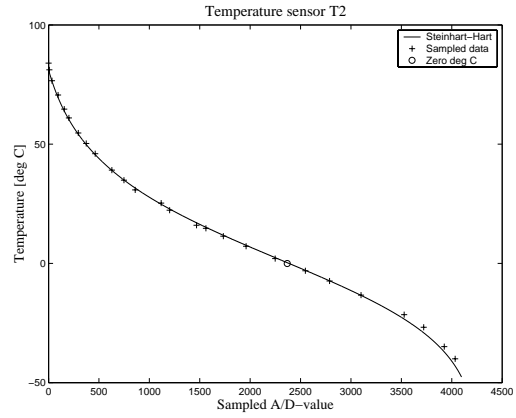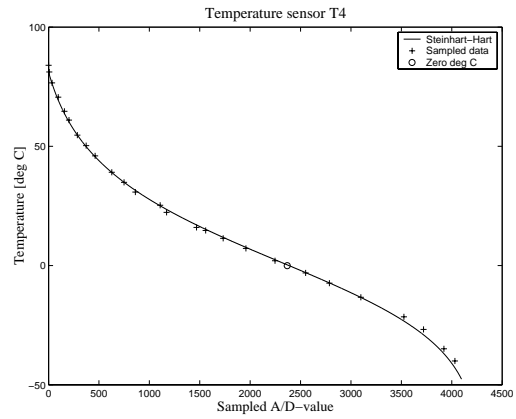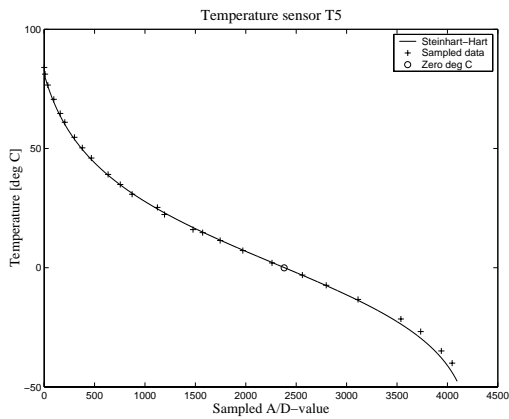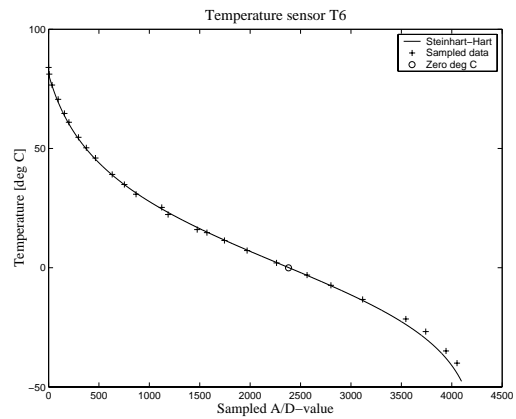
Figure M.2: Sampled data is plotted at different temperatures are marked with a '+'. Data is plotted with a curve representing the transfer function from A/D-converter readout to temperature

131

The test data plotted in figure M.2 follows the temperatures measured with the thermometer. According to the test, errors are largest at low temperatures (high A/D-values in figure M.2). The thermometer is tested with ice water to be accurate at $0°C$ and the temperature sensors all have errors below $1°C$. The accuracy in the range [-10 ... 80]$°C$ is within $2.2°C$. In the range [-40 ... 85]$°C$ the accuracy is within $5°C$. The errors may be $1.8°C$ larger or smaller when taking the thermometer error into account. Introducing an offset of -1$°C$ to temperatures measured with temperature sensors the total error is $\pm1.5°C$ within the range [-10 ... 80]$°C$ and $\pm3°C$ within [-30 ... 85]$°C$.

The small offsets in errors between temperature sensors are not due to thermistors, but due to the electronics used to interface the thermistors. This was tested by exchanging the thermistors in the temperature sensors and observing that the sampled values from each temperature sensor stayed the same. As expected this shows, that the thermistors are interchangeable.

appendix N

Magnetic field simulation using Spenvis

This chapter contains simulations of the magnetic field in an altitude of 700 km in a sun-synchronous orbit with local time of ascending node set to 1.30 hours. The simulation is obtained from the webpage SPENVIS (SPace ENVironment Information System) with the purpose of getting a quick idea of the magnetic field intensity.

N.1   Simulation results

The magnetic field is simulated using the IGRF model for epoch 2000. The orbit specified for the simulation is a sun-synchronous model with orbit epoch 1st January, 0 hours, 0 min, 0 secs and an orbit duration of 2 days. Plots generated from the simulation are shown in figure N.1 to figure N.3. It can be seen in figure N.1 that the magnetic field intensity is lower than 0.5 Gauss. In figure N.2 and N.3 be seen that the intensity is highest at the poles.
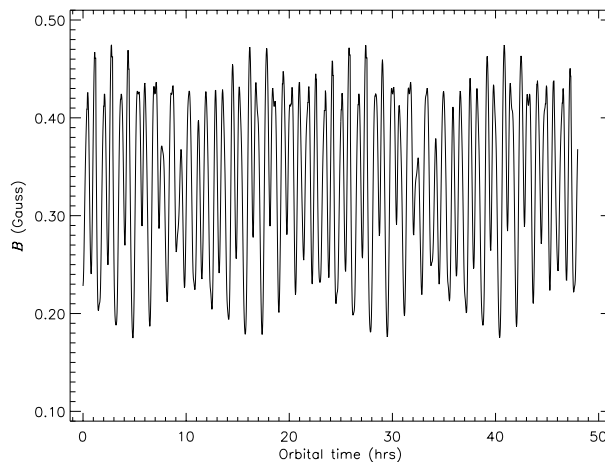

Figure N.1: Magnetic field intensity over time

N.2   Conclusion

It can be concluded from the simulations, that the magnetic field can be expected to be within 0.5 Gauss and that it is strongest near the poles.
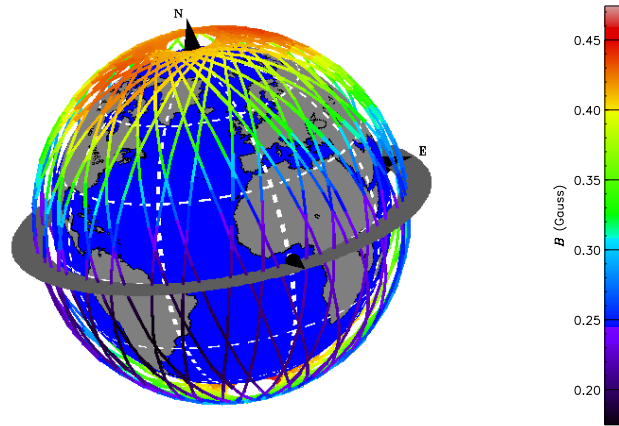
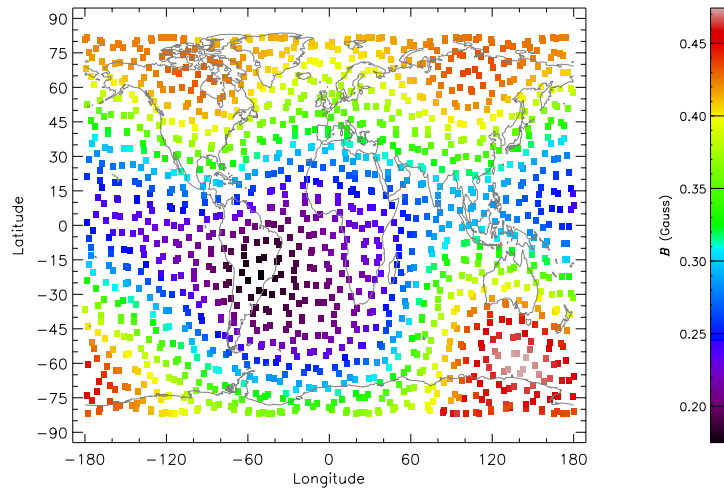Figure N.2: Orbit with magnetic field intensity

Figure N.3: Magnetic field intensity mapped on world

Bibliography

Amsat (2002). Webpage providing informations radio amateur satellites and two-line element sets. http://www.amsat.org/.

Bak, T. (1999). *Spacecraft Attitude Determination - a Magnetometer Approach*. PhD thesis, Aalborg University, Department of Control Engineering, Frederik Bajers Vej 7, Aalborg Ø, Denmark.

BetaTherm (2002). Betatherm homepage. http://www.betatherm.com.

Caruso, M. J. (1998). *Application note: Applications of Magnetoresistive Sensors in Navigation Systems*. Honeywell, 2-98 900212 edition.

Caruso, M. J. (1999). *Application of Magnetic sensors for low cost compass systems*. Honeywell SSEC.

CelesTrak (2002). Webpage providing two-line element sets. http://www.celestrak.com/.

Centrovision (2002). A primer on photodiode technology. Http://www.centrovision.com/tech2.htm.

Clausen, T. B., Hedegaard, A., Rasmussen, K. B., Olsen, R. L., Lundkvist, J., and Nielsen, P. E. (2002). Designing on board computer and payload for the aau cubesat.

Connolly, R. (2000). The p-pod payload planner's guide: Revision b. Technical report, SDMI at California Polytechnic State University. Can be found at http://www.calpoly.edu/ãero/polysat.

CubeSat Cute (2002). Webpage for japanese cubesat. http://horse.mes.titech.ac.jp/srtlssp/cubesat/index.html.

DMI (2002). Dmi homepage. http://www.dmi.dk/projects/oersted.

DSRI (2002). ørsted initial field model (oifm). http://www.dsri.dk/Oersted/Field_models.

ECSS (2002). Ecss-e-10-04, clause 6. Http://www.spenvis.oma.be/spenvis/ecss/ecss06/ecss06.html.

Felix R. Hoots, R. L. R. (1988). Models for propagation of norad element sets. *SPACETRACK REPORT NO. 3*, (3).

Frank L. Pedrotti, L. S. P. (1993). *Introduction to optics*. Prentice-Hall, Inc., second edition edition.

Frederiksen, M. K., Vedstesen, S. V., and Graversen, T. (2002). Attitude control in aau cubesat. Master's thesis, Aalborg University.

Grewal, M. S. and Andrews, A. P. (2001). *Kalman Filtering: Theory and practice using Matlab*. John Wiley & Sons, second edition.

Hall, C. (2002). Chapter 4 - attitude determination. http://www.aoe.vt.edu/ chall/courses/aoe4140/attde.pdf.

HMC1001-2 (1999). *Datasheet: 1- and 2-Axis Magnetic Sensors HMC1001/1002 HMC1021/1022*. Honeywell SSEC, 900248 rev. b 4-00 edition.

HMR2300r (1999). *Datasheet:THREE-AXIS STRAPDOWN MAGNETOMETER - HMR2300r*. Honeywell, 900232 rev. b 1/99 edition.

Humphreys, T. E. (2002). Attitude determination for small satellites using magnetometer and solar data.

IAGA (2002). Iaga homepage - international geomagnetic reference field - epoch 2000. http://www.ngdc.noaa.gov/IAGA/wg8/igrf.html.

Larson, W. J. and Wertz, J. R., editors (1992). *Space Mission Analysis and Design*. Microcosm, Inc. and Kluwer Academic Publishers, second edition.

Lazar, R. D., Bucelea, V., Loidl, A., Formanek, L., and Chlubna, T. (2002). Optimized design of power supply for cubesat at aalborg university.

Markley, F. L. (March-April 2002). Fast quaternion attitude estimation from two vector measurements. *Journal of Guidance, Control and Dynamics*.

Markley, F. L. and Mortari, D. (August 1999). Quaternion attitude estimation using vector observations.

Overgaard, L. and Hedegaard, M. (2002). Mechanical design of aau cubesat.

Roithmayr, C. (1992). Contributions of sperical harmonics to magnetic and gravitational fields.

RREDC (2002). Solar radiation resource information. Http://rredc.nrel.gov/solar/.

Ryer, A. (1998). *Light Measurement Handbook*. Technical Publications Dept. International Light, Inc., 17 Graf Road Newburyport, MA 01950-4092, second printing edition. Can be found at http://www.intl-light.com/.

Silicon (2002). Photodiode basics. Http://www.siliconsensors.com/PB.html.

Silonex (2001). *Datasheet: SLSD-71N8 Solderable Planar Photodiode*. Silonex Inc., rev 2 edition.

Wahba, G. (1965). Least squares estimate of satellite attitude. *SIAM Review*, 7(3).

Wertz, J. R. (1978). *Spacecraft attitude determination and control*. Kluwer Academic Publishers.